

Improvement in Metal-on-Metal Bearing of Hip Implants with
Advanced Stellite Alloys

by

Peishan Hu

A thesis submitted to the Faculty of Graduate and Postdoctoral
Affairs in partial fulfillment of the requirements for the degree of

Master of Applied Science

in

Materials Program

Carleton University
Ottawa, Ontario

© 2013, Peishan Hu

Abstract

CoCrMo alloy Stellite 21, which is a low-carbon Stellite alloy, has been used as hip implant material for a number of decades. However, its limited metal-on-metal bearing has resulted in loosening between the femoral head and acetabular cup of hip implants. As a result, there is a strong demand from the hip implant material industry for effective materials with improved metal-on-metal bearing. Three advanced Stellite alloys, high-carbon Stellite 720, Stellite 21 with addition of 10 wt%Cr (named modified Stellite 21) and Stellite 21 with addition of 0.4 ~ 0.6 wt%CrN (named nitrided Stellite 21), are proposed in this research. The wear and corrosion resistances of these alloys are investigated. The wear test is performed on a pin-on-disc tribometer at room temperature. The corrosion tests are conducted in the simulated human body environment (Hank's solution with pH 7.4 at the temperature of 37°C), which include the electrochemical tests of open circuit potential, cyclic polarization, potentiostatic and electrochemical impedance spectra (EIS), and immersion test. The experimental results demonstrate that the proposed alloys all exhibit better wear resistance than the conventional hip implant material, Stellite 21, either due to increased carbide volume fraction or because of the solid solution strengthening. The corrosion resistance of modified Stellite 21 is much better than that of Stellite 21. Although Stellite 720 and nitrided Stellite 21 are worse than Stellite 21 in corrosion resistance, they are still very corrosion resistant to Hank's solution. Therefore, all the three alloys are recommended for potential hip implant materials, but modified Stellite 21 with combined superior wear and corrosion resistance properties is highly recommended.

Acknowledgement

I would like to extend my deepest gratitude to my thesis supervisor Professor Rong Liu and Professor Jie Liu for their advice, guidance, support and patience during the difficult process of carrying out my research. I could not have completed this work without them.

I would like to sincerely thank Professor Glenn McRae and Dr. Dave McCracken for their continuous help and advice on the corrosion experiments.

I would like to sincerely thank Kevin Sangster, Steve Truttmann, Alex Proctor, David Raude and Gary Clements in departmental machine shop for their help and advice on material preparation.

I would like to thank Dr. Jianqun Wang and Dr. Nimal De Silva from the University of Ottawa for their help in SEM/EDX and ICP-OES examination.

I would also like to thank my colleagues, Xiaozhou Zhang, Kuan Jiang, and Sydney Nsoesie, and all of my friends for helping me out through all the tough times.

Finally, I would like to express my deepest appreciation to my mother, father, and siblings for their constant encouragement and moral support.

Table of Contents

Abstract.....	2
Acknowledgement	3
Table of Contents	4
List of Tables.....	8
List of Figures	9
List of Nomenclatures.....	15
List of Acronyms	17
1 Chapter: Introduction	19
1.1 Background and challenges	19
1.2 Present research.....	21
1.2.1 Objectives.....	21
1.2.2 Tasks and methodologies	22
1.3 Organization of the thesis	24
2 Chapter: Literature Review	26
2.1 Hip implants.....	26
2.1.1 Function and structure.....	26
2.1.2 Concerns for MOM hip implants	29
2.1.2.1 MOM bearing structure.....	29
2.1.2.2 Wear and corrosion behavior.....	30
2.2 Metallic materials for hip implants	33
2.2.1 Stainless steel.....	33
2.2.2 Titanium and its alloys	34
2.2.3 Cobalt based alloys	34

2.3	Stellite alloys.....	36
2.3.1	Chemical composition and microstructure.....	36
2.3.2	Tribology of Stellite alloys as potential hip implant materials.....	39
2.3.2.1	Running-in and steady-state wear of hip replacement.....	39
2.3.2.2	Wear debris particle characterization.....	41
2.3.3	Corrosion of Stellite alloys as potential hip implant materials.....	41
2.3.4	Nitrided Stellite alloys.....	42
2.4	Tribological characterization of hip implant materials.....	42
2.4.1	Wear test methods.....	42
2.4.2	Sliding wear test.....	43
2.5	Corrosion characterization of hip implant materials.....	44
2.5.1	Corrosion in bio-environment.....	44
2.5.2	Corrosion tests.....	45
2.5.2.1	Polarization.....	45
2.5.2.2	Potentiostatic test.....	49
2.5.2.3	Electrochemical impedance spectroscopy.....	49
2.5.2.4	Immersion test.....	55
3	Chapter: Microstructure Characterization.....	57
3.1	Alloy specimens.....	57
3.1.1	Chemical composition.....	57
3.1.2	Specimen preparation.....	58
3.2	Microstructural analysis.....	58
3.2.1	Test facilities.....	58
3.2.2	Microstructure and phases.....	60

4	Chapter: Wear Resistance Evaluation	81
4.1	Wear test.....	81
4.1.1	Test equipment.....	81
4.1.2	Test parameters.....	83
4.2	Experimental results.....	84
4.2.1	Wear track	84
4.2.2	Wear loss	86
4.3	Worn surface analysis.....	89
5	Chapter: Corrosion Resistance Evaluation	104
5.1	Test specimens and solution	104
5.1.1	Specimen preparation.....	104
5.1.2	Solution preparation.....	105
5.2	Electrochemical tests.....	106
5.2.1	Test setup.....	106
5.2.2	Test procedure	110
5.3	Electrochemical tests results and analysis	112
5.3.1	Open circuit potential.....	112
5.3.2	Cyclic polarization curves	113
5.3.3	Potentiostatic measurements.....	119
5.3.4	EIS results.....	123
5.4	Immersion test.....	133
5.4.1	Experimental details.....	133
5.4.2	Element concentration results and analysis	137
6	Chapter: Discussion on Results and Correlations	142
6.1	Effects of chemical composition and manufacturing process on microstructure.....	142

6.2	Effects of microstructure on wear behavior.....	144
6.3	Effects of microstructure on corrosion behavior.....	146
6.4	Corrleations among various factors.....	148
7	Chapter: Conclusions and Future Work.....	151
7.1	Summary of the research.....	151
7.2	Limitation of this research.....	153
7.3	Future work.....	153
	References.....	155

List of Tables

Table 2-1: Nominal chemical compositions (wt%, Co in balance) of various cast Stellite alloys [57].	37
Table 3-1: Chemical compositions (wt%, Co in balance) of Stellite 21 and Stellite 720.	58
Table 4-1: Pin-on-disc wear test parameters.	84
Table 5-1: Chemical composition of Hank's solution [95].	105
Table 5-2: Cyclic polarization data of the tested alloys in Hank's solution with pH 7.4 at 37°C.	118
Table 5-3: Values of equivalent circuit components.	131
Table 5-4: Cr ₂ O ₃ film thickness values on specimen surfaces at selected potentials	133
Table 6-1: Wear and corrosion results of the test alloys.	150

List of Figures

Figure 2-1: An X-ray of hip replacements: Left showing a total hip replacement and right a hip resurfacing [20].	27
Figure 2-2: Typical metal-on-polymer, ceramic-on-ceramic and metal-on-metal THR [21, 22].	28
Figure 2-3: Typical MOM hip resurfacing [33].	29
Figure 2-4: The effect of femoral head diameter upon lubrication and wear in metal-on-metal total hip replacements [38].	30
Figure 2-5: Components of volume loss for: (a) HC CoCrMo, and (b) LC CoCrMo in 50% serum, DMEM and 0.3% NaCl [42].	32
Figure 2-6: SEM images of microstructure: (a) Stellite 3 and (b) Stellite 6.	38
Figure 2-7: SEM images of microstructure of low carbon Stellite 21.	39
Figure 2-8: Typical wear characteristics of MOM hip joints: (a) volumetric wear, and (b) volumetric wear rates [63, 64].	40
Figure 2-9: Typical potentiodynamic polarization curve of a passive alloy.	47
Figure 2-10: Cyclic polarization curves for: (a) Alloy G-3, and (b) Type 317L in pH 1 sulfuric acid solution with 10,000 ppm chlorine, 1000 ppm fluorine, and 5000 ppm manganese at 50°C [84].	49
Figure 2-11: The Randles circuit model used to represent the electrochemical system of a perfect coated metal in solution [89].	50
Figure 2-12: The Randles circuit model used to represent the electrochemical system of a non-ideal coated metal or a bulk metal in solution [90].	52

Figure 2-13: Typical Bode plots: (a) for an ideal coating, and (b) for a non-ideal coating circuit [91].....	54
Figure 3-1: Tescan Vega-II XMU Scanning Electron Microscope (SEM) with an Energy Dispersive X-ray (EDX) spectroscopy system.	59
Figure 3-2: SEM microstructure of Stellite 21: (a) at low magnification, and (b) at high magnification.	61
Figure 3-3: EDX results of Stellite 21: (a) cobalt solid solution, and (b) eutectic (Cr_{23}C_6 carbide and Co solid solution).	64
Figure 3-4: SEM microstructure of Stellite 720: (a) at low magnification, and (b) at high magnification.	66
Figure 3-5: EDX results of Stellite 720: (a) Co solid solution, (b) Mo-rich carbide, and (c) primary Cr_7C_3 carbide.	69
Figure 3-6: SEM microstructure of modified Stellite 21: (a) at low magnification, and (b) at high magnification.....	71
Figure 3-7: EDX results of modified Stellite 21: (a) Co solid solution, and (b) eutectic (Cr_{23}C_6 carbide + Co solid solution).	74
Figure 3-8: SEM microstructure of nitrided Stellite 21: (a) at low magnification, and (b) at high magnification.....	76
Figure 3-9: EDX results of nitrided Stellite 21: (a) Co solid solution, (b) eutectic with Cr_{23}C_6 carbide, and (c) microdroplet.	80
Figure 4-1: Neoplus pin-on-disc tribometer system: (a) system assembly, and (b) rotating ball pin and static disc specimen.	82
Figure 4-2: Worn surface of Stellite 21 after the pin-on-disc wear test.	84

Figure 4-3: The DEKTAK 150 surface profile measuring system.	85
Figure 4-4: A schematic drawing for volume estimation of wear track.	86
Figure 4-5: Cross section profiles of wear tracks: (a) Stellite 21, (b) Stellite 720, (c) modified Stellite 21, and (d) nitrided Stellite 21.	88
Figure 4-6: Wear losses (mm ³) of the tested alloys.	89
Figure 4-7: Worn surface of Stellite 21: (a) at low magnification, and (b) at high magnification.	90
Figure 4-8: EDX spectrum of wear track in the worn surface of Stellite 21.	92
Figure 4-9: Worn surface of Stellite 720: (a) at low magnification, and (b) at high magnification.	93
Figure 4-10: EDX spectrum of wear track in the worn surface of Stellite 720.	95
Figure 4-11: Worn surface of modified Stellite 21: (a) at low magnification, and (b) at high magnification.	96
Figure 4-12: EDX spectrum of wear track in the worn surface of modified Stellite 21.	98
Figure 4-13: Worn surface of nitrided Stellite 21: (a) at low magnification, and (b) at high magnification.	99
Figure 4-14: EDX spectrum of wear track in the worn surface of nitrided Stellite 21.	100
Figure 5-1: The schematic diagram of the electrochemical test setup.	107
Figure 5-2: Electrochemical cell assembly.	109
Figure 5-3: The experimental setup for electrochemical tests.	110
Figure 5-4: OCP curves as a function of time for the Stellite alloys in Hank's solution with pH 7.4 at 37°C. For clarity, data are shown only for the first 50000 s of the exposure time.	113

Figure 5-5: Cyclic polarization curve of Stellite 21 in Hank's solution with pH 7.4 at 37°C.	115
Figure 5-6: Cyclic polarization curve of Stellite 720 in Hank's solution with pH 7.4 at 37°C.....	115
Figure 5-7: Cyclic polarization curve of modified Stellite 21 in Hank's solution with pH 7.4 at 37°C.....	116
Figure 5-8: Cyclic polarization curve of nitrided Stellite 21 in Hank's solution with pH 7.4 at 37°C.....	116
Figure 5-9: Cyclic polarization curves of Stellite alloys in Hank's solution with pH 7.4 at 37°C.....	117
Figure 5-10: Potential-pH equilibrium diagram for the deaerated chromium-water system at 25°C.....	117
Figure 5-11: Potential-pH equilibrium diagram for the deaerated cobalt-water system at 25°C.....	118
Figure 5-12: Localized corrosion resistance of the tested alloys.	119
Figure 5-13: Potentiostatic current transients for Stellite 21 and modified Stellite 21 at constant potentials of 0.2 V _{SCE} , 0.5 V _{SCE} , 0.75 V _{SCE} , and 0.9 V _{SCE} , respectively. For clarity, data are shown only for the first 600 s of the exposure time.....	121
Figure 5-14: Current densities of the tested alloys at E_{corr} for 40 hr.....	123
Figure 5-15: Calculated corrosion rates of the tested alloys.	123
Figure 5-16: Electrochemical impedance spectra at E_{corr} , 0.2 V _{SCE} , 0.5 V _{SCE} , 0.75 V _{SCE} and 0.9 V _{SCE} for Stellite 21 in Hank's solution with pH 7.4 at 37°C: (a)	

	Bode plots of impedance magnitude, and (b) Bode plots of phase angle.	
	The equivalent circuit is attached to both diagrams.	125
Figure 5-17:	Electrochemical impedance spectra at E_{corr} , 0.2 V_{SCE} , and 0.5 V_{SCE} for Stellite 720 in Hank's solution with pH 7.4 at 37°C: (a) Bode plots of impedance magnitude, and (b) Bode plots of phase angle. The equivalent circuit is attached to both diagrams.	127
Figure 5-18:	Electrochemical impedance spectra at E_{corr} , 0.2 V_{SCE} , and 0.5 V_{SCE} for modified Stellite 21 in Hank's solution with pH 7.4 at 37°C: (a) Bode plots of impedance magnitude, and (b) Bode plots of phase angle. The equivalent circuit is attached to both diagrams.	128
Figure 5-19:	Electrochemical impedance spectra at E_{corr} , 0.2 V_{SCE} , and 0.5 V_{SCE} for nitrided Stellite 21 in Hank's solution with pH 7.4 at 37°C: (a) Bode plots of impedance magnitude, and (b) Bode plots of phase angle. The equivalent circuit is attached to both diagrams.	129
Figure 5-20:	Electrochemical impedance spectra at E_{corr} for the tested alloys in Hank's solution with pH 7.4 at 37°C: (a) Bode plots of impedance magnitude, and (b) Bode plots of phase angle. The equivalent circuit is attached to both diagrams.	130
Figure 5-21:	Immersion test set-up.	134
Figure 5-22:	The Agilent Vista Pro ICP-OES instrument.	135
Figure 5-23:	ICP-OES system: (a) a schematic diagram of ICP-OES setup, and (b) a schematic diagram of the ICP torch [107, 108].	137

Figure 5-24: Cobalt ion concentrations in sample solution for the Stellite alloys after immersion tests.	138
Figure 5-25: Chromium ion concentrations in sample solution after immersion tests of the Stellite alloys.	138
Figure 5-26: Molybdenum ion concentrations in sample solution after immersion tests the Stellite alloys.	139
Figure 5-27: Nickel ion concentrations in sample solution after immersion tests of the Stellite alloys.	139
Figure 5-28: Ion concentrations in sample solutions for the Stellite alloys after 10 day immersion tests.	141
Figure 6-1: SEM image of identified carbide region in Stellite 720.	143
Figure 6-2: Microhardness test results of the Stellite alloys.	145

List of Nomenclatures

A	Cross-sectional area of wear track
C_c	Capacitance of coating
d	Thickness of oxide film
D	Diameter of wear track
E_b	Breakdown potential
E_{corr}	Corrosion potential
E_{pit}	Pitting potential
E_{pp}	Primarily passive potential
E_{prot}	Protection potential
i_{corr}	Current density
L	Applied normal load on the specimen under wear
N	Rotation speed
R_p	Polarization resistance
R_s	Solution resistance
S	Sliding distance
t	Time
V	Volume of worn material removed
Y_0	CPE parameter
Z	Impedance
α	CPE exponent
λ	Wavelength
θ	Phase angle

ρ Density of alloy
 ω Angular frequency

List of Acronyms

AC	Alternating current
ASTM	American society for testing and material
CCDs	Charge coupled devices
CE	Counter electrode
CJPR	Canadian Joint Replacement Registry
COC	Ceramic-on-ceramic
CPE	Constant phase element
DC	Direct current
EDX	Energy dispersive X-ray
EIS	Electrochemical impedance spectroscopy
FCC	Face-centered cubic
HCP	Hexagonal close-packed
HIP	Hot isostatic pressing
ICP-OES	Inductively couple plasma optical emission spectrometry
MOM	Metal-on-metal
MOP	Metal-on-polymer
OCP	Open circuit potential
RE	Reference electrode
RF	Radio frequency
SCE	Saturated calomel electrode
SEM	Scanning electron microscope

SFE	Stacking fault energy
THR	Total hip replacement
WE	Working electrode
XPS	X-ray photoelectron spectroscopy
XRD	X-ray diffraction

1 Chapter: Introduction

This chapter is an introduction to the present research, including the background, the challenges and the objectives of this research. The tasks and the methodologies adopted in this research are also described.

1.1 Background and challenges

Hip implant is a medical device that can relieve arthritis pain or fix severe physical joint damage as part of hip treatment. Technological advancements in materials, design and manufacturing techniques, have made hip replacement one of the most common, predictable and reliable orthopaedic operations, though implant duration varies widely from short term to long term. The first successful hip replacement surgery was performed over 50 years ago and now benefits millions of people every year. As younger and more active patients are suffering from unhealthy hip joints, there is an urgent demand of increasing the reliability and longevity of artificial hip implants.

One of the most important factors for well performing hip implants in human body is the material. The common material configurations for hip replacements include metal-on-polymer (MOP), metal-on-metal (MOM) and ceramic-on-ceramic (COC). Among them, MOM bearings have received accumulating attention in recent years due to their superior wear resistance, less fracture risks and longer service life expectancy in human body. MOM articulations have been conceived with the purpose of reducing wear of components ensuring longer implant duration. The most famous implant with a “first

generation” MOM articulation was developed in the early 1960’s. Conceptually it was an excellent solution for patients, but the prematurely removed implants turned out that the material, design and, mostly, manufacturing technology were the main retrieval causes of the devices [1]. In the 1970s, a group of researchers performed an extensive study on what they called “second generation” MOM articulations, directing their work in two main directions. One was to determine the wear characteristics of the bearings, and the other was to investigate the possible toxicity of the wear debris [2, 3]. Furthermore, no metallic materials are totally resistant to corrosion or ionization within the corrosive human body fluid and the corrosion products could cause local bone and soft-tissue discoloration and even remote and systemic effects [4]. Therefore, corrosion is another essential concern when choosing, designing and/or manufacturing hip implant materials. The materials used for hip implants must provide high wear resistance, strength, impact resistance and superior corrosion resistance whilst surviving in the environment of human body and not significantly altering the human physiology.

Retrieved MOM implants have been reported by orthopedic engineers and researchers all over the world [5, 6, 7, 8, 9]. The major causes of the retrievals were the loosening of the femoral head and the cup. In *vivo*, both wear and corrosion can give rise to metal debris and ion release, resulting in the prosthesis loosening. Concerns have been raised about that the debris/ions may incite biological effects on patients [10]. In some cases, the metallic wear debris from MOM implants has induced osteolytic and cytotoxic responses [11, 12]. There are also suspicions that metal ions increase the risk of implant failure by inducing hypersensitivity [13, 14, 15]. The volumetric wear rates of the metal surfaces

are strongly related to the levels of metallic ions. In light of these findings and concerns, it has been speculated that metal implants may be susceptible to prolonged corrosion [16]. Although there have been no systemic conclusions about the side effects or limit amount of the wear/corrosion products in human body, there is considerable interest in finding ways to further reduce the wear, wear debris, and corrosion ion release of MOM bearings for hip implants. Constant efforts have been made to improve the wear and corrosion performance of MOM implants.

1.2 Present research

1.2.1 Objectives

In order to improve the MOM bearing of hip implants so as to optimize their performance in human body, the present research attempted to explore new materials with improved MOM bearing for hip implant applications. Based on the common and conventional hip implant alloy, Stellite 21, which is a CoCrMo alloy containing a very small amount of carbon (0.25 wt%), two new Stellite alloys were created and characterized under wear and corrosion tests as potential hip implant materials. One is Stellite 21 with addition of ~ 10 wt%Cr, named modified Stellite 21 in this research and the other is Stellite 21 with addition of 0.4 ~ 0.6 wt%CrN, named nitrided Stellite 21. Cr has dual functions in the alloys: enhancing the corrosion resistance and strengthening the solid solution matrix and thereby increasing the wear resistance. The presence of N can promote carbide formation and thus also enhance the wear resistance. Stellite 720 is a high-carbon (2.5 wt%) Stellite alloy, or a CoCrMo alloy containing a very high level of C. It exhibits excellent wear resistance and has been employed in various practical applications, but it has never been

used for orthopedic implants. Owing to its superior tribological properties, this alloy has potential as hip implant material. Since there are two main concerns associated with hip implant materials: wear resistance and corrosion resistance in real human body environment, the modified Stellite 21, nitrided Stellite 21 and Stellite 720 were studied under series of wear and corrosion tests by simulating the real operating conditions. Conventional Stellite 21 was also tested under the same conditions for comparison or reference.

1.2.2 Tasks and methodologies

The main tasks implemented and methodologies adopted to achieve the objectives of this research are summarized below:

1. The microstructures of the four alloys were analyzed using a Tescan Vega-II XMU Scanning Electron Microscope (SEM), equipped with an Oxford Energy Dispersive X-ray (EDX) detection system for elemental analysis and quantitative mapping. Each phase in the microstructures was identified.
2. The sliding wear resistance of the alloys was evaluated on a Neoplus Pin-On-Disc Tribometer. The volume losses of each specimen after the wear test were evaluated utilizing a DEKTAK 150 surface profile measuring system. The worn surfaces of the specimen were analyzed using the SEM/EDX system.
3. Electrochemical tests were conducted on each of the alloys to investigate their corrosion behavior in simulated human body fluid, Hank's solution with pH 7.4 at the temperature of 37°C. Open circuit potential (OCP), cyclic polarization, potentiostatic and electrochemical impedance spectroscopy (EIS) tests were

performed on these alloys in the solution to obtain the data of localized pitting potential, general corrosion rate and oxide film growth.

4. In order to further study the corrosion behaviour of these alloys in the solution, immersion test, which is considered as a traditional approach for corrosion research of materials, was also conducted on these alloys in the same solution for 1, 2, 5, and 10 days, respectively. The ion release concentrations in the solution were quantified using an inductively couple plasma optical emission spectrometry (ICP-OES) instrument.
5. The experimental results were analyzed and discussed, including the influence of chemical composition and manufacturing process on the microstructure, wear resistance and corrosion behaviour of these alloys. The correlations among these properties were discussed.
6. The experimental results, discussion and correlations were integrated to assess the applicability of these alloys as potential hip implant materials.

1.3 Organization of the thesis

This thesis is a comprehensive report of the present research, which summarizes the main aspects or contents involved in the research. It consists of seven chapters that cover the introduction of this research, literature review related to this research, microstructure analysis, wear resistance test and evaluation, corrosion resistance test and evaluation of the four alloys being studied, discussion on the results, as well as conclusions and future work of this research. The contents of each chapter are summarized below:

Chapter 1 is an introduction to the present research, including the background, the challenges and the objectives of this research. The tasks committed and the methodologies adopted in this research are described. The structure of this thesis is outlined at the end of this chapter.

Chapter 2 is the literature review, covering a brief introduction of hip implants, concerns for hip implants, and metallic biomaterials employed as hip implants, especially Stellite alloys including their chemical composition, classification, microstructure, and various properties such as tribological, mechanical and corrosion properties that were investigated in previous research. The methods commonly used for wear and corrosion studies of materials are also summarized in this chapter.

Chapter 3 reports the procedure and results of the microstructural analysis on these alloys. The specimen preparation steps are described in details. Both SEM

microstructure images and EDX spectra for each alloy specimen are presented. The results are analyzed.

Chapter 4 reports the details of the wear test facilities, test procedure and parameters as well as the test results. The cross-section profiles of wear track are presented and the wear losses of the alloys are plotted. The SEM morphologies and EDX spectra of the worn surfaces for each specimen are provided and analyzed.

Chapter 5 presents the details of the corrosion tests, including specimen and solution preparation for the corrosion tests, test setup, experimental procedures and test results. The corrosion tests consist of electrochemical tests and immersion test. The data from these tests on each alloy are plotted and analyzed.

Chapter 6 is the discussion on the experimental results, focussing on the effects of chemical composition and manufacturing process of these alloys on their microstructure, wear and corrosion behaviour in the designated test conditions. The correlations among these results are analyzed and reported.

Chapter 7 summarizes this research. The conclusions drawn from this research are provided. The future work towards to the goals of the entire project is recommended.

2 Chapter: Literature Review

This chapter is an intensive literature review, covering a brief introduction of hip implants, concerns for hip implants, and metallic biomaterials employed as hip implants, especially Stellite alloys. The focus of this literature review was on the wear and corrosion performances of Stellite alloys for MOM bearings under *in vivo* and *in vitro* body environments.

2.1 Hip implants

2.1.1 Function and structure

Human hip joint is the body's largest ball-and-socket joint that offers a great support of the body's weight and force. It is also able to withstand repeated movements such as walking, running, and jumping without great wearing and tearing in human body fluid environment [17, 18]. Arthritis and hip fracture are among the most common causes of hip pain, which often happen in elder adults, while tendinitis and tendon strain are more likely to occur in younger and more active generation due to the repeated activities and overuse [17]. It was reported by the Canadian Joint Replacement Registry (CJPR) that a 62.7% increase of hip joint replacement surgery took place in one decade from 1996 (15,214 cases) to 2006 (24,253 cases) [7]. Moreover, another review by the CJPR in 2003 reported that 1.7% of 58,351 patients had suffered hip implant revision within one year [19]. Therefore, there is an urgent need for improved hip implants with superior corrosion and wear resistance, outstanding biocompatibility as well as longevity.

There are two types of hip replacements: total hip replacement (THR) and hip resurfacing, as shown in Figure 2-1.



Figure 2-1: An X-ray of hip replacements: Left showing a total hip replacement and right a hip resurfacing [20].

In the THR, the head of femur is thoroughly cut away and replaced by a metal stem with a ball on the top of the stem. Due to the great weight loss, the THR is mostly suggested to be applied on elderly or inactive patients. In the THR, metal-on-polymer (MOP), ceramic-on-ceramic (COC) and metal-on-metal (MOM) material configurations are commonly adopted, as seen in Figure 2-2.

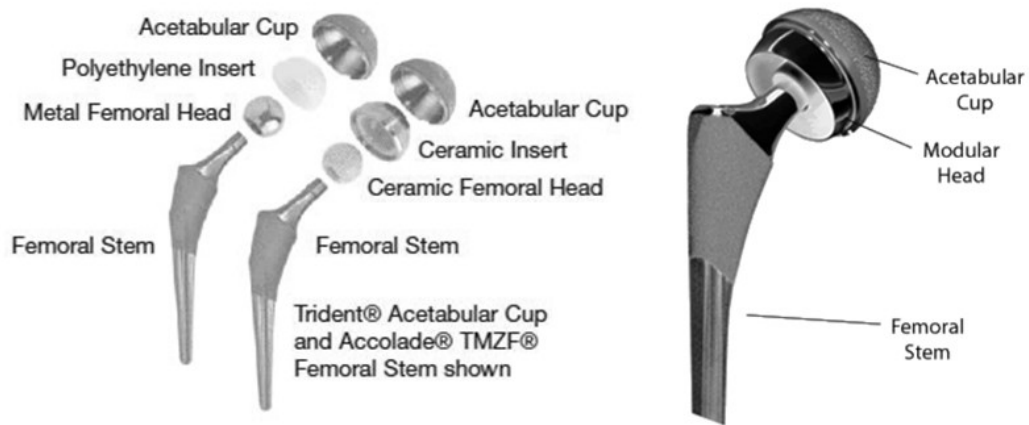


Figure 2-2: Typical metal-on-polymer, ceramic-on-ceramic and metal-on-metal THR [21, 22].

The MOP THR was first employed in the early 1960s and had been used as one of the most popular hip joint replacements during the last few decades because of its low costs [23, 24, 25]. However, the side effects of the MOP THR were poor wear resistance and thus excessive debris could be released to the human body fluid [25, 26, 27]. The COC THR merited industry's attention since it could lead to the lowest amount of wear debris. However, the major drawback of COC THR was found to be catastrophic fragile fracture [25, 28]. In recent years, the MOM THR has generated continuous interest because of its much lower amount of wear debris when compared to the MOP THR. In addition, the MOM THR allows larger femoral head diameter which can reduce hip dislocations, avoiding high risk of fracture associated with the COC THR [29]. However, prior studies also showed a significantly higher metal ion release of the MOM THR in comparison with the other two types of THR. Further studies associated with wear and corrosion behavior of MOM bearings are in an urgent need to ensure that the released ions in human fluid will not result in accelerated osteolysis and implant retrievals [30].

Based on the MOM THR system, the alternative hip replacement, known as hip resurfacing (Figure 2-3), is usually implanted in younger, active patients since less femur bone is removed [31]. Also, easier revision surgery can be done due to the remaining of more original bone stock [32]. However, hip replacing is a relatively new member in the implant market and the long-term outcome data is therefore not available.



Figure 2-3: Typical MOM hip resurfacing [33].

2.1.2 Concerns for MOM hip implants

2.1.2.1 MOM bearing structure

MOM bearings are drawing more attention of researchers because of their low-wear rates. It is recognized that lubrication is one of the most important factors that affect the amount of wear debris [34, 35]. As mentioned above, the hip joints are subjected to various loads due to movements such as walking, running and jumping. When the loads are applied on the bearing surfaces, two distinct situations can be observed with respect to the modes of lubrication, which are called the regimes of lubrication. One is the mixed regime where the generated lubricant (joint fluid) film completely separates the surfaces and the other is the boundary regime where the load is carried by the surface asperities rather than by the

lubricant [36, 37]. Studies have shown that by improving the lubrication regime and lubrication film thickness, the wear rate can be reduced significantly [36, 38, 39]. It has been reported that the larger femoral head size and the smaller clearance between the femoral head and the acetabular cup can optimize the lubrication. Figure 2-4 shows that as the diameter of the femoral head increases, the lubrication regime develops from the boundary mode to the mixed mode, resulting in reduced wear loss. Furthermore, a small clearance has been shown to improve the conformity between the two bearing surfaces and consequently the lubrication. If the clearance is too large, the lubrication regime can shift from the mixed mode back to the boundary mode [40].

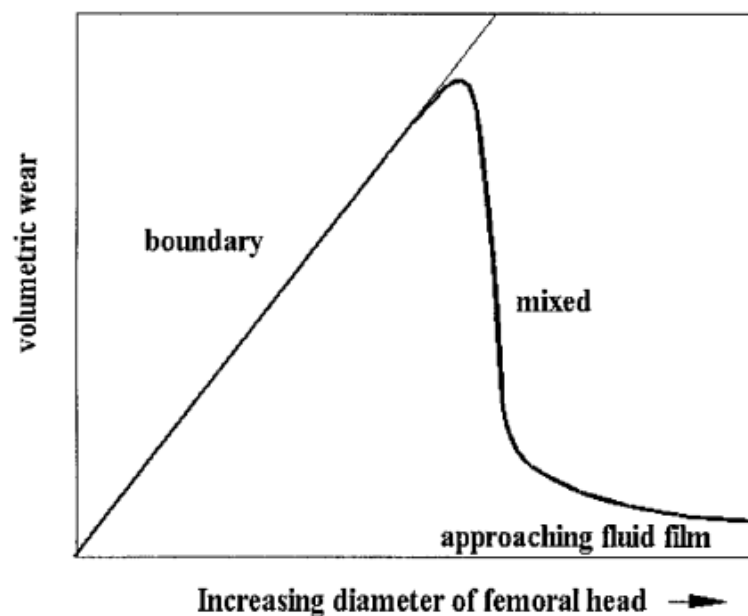


Figure 2-4: The effect of femoral head diameter upon lubrication and wear in metal-on-metal total hip replacements [38].

2.1.2.2 Wear and corrosion behavior

As most of hip implants serve in human body for at least 10 ~ 15 years, they are subjected to corrosion due to their contact with biological tissues and the wear caused by

mechanical actions, which result in metallic ions and wear debris release. Loosening between the femoral head and acetabular cup therefore occurs because of the material loss. It is commonly associated with pain and can cause the premature failure of the implants. It is agreed that a corrosive environment accelerates the wear, and that chemical reactions are stimulated by the presence of friction and wear [41]. The wear debris and corrosion ion release are usually induced simultaneously. According to the study of Yan *et al.* [42], the total material loss (T) can be described by the following equation:

$$T = W + C' + S, \quad (2.1)$$

where W is the material wear loss in the absence of corrosion, C' is the material corrosion loss in the absence of wear, and the synergy S includes two components which are the effect of wear on corrosion (C_w) and the effect of corrosion on wear (W_c). Two types of MOM materials, including wrought high carbon (HC) CoCrMo and wrought low carbon (LC) CoCrMo were investigated in three different fluids (i.e., 50% calf bovine serum, Dulbecco's Modified Eagle's Medium (DMEM), and 0.3% NaCl solution) at 37°C using a pin-on-reciprocating plate tribometer. Figure 2-5 shows that about 22%~50% of the material loss was attributed to corrosion-related effects. In other words, wear-related material loss was the main contribution to the released wear debris/metallic ion particles. Furthermore, it can be seen from Figure 2-5 that, for CoCrMo alloys, if the carbon content was increased, the wear-related material loss would be the main factor affecting the tribocorrosion behavior.

Many studies have shown that wear debris and metallic ions can cause possible adverse health effects [8, 15, 43, 44, 45]. As learned from these studies, possible adverse health effects can be caused by accumulated metal particles including osteolysis, inflammation, pain, and pseudotumours. On the other hand, the pathological effect of metallic wear particles has been found to be insignificant in some investigations [46, 47]. No systemic conclusions about the side effects or limit amount of the wear/corrosion products in human body have been drawn, however, it is generally agreed that the less the particles are released in human body, the better service the MOM implant can provide.

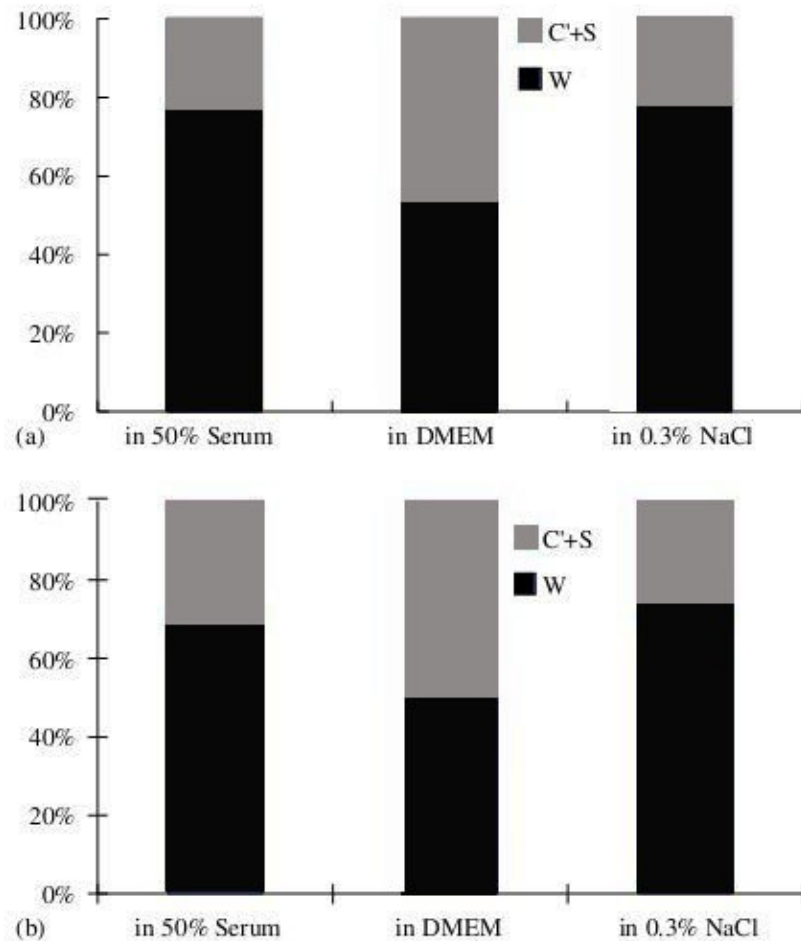


Figure 2-5: Components of volume loss for: (a) HC CoCrMo, and (b) LC CoCrMo in 50% serum, DMEM and 0.3% NaCl [42].

2.2 Metallic materials for hip implants

There are three types of metallic materials commonly employed as hip implants: stainless steel, titanium and its alloys and cobalt-chromium alloys [6].

2.2.1 Stainless steel

The application of stainless steel as implants can be dated back to 1920s [48]. The main alloying elements in the iron based surgical stainless steel are chromium, nickel and molybdenum, which provide fairly uniform corrosion resistance, homogeneous finish as well as good hardness property. Studies have shown that the presence of chromium oxide film dramatically improves the corrosion resistance and fatigue strength of surgical stainless steel in aggressive corrosive environment [49]. ASTM 316 stainless steel and 316L stainless steel (L stands for lower carbon), containing 16 - 18% chromium and 0.03 - 0.08% carbon, are the most popular implant materials for a long period of time. The lowering of carbon content in stainless steels keeps them from forming chromium carbides because these carbides usually cause intergranular corrosion. On the other side, these carbides also make the steels with limited superiority in load-bearing due to reduced strength. Pitting and crevice corrosion attacks found in retrieved stainless steel implants also limit the application of these steels as temporary MOM bearings [5]. Surgical stainless steel is also commonly used in developing countries because of its cost-effective advantage.

2.2.2 Titanium and its alloys

Titanium and its alloys became to draw worldwide attention as hip joint replacement materials since 1970s. Their outstanding corrosion resistance (thick passive oxide film), lower density and higher modulus match with human bone make them a superior alternative as implant materials when compared with other types of alloy [50]. However, it was reported that titanium and its alloy hip joint implants could be damaged due to their low fatigue strength [51]. In return, the damage accelerated pitting propagation in the material surface, deriving a high level of aseptic loosening and tissue discoloration.

2.2.3 Cobalt based alloys

Since the first usage as biomaterial in 1930s as an alternative to gold in surgery, cobalt-based alloys, specifically CoCrMo alloys, have been notably applied in hip replacements [52]. By virtue of their high fatigue strength, cobalt-based alloys are a better option for MOM bearing components when compared to stainless steels and titanium alloys [53]. In addition, the presence of element chromium can form chromium-rich oxide film on the alloy surface in an aqueous environment, which permits excellent corrosion resistance [54, 55]. The mechanical strength of cobalt-based alloys is enhanced by formation of chromium-carbide, which guarantees minimum amount of wear debris, compared to other alloys. There are primarily two categories of cobalt-based alloys for biomaterials in consideration of manufacturing methods: wrought alloys and cast alloys. The wrought CoNiCrMo alloy is newly applied on medical implant while the cast cobalt-based alloy has been used as artificial joints for a long time [56].

Cobalt exhibits two crystal structures. The hexagonal close-packed (HCP) crystal structure is thermodynamically stable from room temperature or human body temperature to 417°C. The face-centered cubic (FCC) crystal structure with a very low stacking fault energy (SFE) forms from 417°C and above. Due to the instability, the FCC structure can only completely transform to HCP structure at 417°C if cooled down extremely slowly [57]. However, in practical conditions, the cobalt-based alloys applied as hip implant materials are mostly cooled down at a high rate, which turns out that the FCC structure of cobalt and its alloys is usually mixed with the HCP structure at the human body temperature [57, 58]. HCP structure transformation can be triggered by mechanical stress or time at elevated temperatures. For instance, it is verified that such structure is found on the surface of pin-on-disc wear test specimens and retrieval hip joint implants [57, 59]. The unstable FCC structure and its associated low SFE are found to result in high yield strength, high work-hardening rate as well as less susceptible to fatigue under cyclic stresses. In addition, the transformation to HCP structure may also generate outstanding resistance to cavitation and erosion-corrosion of cobalt-based alloys [57]. Additions of alloying elements such as Ni and C promote the stability of the FCC structure at high temperatures up to 1495°C, which increase the SFE of the Co-rich solid solution matrix. Adversely, Cr, Mo and W offer stability of HCP structure at low-temperatures, which results in better corrosion resistance [60].

2.3 Stellite alloys

2.3.1 Chemical composition and microstructure

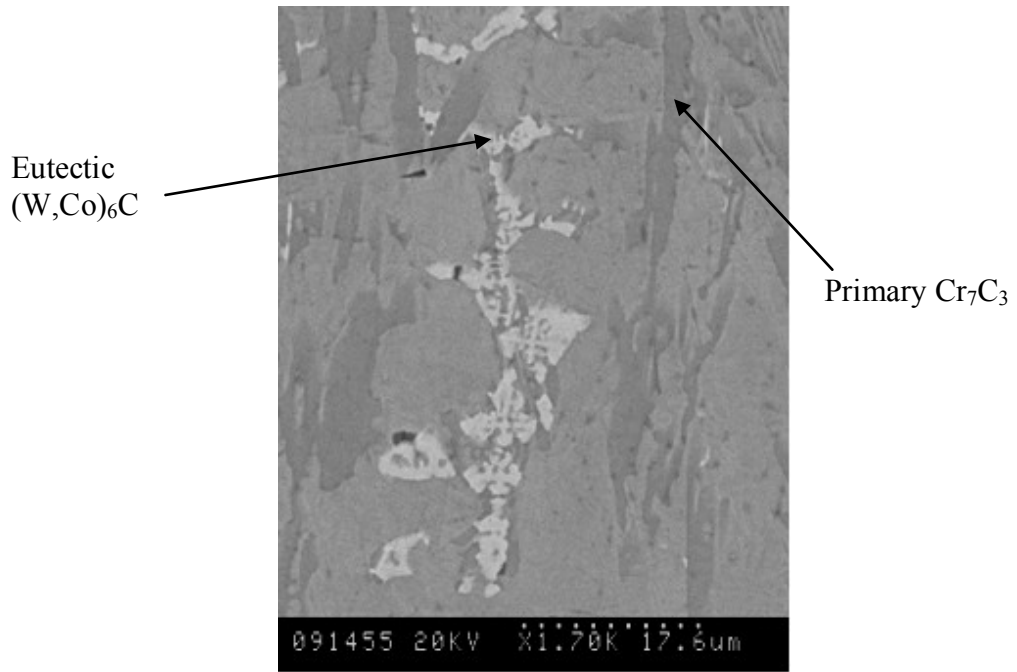
Stellite alloys are a family of cobalt-based alloys with main alloying elements being Cr, W or/and Mo, and also minor C [57]. Historically, Stellite alloys were investigated and named by Elwood Haynes in the Deloro Stellite Company around 1882 [57, 61]. Among the cast Stellite alloys, Stellite 21 is the only alloy that is commercially used as hip implant material. To improve the performance and extend the service life of hip implants, investigation of other cast Stellite alloys as potential hip implant materials is needed.

Table 2-1 lists the nominal chemical compositions of various Stellite alloys that are commonly used in different fields [57]. It is shown that Stellite alloys contain a certain level of carbon to encourage the formation of carbides in the microstructure during alloying solidification. The other three main alloying elements are Cr, W and Mo. Depending on the contents of the alloying elements of C, different amounts and types of carbides form in these alloys. For example, Stellite 3 with a high C level of 2.4 wt% has a microstructure of primary Cr-rich M_7C_3 carbides in an interdendritic eutectic matrix with solid solution and W-rich M_6C carbides, as shown in Figure 2-6, whereas hypo-eutectic Stellite 6 with 1wt%C consists of primary Co dendrites with eutectic Cr-rich M_7C_3 carbides network. Unlike Stellite 1, Stellite 3 and Stellite 6, low-carbon Stellite 21 and Stellite 22 employ molybdenum instead of W to strengthen the solid solution. The Cr-rich $M_{23}C_6$ carbides are often formed in low-carbon Stellite alloys [57], as shown in Figure 2-7. The 700 series (alloys 703, 706, 712, 720 in Table 2-1) alloys

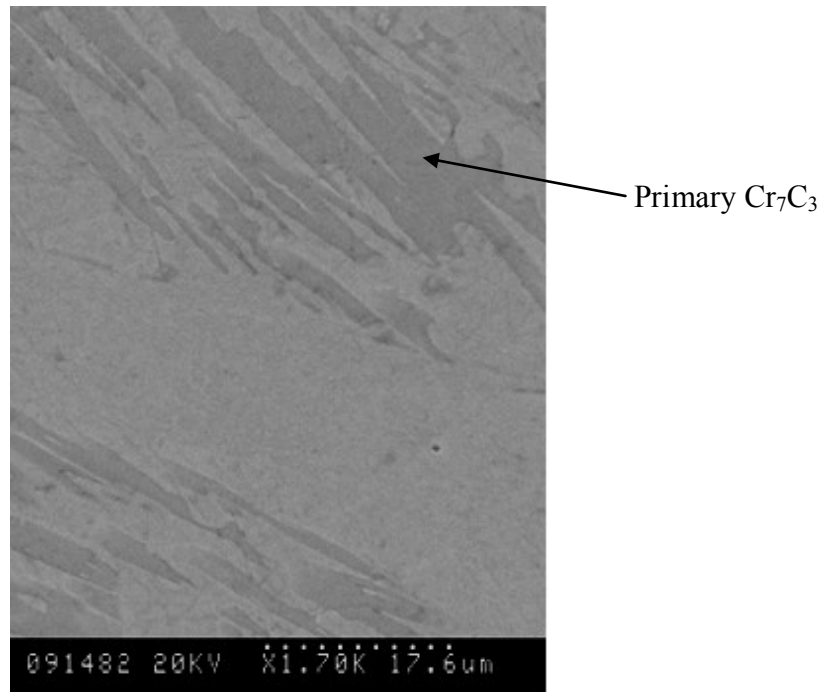
are the most recently developed alloys in the Stellite family. Similar to Stellite 21 and Stellite 22, the W is replaced by 5 - 18 wt%Mo [57].

Table 2-1: Nominal chemical compositions (wt%, Co in balance) of various cast Stellite alloys [57].

Alloy	Cr	W	Mo	C	Fe	Ni	Si	Mn	Others
Stellite 1	30	13	0.5	2.5	3	1.5	1.3	0.5	
Stellite 3	30.5	12.5		2.4	5	3.5	2	2	1B
Stellite 4	30	14	1	0.57	3	3	2	1	
Stellite 6	29	4.5	1.5	1.2	3	3	1.5	1	
Stellite 12	30	8.3		1.4	3	1.5	0.7	2.5	
Stellite 21	27		5.5	0.25	3	2.75	1	1	
Stellite 20	33	17.5		2.45	2.5	2.5		1	
Stellite 22	27		11	0.25	3	2.75	1	1	
Stellite 25	20	15		0.1	3	10	1	1.5	
Stellite 31	22	7.5		0.5	1.5	10	0.5	0.5	
Stellite 80	33.5	19		1.9					1B
Stellite 188	22	14		0.1	3	22	0.35	1.25	0.03La
Stellite 190	27	14	1	3.3	3	3	1	1	
Stellite 300	22	32		1.5					
Stellite 694	28	19		1	5		1	1	
Stellite 703	32		12	2.4	3	3	1.5	1.5	
Stellite 706	29		5	1.2	3	3	1.5	1.5	
Stellite 712	29		8.5	2	3	3	1.5	1.5	
Stellite 720	33		18	2.5	3	3	1.5	1.5	0.3B



(a)



(b)

Figure 2-6: SEM images of microstructure: (a) Stellite 3 and (b) Stellite 6.

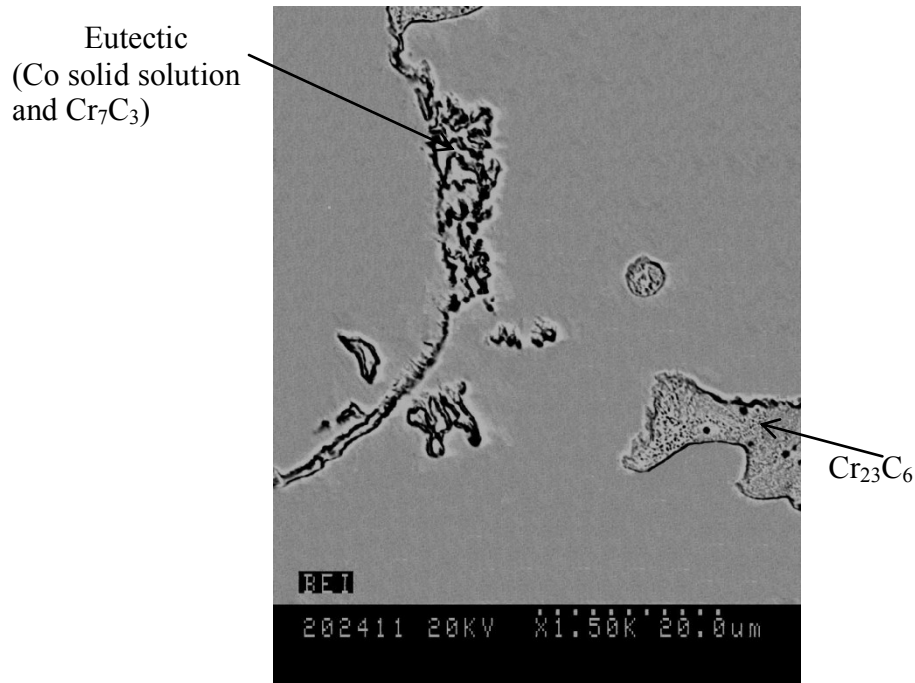
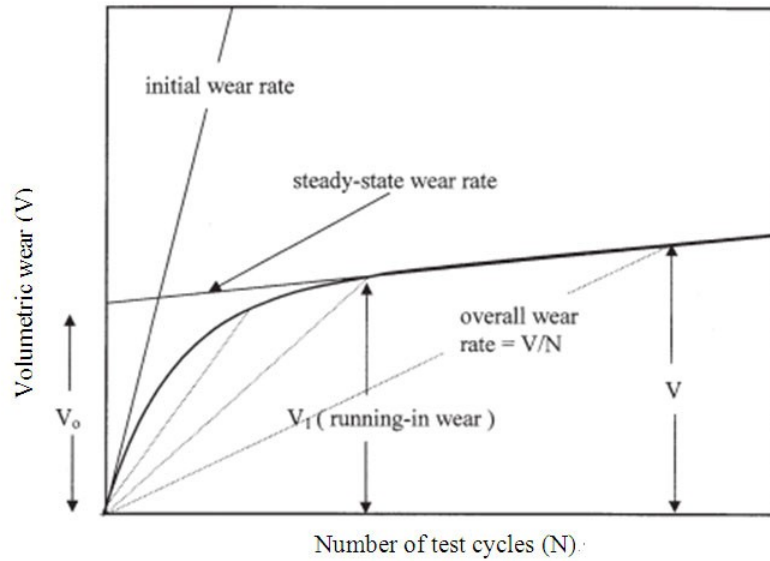


Figure 2-7: SEM images of microstructure of low carbon Stellite 21.

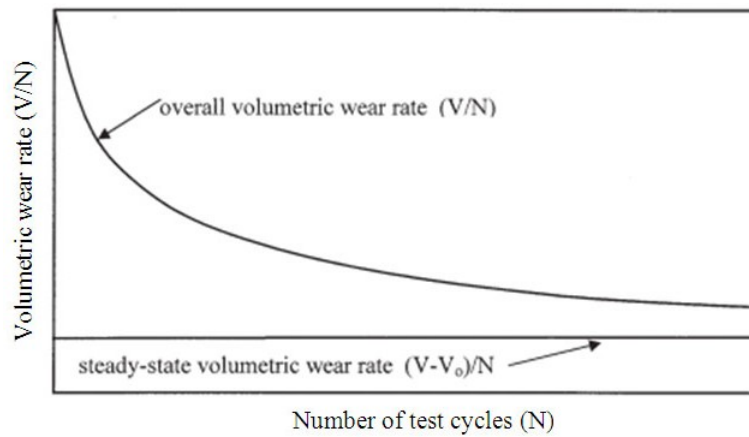
2.3.2 Tribology of Stellite alloys as potential hip implant materials

2.3.2.1 Running-in and steady-state wear of hip replacement

Wear behavior and characteristics of MOM hip joints can be described by the diagrams in Figure 2-8. There are two distinct stages during the wear of hip replacements. The running-in or bedding-in period exhibits relatively high wear rate within the first million test cycles. This is followed by the steady-state stage when the volumetric wear rate becomes steady and much lower. Although the running-in wear only occupies a small portion of the overall MOM hip joints wear life, it is more likely to generate wear debris (V_1 out of V), initiate fracture and cause ion release [62].



(a)



(b)

Figure 2-8: Typical wear characteristics of MOM hip joints: (a) volumetric wear, and (b) volumetric wear rates [63, 64].

Studies showed that at the running-in wear stage, the hard Cr-rich carbides between CoCrMo materials came into contact, avoiding the softer matrix-on-matrix abrasion thus causing large amounts of wear debris. Hernández-Rodríguez *et al.* [65] found that the carbide volume fraction had a dominant influence on the wear resistance of the bearing

surfaces. With the same chemical composition, the as-cast microstructure containing blocky-shape carbides or the carbide precipitates had a larger carbide volume fraction thus resulting in less amounts of debris under wear. On the other hand, the partial/complete solution microstructure after heat treatment exhibited smaller carbide size and a reduction in visible carbides in the solution matrix [65, 66, 67, 68].

2.3.2.2 Wear debris particle characterization

As mentioned above, the wear rate of MOM bearings is at least 20 times lower than the MOP bearings. Furthermore, the volumetric concentration of wear particles released from the MOM bearings is also significantly reduced. However, the calculated number of wear particles is higher than for the same volume of MOP wear which indicates smaller sizes of wear particles [8]. A study of retrieved hip implants (cast Stellite 21) from 10 patients reported the wear particle characterizations in terms of size and shape [69]. The particles were classified as round, oval and needle-shaped with a predominance of round to oval-shaped particles. The particle lengths ranged from 10 ~ 400 nm with a majority between 5 ~ 20 nm, which were similar to those reported by other researchers [70, 71, 72]. The wear particles were believed to be associated with tissue necrosis [73], hypersensitivity [74] and genotoxicity [75].

2.3.3 Corrosion of Stellite alloys as potential hip implant materials

Chromium-rich oxide film Cr_2O_3 is the major constituent of the passive film on the surface of Stellite alloys, which effectively resists further corrosion of the alloys in human body fluid. The minor constituents including Co-, Mo- and Ni-oxides are also found on the outside layer of the film [76]. The oxide film varies in film thickness,

chemical composition and oxidation state. When the oxide film is disrupted by change of pH values, reducing/oxidizing potential changes, corrosion proceeds and metal ions are released continuously unless the film is regenerated. Therefore, the repassivation ability of Stellite alloys plays an important role in inhibiting rapid corrosion process and metal ion release [53]

2.3.4 Nitrided Stellite alloys

As hip replacements are required to bear high loads, plasma nitriding is another attempt to increase the wear resistance of surgical Stellite alloys. It has been proved by several researchers that the wear losses of surface-nitrided Stellite alloys can be reduced by a factor of 10 under sliding wear tests when compared to those of untreated Stellite alloys [77, 78, 79]. However, some other comparative studies obtained the opposite corrosion results with the reasons of the heavy ion bombardment and the surface roughening of the nitrided alloys [80, 81]. Further investigation is therefore needed to verify the nitriding effect on the wear and corrosion behavior of Stellite alloys.

2.4 Tribological characterization of hip implant materials

2.4.1 Wear test methods

The tribological behavior of hip implants can significantly affect their performance in human body. Therefore, the tribological properties of hip implant materials must meet the requirements for hip implants. A wide range of methods have been developed and employed to investigate the wear behavior of the MOM hip replacements, but two commonly used systems are pin-on-disc tribometer and hip joint simulator. The pin-on-

disc method provides informative results about the wear loss and friction coefficient of the tested material under dry wear condition with pre-set contact load, sliding speed and distance. The hip joint simulator can model or predict the load and lubrication as well as the motion patterns for the conditions of human hip joints [63]. The hip joint simulator is far more expensive and time consuming when compared to pin-on-disc tribometer.

2.4.2 Sliding wear test

In the context of hip joint tribology, adhesive wear is one of the major wear mechanisms between the acetabular cup and the femoral head. Adhesive wear, or sliding wear, occurs when one solid surface slides over the other under a certain load. At room temperature, the softer surface undergoes loss of dimensions due to plastic deformation, giving rise to high friction with its counter surface and eventually generating small flakes, leading to wear of the materials [57]. The sliding wear mechanism is a function of several variables that include type of materials involved, applied load, temperature, wear duration, and sliding speed.

The Archard equation [82] provides a basic concept to predict and analyze the wear loss of a material, which is commonly applied to the sliding wear system. The Archard equation suggests that the wear volume loss V (mm^3) is in direct proportion to the applied normal load L (N), and the sliding distance S (mm) and in inverse proportion to the hardness H of the tested material.

$$V = k \frac{LS}{H}, \quad (2.2)$$

where k is known as the dimensionless wear coefficient normally less than 1.

2.5 Corrosion characterization of hip implant materials

Corrosion of metals is an electrochemical process where the materials are gradually ionized. When metallic materials are implanted, special concern on corrosion should be paid because of the hostile electrolytic environment of hip joints. A healthy hip joint fluid is an oxygenated saline solution with salt content of about 0.9% at pH ~7.4, and temperature of $37\pm 1^\circ\text{C}$ [83].

In vitro and *in vivo* are commonly employed to investigate the corrosion behavior of biomaterials. *In vivo* is experimentation using a whole living organism where animal testing and clinical trials are two common forms. However, due to the high cost of *vivo* experiments, *in vitro* is applied as the controlled environment, which can represent similar environment of the real situation [84]. The corrosion resistance of metallic implants is recommended to be qualified by simple immersion or electrochemical methods *in vitro*.

2.5.1 Corrosion in bio-environment

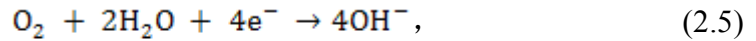
The metal ion release of hip implants in human body due to corrosion can give rise to surrounding tissue blackening and implant loosening. It is therefore necessary to understand the kinetics of corrosion in the hip joint fluid of human body. The electrochemical reactions that occur on the surface of Stellite alloys in a bio environment are similar to those observed during exposure to seawater [83]. The metal is ionized

while the oxygen is reduced to hydroxyl ions. The total rate of oxidation must equal the total rate of reduction when the corrosion takes place.

Anodic reaction:



Cathodic reaction:



where the chromium ions Cr^{n+} can be Cr^{3+} or Cr^{6+} [85, 86]. The studies have shown that the release ions Co^{2+} , Cr^{3+} and Cr^{6+} lead to the reduction of the number of cells and the failure of osseo-integration of bone onto the fixation surface [85].

2.5.2 Corrosion tests

2.5.2.1 Polarization

When a metal is implanted, a natural electrochemical cell forms. Both oxidation and reduction reactions occur through the metal-electrolyte interface. *In vitro*, the anodic/cathodic current is monitored to observe the corrosion process. If the oxidation rate equals the reduction rate when no external potential load is applied, the net current is zero in the interface. The equilibrium potential in this situation is called open circuit potential (OCP) or corrosion potential (E_{corr}). The potential measured is relative to the reference potential.

Polarization methods, including potentiodynamic polarization, potentiostaircase, and cyclic voltammetry, are often used for *in vitro* corrosion tests. These techniques can provide important information regarding the corrosion mechanisms and susceptibility of specific materials to corrosion in designated environments. Figure 2-9 shows a typical potentiodynamic polarization curve of a passive alloy. The scan starts from point 1 and shifts in an anodic, or noble, direction until it ends at point 2. A number of features of the curve should be noticed. The OCP or E_{corr} rests at point A where it corresponds to corrosion current i_{corr} . At this point, the measured current should be close to zero as the sum of the anodic and cathodic reaction rate are equal to each other. As the potential increases, the curve moves to region B, which is defined as active region. In this region, the oxidation reaction overrates the reduce reaction and causes corrosion proceeding. The potential at point C is so-called primarily passive potential E_{pp} where the current begins to decrease while the potential increases. With the active-passive transition in region D, region E is known as the passive region. The corrosion process is resisted due to the formation of oxide film in this region. The oxide film is damaged at point F when the potential reaches a certain positive value, termed as pitting potential E_{pit} or breakdown potential E_b . Furthermore, it is known as the tranpassivative region when the applied current starts to increase rapidly throughout region G. It should be mentioned that a real potentiodynamic polarization curve may have some, not necessary to have all, of the features described above.

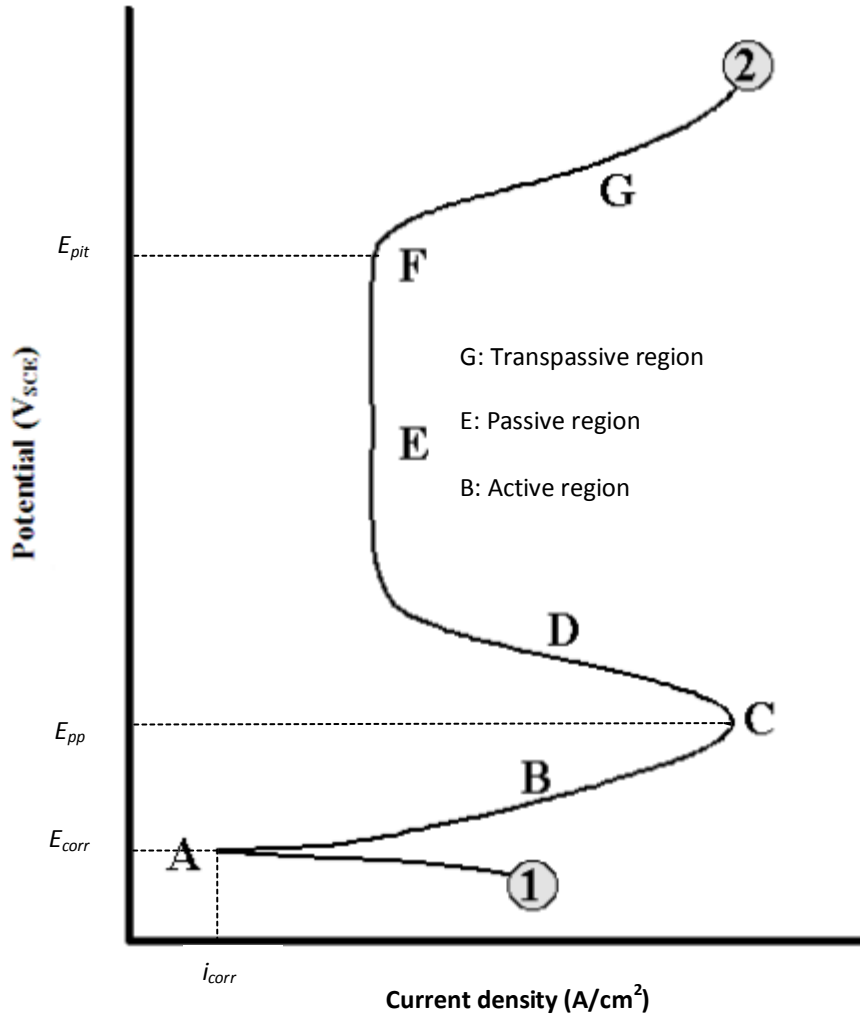
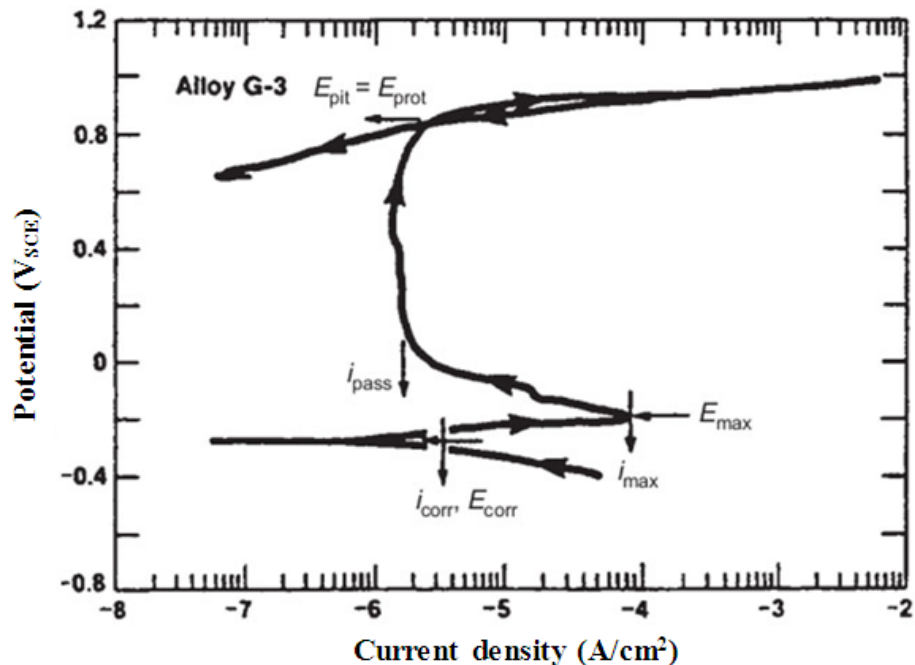


Figure 2-9: Typical potentiodynamic polarization curve of a passive alloy.

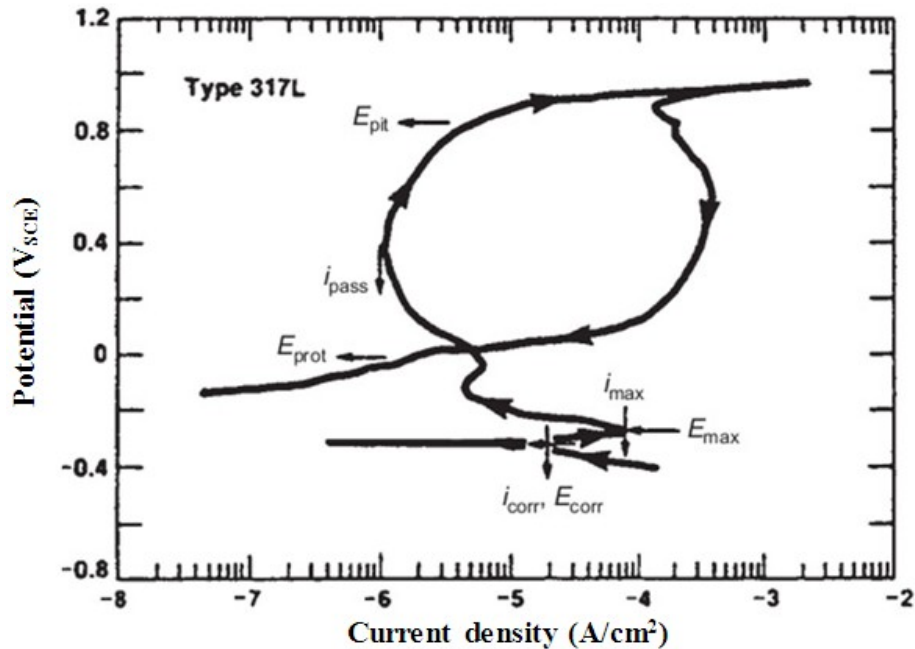
From the potentiodynamic polarization curve, the corrosion behavior of the material can be predicted. The less the difference between the values of E_{pp} and the E_{corr} , the more likely the material is to be passive. A lower current density indicates quicker passivation and better corrosion resistance of the material.

Cyclic polarization involves sweeping the potential in an anodic direction until a predetermined value of current or potential is reached, then the scan is immediately reversed toward more cathodic values until the original value of potential is reached, and

the reverse scan is also called hysteresis loop. The existence of hysteresis is usually indicative of pitting, while the size of the loop is often related to the amount of pitting. As can be seen in Figure 2-10, the hysteresis behavior on the reverse scan between stainless steel 317L and alloy G-3 is very different. The nominal composition of type 317L is 19%Cr, 13%Ni, 3.5%Mo, 1.8%Mn, and 0.03%C (in weight), whereas the nominal composition of alloy G-3 is 22%Cr, 44%Ni, 7%Mo, 1.9%Cu, 5%Co, 1.3%W, 0.3%Nb plus Ta, and 19.6%Fe (in weight). There is little or no hysteresis loop for alloy G-3, whereas a large hysteresis loop is found for stainless steel 317L. The values of pitting potential E_{pit} , and protection potential E_{prot} , where the passivity will be re-established after broken down, are nearly identical for alloy G-3. A more positive E_{prot} value and a small difference between E_{pit} and E_{prot} indicate better resistance to localized corrosion.



(a)



(b)

Figure 2-10: Cyclic polarization curves for: (a) Alloy G-3, and (b) Type 317L in pH 1 sulfuric acid solution with 10,000 ppm chlorine, 1000 ppm fluorine, and 5000 ppm manganese at 50°C [84].

2.5.2.2 Potentiostatic test

For potentiostatic approach, the potential can be forced to shift in an anodic or cathodic direction as practically required while the specimen only sits at E_{corr} in a traditional immersion test. The corrosion current at certain potential during a certain period of time can be investigated in real time. The uniform corrosion rate of the material then can be calculated from the results of electrochemical measurements.

2.5.2.3 Electrochemical impedance spectroscopy

Electrochemical impedance spectroscopy (EIS) is a non-destructive technique that can be applied to investigate the specimen properties in the simulated human body environment

by driving a small, sinusoidal, alternating current (AC) or voltage over a range of frequencies [87]. The electrochemical response of the system is measured and analyzed over this range of frequencies.

When an intact coated or bulk metal is immersed in aqueous, conductive and ionic solution, a simple equivalent electrical circuit, Randles circuit, is commonly interpreted on the basis of the circuit generated on the electrode/electrolyte interface [88]. In the case of an imperviously coated metal, the coating acts as a perfect capacitor so that the charge built between the substrate and the electrolyte could not pass through it. The electrochemical system is therefore fitted to the circuit shown in Figure 2-11. This equivalent circuit model consists of a resistor in series with a parallel RC (resistor and capacitor in parallel). R_s represents the electrolyte resistance, C_c is the capacitance of the coating and R_p is the polarization resistance.

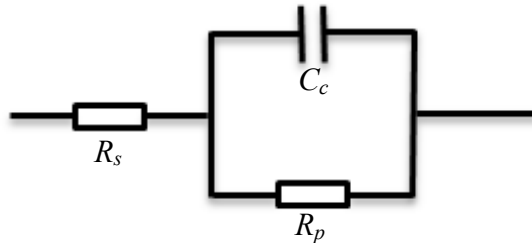


Figure 2-11: The Randles circuit model used to represent the electrochemical system of a perfect coated metal in solution [89].

When a sine alternating voltage (V) of varying frequency (ω) is applied on the cell, the resistors R_s and R_p are independent of frequency, indicating no time lag and a phase angle θ of zero in the corresponding current. Unlike the resistors, the current of the coating

capacitor is -90° out-of-phase with the voltage, which means that the sine potential waveform leads to a cosine current waveform. The higher the frequency, the faster the voltage changes, and the higher the magnitude of current is on the capacitor. According to Ohm's law, the impedance of the capacitor is a ratio of the AC voltage to the current. Therefore, when the frequency reaches the maximum, the capacitor impedance tends to be very small. On the other hand, when the frequency approaches to zero, the impedance becomes infinity. The impedance of a capacitor can be expressed as a complex function:

$$\begin{aligned}
 Z_C &= Z_{real} + Z_{imaginary} \\
 &= 0 + \frac{1}{j\omega C} \\
 &= \frac{1}{j\omega C}, \tag{2.6}
 \end{aligned}$$

where Z_{real} is the real component of the impedance, and $Z_{imaginary}$ is the imaginary component. $j = \sqrt{-1}$, ω is the angular frequency ($\omega = 2\pi f$), and C is the capacitance of the capacitor which can be calculated as [87]:

$$C = \frac{\varepsilon \varepsilon_0 A}{d}, \tag{2.7}$$

where A is the surface area, ε is the dielectric constant of coating material, ε_0 is 8.854×10^{-12} F/m, and d is the thickness of the coating.

For the ideal capacitor circuit model, the total impedance is expressed as:

$$\begin{aligned}
Z(\omega) &= R_S + \left(\frac{1}{\frac{1}{R_P} + j\omega C} \right) \\
&= R_S + \frac{R_P}{1+(R_P\omega C)^2} - j \frac{R_P^2\omega C}{1+(R_P\omega C)^2}
\end{aligned} \tag{2.8}$$

However, in the real case, a coating is not always uniformly deposited. Defects such as scratches or pores on the coating surface become conductive when immersed in an aqueous environment, and allow chemicals to get access to the underlying substrate. Also, the surface of the bulk CoCrMo alloy is initially covered by a thin “coating”, the air-formed Cr₂O₃ oxide film. In such cases, the ideal capacitor is impossibly fitted to the circuit model. A constant phase element (CPE) is therefore introduced to replace the ideal capacitor, as shown in Figure 2-12.

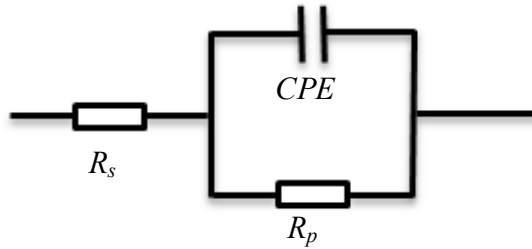


Figure 2-12: The Randles circuit model used to represent the electrochemical system of a non-ideal coated metal or a bulk metal in solution [90].

The impedance associated with a CPE is also a complex function as the capacitor and is given by the equation as follows [90]:

$$Z_{CPE} = \frac{1}{Y_0(j\omega)^\alpha} \tag{2.9}$$

As a result,

$$Y_0 = \frac{1}{Z_{CPE}(j\omega)^\alpha}, \tag{2.10}$$

where Y_0 is the constant CPE parameter in unit of $\Omega^{-1}s^\alpha$ (s in second) and α is the CPE exponent lying between 0 and 1. When α is equal to 1, the CPE is equivalent to an ideal capacitor $Y_0 = C$.

For the CPE circuit model, the circuit analysis result in the expression for total, real, and imaginary impedance, the modulus of impedance $|Z|$, as well as the phase angle θ are given as,

$$Z(\omega) = R_S + \frac{R_P}{1+(R_P\omega Y_0)^2} - j \frac{R_P^2\omega Y_0}{1+(R_P\omega Y_0)^2} \quad (2.11)$$

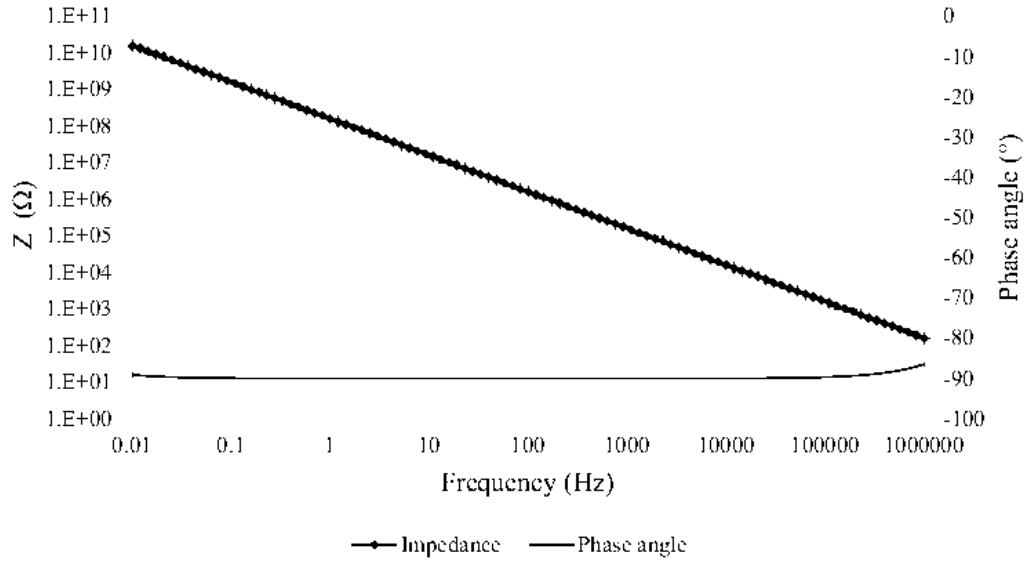
$$Z_{real}(\omega) = R_S + \frac{R_P}{1+(R_P\omega Y_0)^2} \quad (2.12)$$

$$Z_{imaginary}(\omega) = -\frac{R_P^2\omega Y_0}{1+(R_P\omega Y_0)^2} \quad (2.13)$$

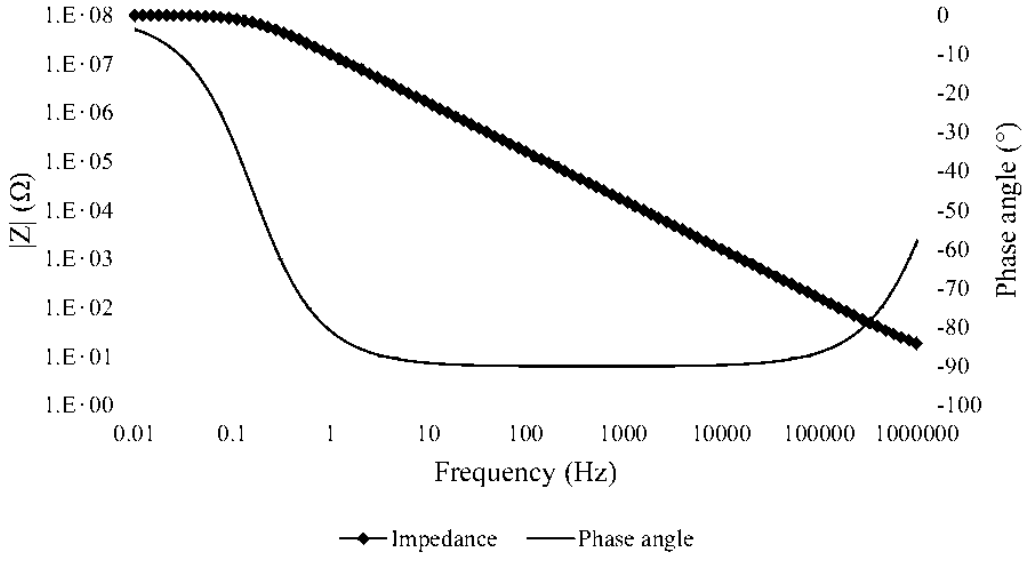
$$\theta = \tan^{-1}\left(\frac{Z_{imaginary}}{Z_{real}}\right) \quad (2.14)$$

$$|Z| = ((Z_{real})^2 + (Z_{imaginary})^2)^{1/2} \quad (2.15)$$

To characterize the impedance, the magnitude (or the modulus) of the impedance $|Z|$, the phase angle θ and the frequency, are often plotted as what is known as a Bode plot [87], as shown in Figure 2-13. By fitting measured data to the CPE Randles circuit, values such as R_S , R_P , Y_0 , and α can be calculated.



(a)



(b)

Figure 2-13: Typical Bode plots: (a) for an ideal coating, and (b) for a non-ideal coating circuit [91].

As the CPE is frequency dependent, the impedance of the CPE decreases when the frequency increases. When the frequency reaches a very high value, the impedance of the CPE can be very small and the total impedance is therefore controlled by R_S . From Figure 2-13(b), it can be seen that, at very high frequencies,

$$Z(\omega) = R_S \quad (2.16)$$

As the frequency decreases, the total impedance increases due to the increase of the CPE impedance. When the frequency approaches to a very low value, the impedance of the CPE becomes ultimately high and the CPE will act as an open circuit. As a result, it can also be seen from Figure 2-13(b) that, at very low frequencies,

$$Z(\omega) = R_S + R_P \quad (2.17)$$

Thus, in both the high and low frequency regions, the Randles circuit behaves primarily as a resistor. The impedance does not vary along with the frequency. At intermediate frequencies, the capacitor's impedance is important and the cell acts like a capacitor. The imaginary component becomes significant, the phase angle approaches -90° and the cell impedance becomes linearly frequency dependent.

2.5.2.4 Immersion test

Immersion test remains to be one of the most efficient approaches for evaluating the corrosion resistance of metals in aqueous solution. In this method, specimens are immersed into the corrosive solution that simulates real work circumstances as much as possible, or into strong corrosive media to accelerate corrosion process in order to collect corrosion data or to compare different materials in one discipline. A number of factors have effects on achieving specific purpose such as pH value, test temperature, immersion solution, and duration of immersion time [84]. The experimental data from immersion test can be assessed in various ways, such as weight change (loss or gain), volume change (loss or gain), pits depth, and so on. From the micro-morphology standpoint, the

immersion-tested specimen can also be examined and analyzed using SEM, EDX, X-Ray Diffraction (XRD), and X-Ray Photoelectron Spectroscopy (XPS). The last two enable the investigation of chemical element transformation.

After immersion, the inductively couple plasma optical emission spectrometry (ICP-OES) analytical technique can be used to detect the released ion concentrations within the solution. The ICP-OES is a type of emission spectroscopy that utilizes the inductively coupled plasma to excite atoms and ions that emit electromagnetic radiation at different wavelength characteristics of particular elements [92].

3 Chapter: Microstructure Characterization

The microstructure of a material determines its properties and performances in service. Therefore, the microstructures of the alloys being studied in this research were analyzed prior to the investigation of their wear and corrosion resistance.

3.1 Alloy specimens

3.1.1 Chemical composition

Four different Stellite alloys were studied in this research, including high-carbon Stellite 720, modified low-carbon Stellite 21 with increased Cr content, nitrided Stellite 21 with addition of CrN, and conventional Stellite 21 as reference. These alloy specimens were all produced at Kennametal Stellite Inc. Stellite 21 and Stellite 720 specimens were cast products while the other two were processed by hot isostatic pressing (HIP), as the modified Stellite 21 and nitrided Stellite 21 alloys were easier to be made with the addition of Cr and CrN powders using the HIP approach. About 10 wt%Cr and 0.4 ~ 0.6 wt%CrN powders were added to Stellite 21 powder respectively, to create the two new alloys - modified Stellite 21 and nitrided Stellite 21. The chemical compositions of Stellite 21 and Stellite 720 are given in Table 3-1. Stellite 720 contains very high C content whereas Stellite 21 has very low C content. Therefore, the former is a carbide-strengthened alloy and the latter is a solution-strengthened alloy. The contents of Cr and Mo of Stellite 720 are also higher than those of Stellite 21, which further strengthen this alloy.

Table 3-1: Chemical compositions (wt%, Co in balance) of Stellite 21 and Stellite 720.

Elements Alloys	Cr	Mo	C	Fe	Ni	Si	Mn	Other
Stellite 21	27	5.5	0.25	3	2.75	1	1	
Stellite 720	33	18	2.5	3	3	1.5	1.5	0.3B

3.1.2 Specimen preparation

The preparation procedures of the specimens for microstructural analysis include cutting, mounting, rough grinding, intermediate polishing and final polishing. The alloy specimens were cut in dimensions of approximately 15 × 10 × 2 mm. After cleaned with water, the specimens were mounted by encapsulating into epoxy resin. The mounted specimens were ground by using different sizes of silicon carbide (SiC) abrasive paper #240, #320, #400, and #600 successively, followed by polishing processes using polishing cloths plus 6 um and 0.3 um alumina powders. The specimens were cleaned up by water during each step of grinding and polishing to avoid debris sustaining. After polishing, the specimens were blow-dried by an air gun. Smooth and specular surfaces were obtained finally for microstructural analysis.

3.2 Microstructural analysis

3.2.1 Test facilities

The microstructure analysis of the specimens was performed on a Tescan Vega-II XMU SEM, shown in Figure 3-1, equipped with an Oxford EDX spectroscopy system for elemental analysis and quantitative mapping. The images of the microstructures were

captured at a low magnification and at a high magnification, respectively. Each phase in the microstructures was analyzed with the EDX system that can provide the chemical constituents in a specific area. The EDX spectrum for the chemical constituents can then be obtained, along with the elemental content table. However, it should be mentioned that the SEM system is not able to accurately identify the non-metallic elements such as carbon element. For this reason, the carbon contents in the microstructural phases are not presented in the elemental content tables. The percentages of other element contents were recalculated using the following formula:

$$\frac{100\%}{Total_{Original}(\%) - Carbon\ constant(\%)} = \frac{Element\ content\ After(\%)}{Element\ content\ Before(\%)} \quad (3.1)$$

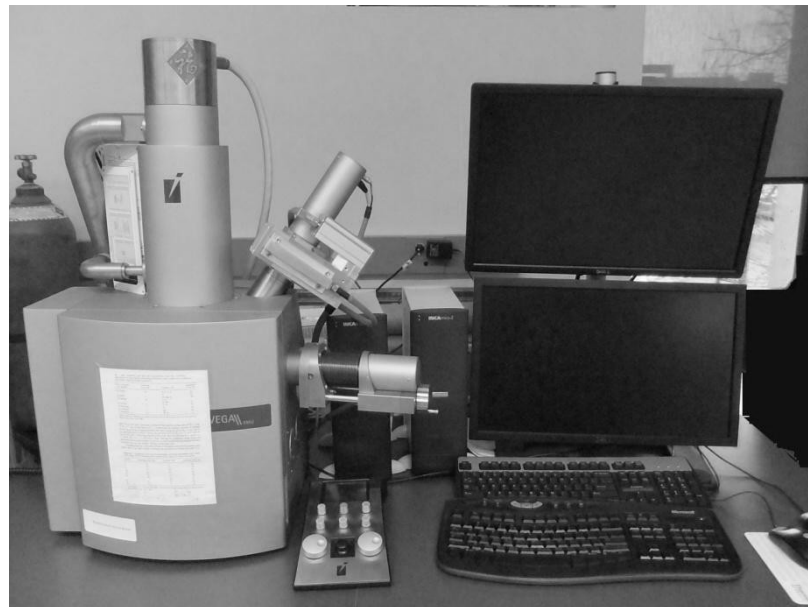
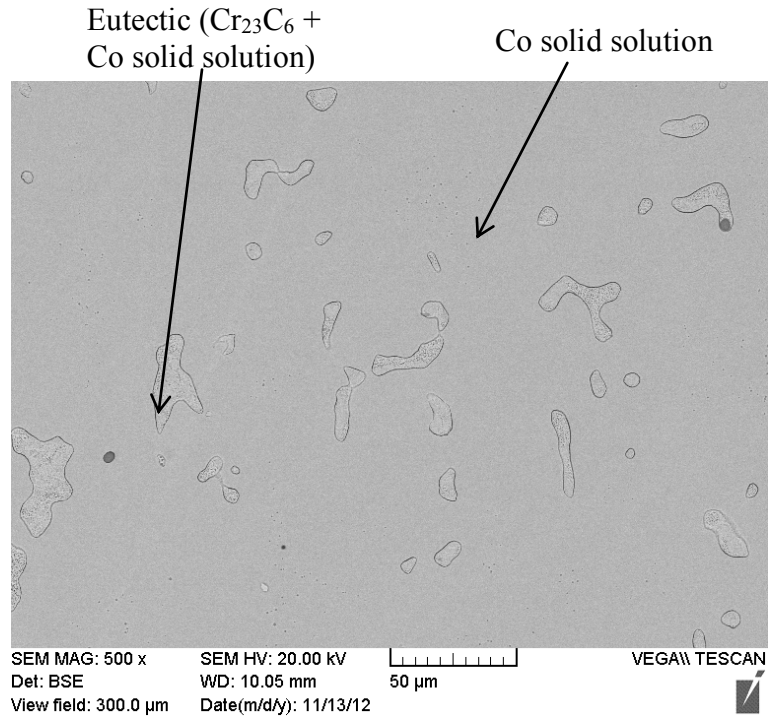


Figure 3-1: Tescan Vega-II XMU Scanning Electron Microscope (SEM) with an Energy Dispersive X-ray (EDX) spectroscopy system.

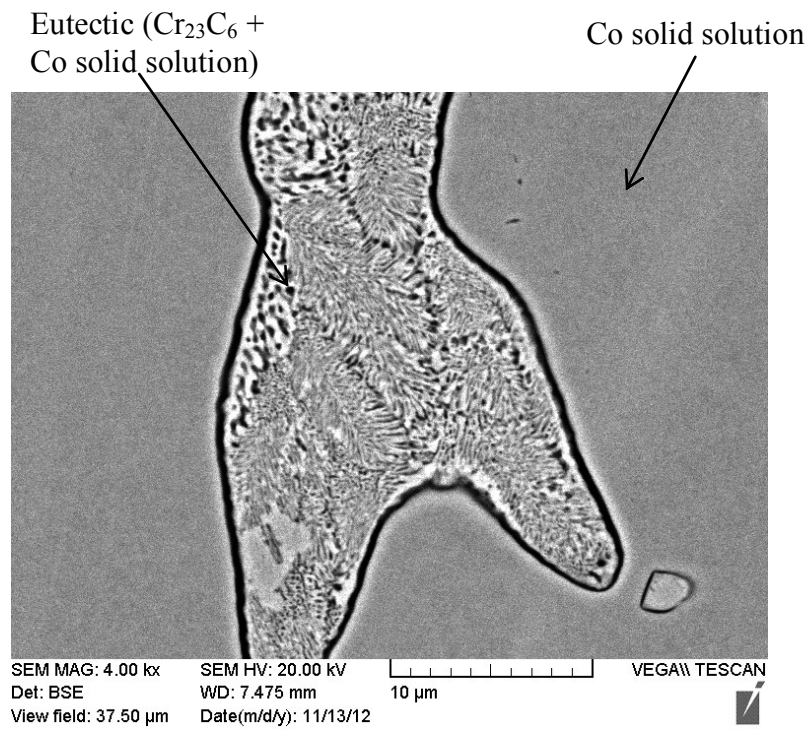
3.2.2 Microstructure and phases

Stellite 21

The SEM images of microstructure of Stellite 21 are presented in Figure 3-2, which show that the microstructure of this alloy consists of primary Co solid solution with minor carbides precipitated in the eutectic phase. Since Stellite 21 contains a very low level of C (0.25 wt %), the volume fraction of carbides in this alloy is only about 4% [57]. This renders it a solution-strengthened alloy rather than a carbide-strengthened alloy. Furthermore, the EDX results for the solid solution phase and the fishbone eutectic phase (carbides and Co solid solution mixture) are presented in Figure 3-3. It is shown that the solid solution contains very high Co content and also some Cr and Mo while the eutectic phase has high C and very high Cr. Therefore, the carbide is identified to be Cr_{23}C_6 instead of Cr_7C_3 . It has been reported that Cr_{23}C_6 is commonly abundant in low-carbon Stellite alloys [57]. There is also high Co content in the eutectic phase which comes from the Co solid solution.

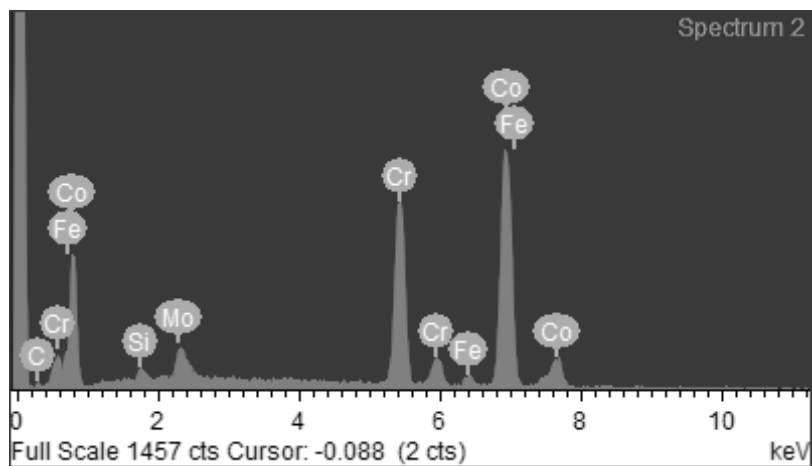
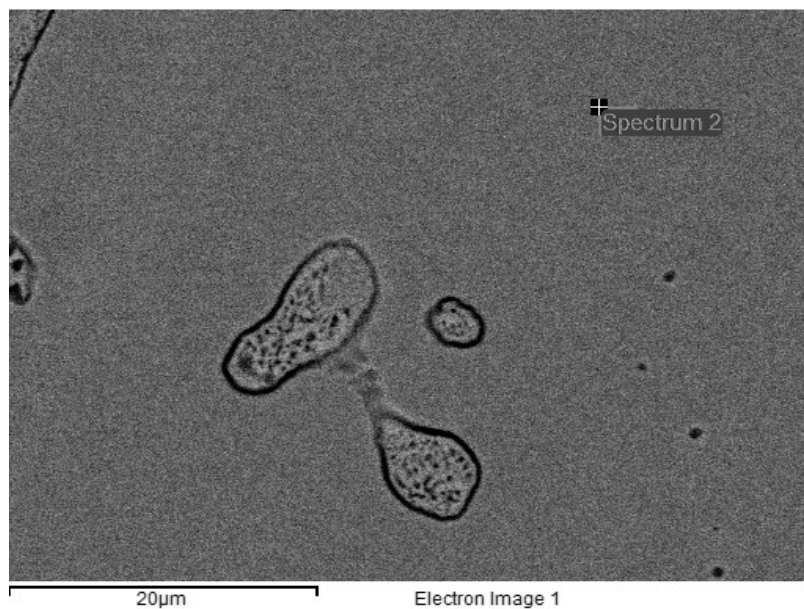


(a)



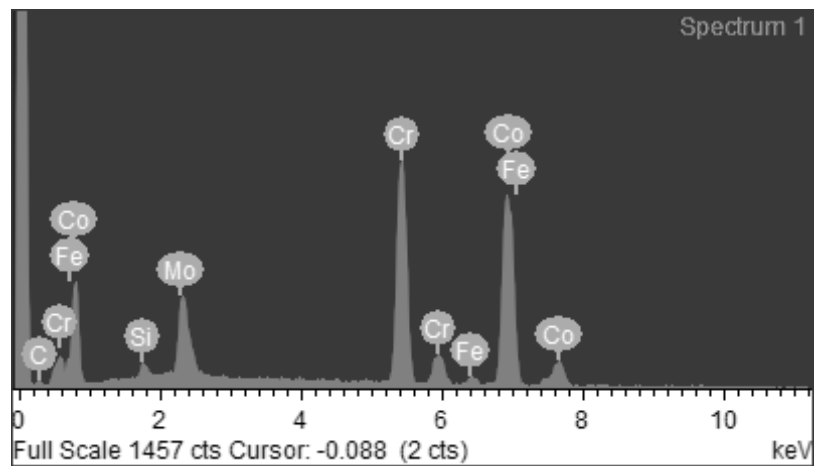
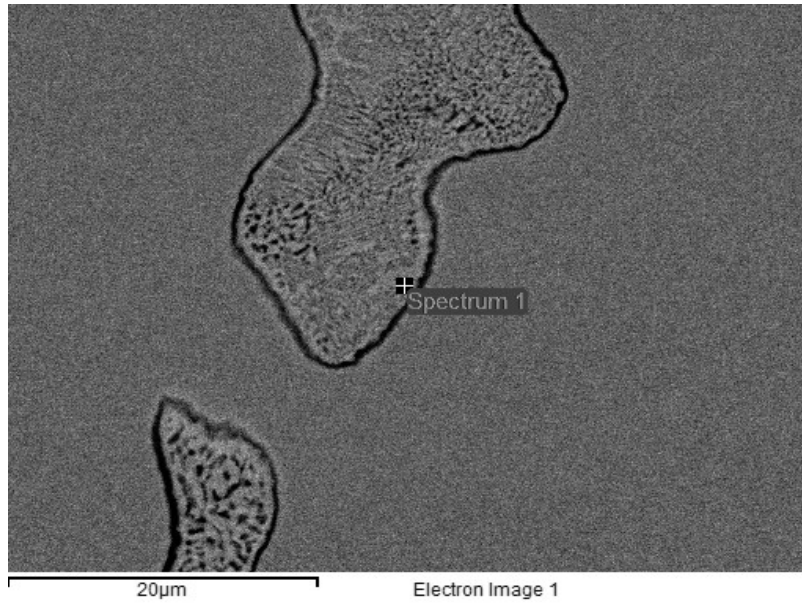
(b)

Figure 3-2: SEM microstructure of Stellite 21: (a) at low magnification, and (b) at high magnification.



Element	Weight%	Atomic%
Si K	0.79	1.62
Cr K	27.69	30.8
Fe K	2.08	2.13
Co K	64.17	62.51
Mo L	5.27	3.15
Totals	100	100

(a)



Element	Weight%	Atomic%
Si K	0.79	1.71
Cr K	32.97	37.32
Fe K	1.72	1.80
Co K	50.86	50.80
Mo L	13.16	8.37
Totals	100	100

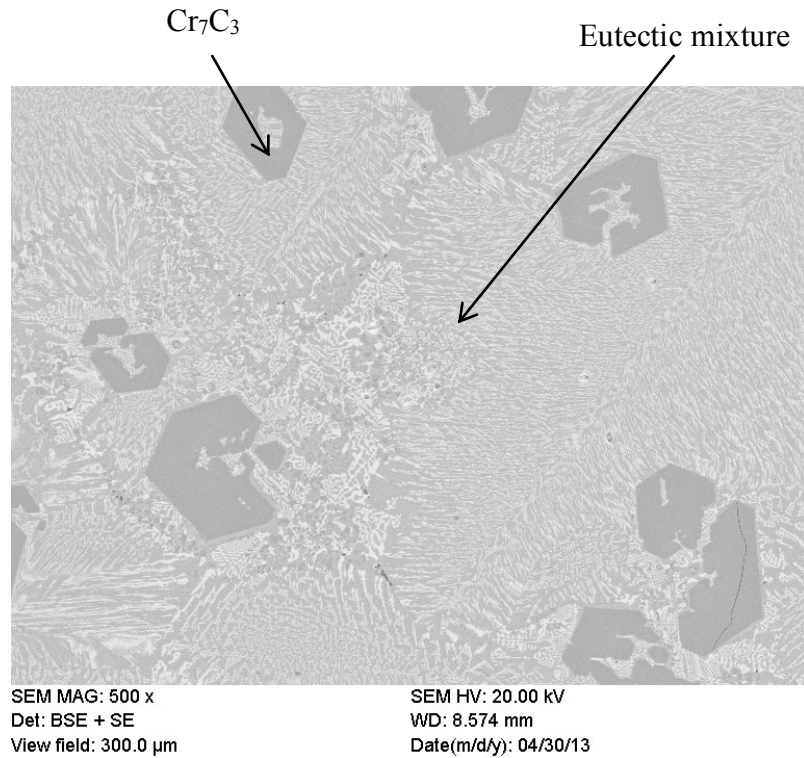
(b)

Figure 3-3: EDX results of Stellite 21: (a) cobalt solid solution, and (b) eutectic (Cr_{23}C_6 carbide and Co solid solution).

Stellite 720

Stellite 720 contains a very high level of carbon content (2.5 wt%) so that it has a hyper-eutectic microstructure, consisting of primary carbide (black) and eutectic mixture that includes Co solid solution (grey) and various carbides (black and white), as shown in Figure 3-4. To further identify the phases present in this alloy, the EDX analysis was conducted on each phase of the microstructure. The EDX spectra along with the element content tables are given in Figure 3-5. For the Co solid solution phase, similar to that of Stellite 21, Co and Cr predominate in the composition, but the Co content in the solid solution of Stellite 720 is lower than that of Stellite 21. This is because some Co in the former is imparted to form the Mo-rich Co-containing carbide. Due to the high content, Mo not only exists in the solid solution as one of the strengtheners but also forms Mo-rich carbide (white) in this alloy. As shown in Figure 3-5(b), high Mo, Co as well as C

contents are detected in the white phase, which is probably $(\text{Mo}, \text{Co})_6\text{C}$ or $(\text{Mo}, \text{Co})_2\text{C}$ carbide. In the primary carbide phase, very high Cr is identified and a high peak (representing a large amount) of C is shown in the EDX spectrum. This is the type of Cr_7C_3 carbide, which is commonly formed in high-carbon Stellite alloys [57].



(a)

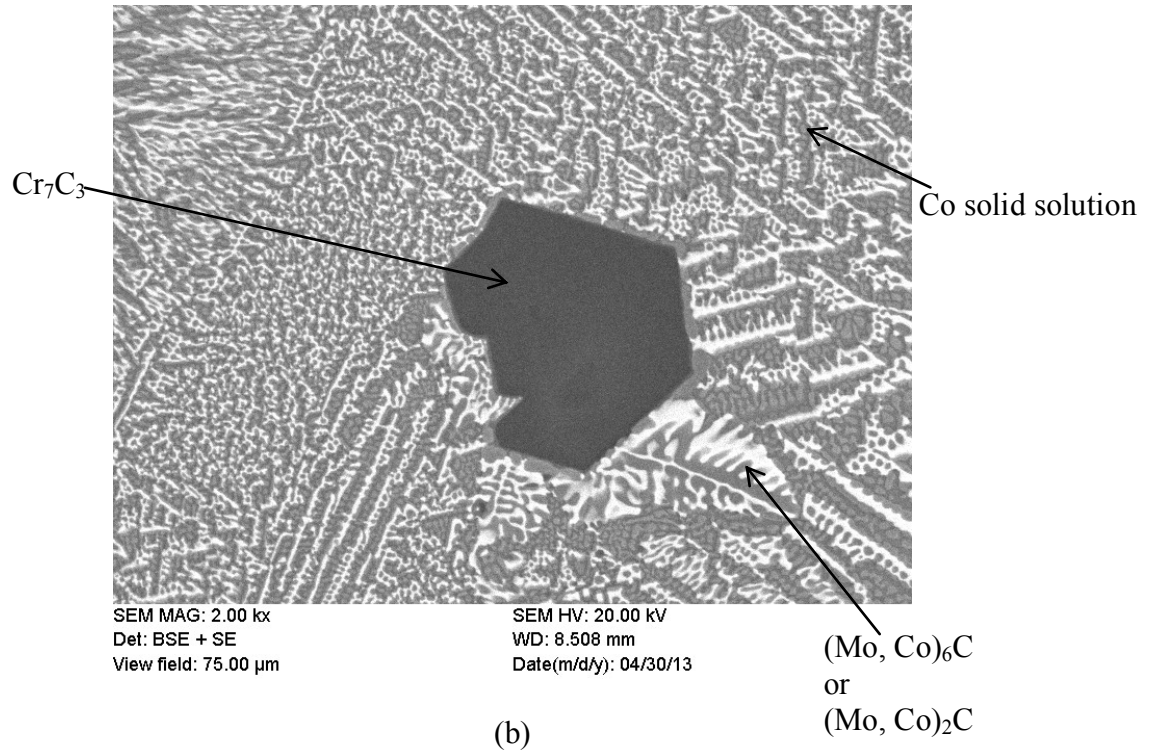
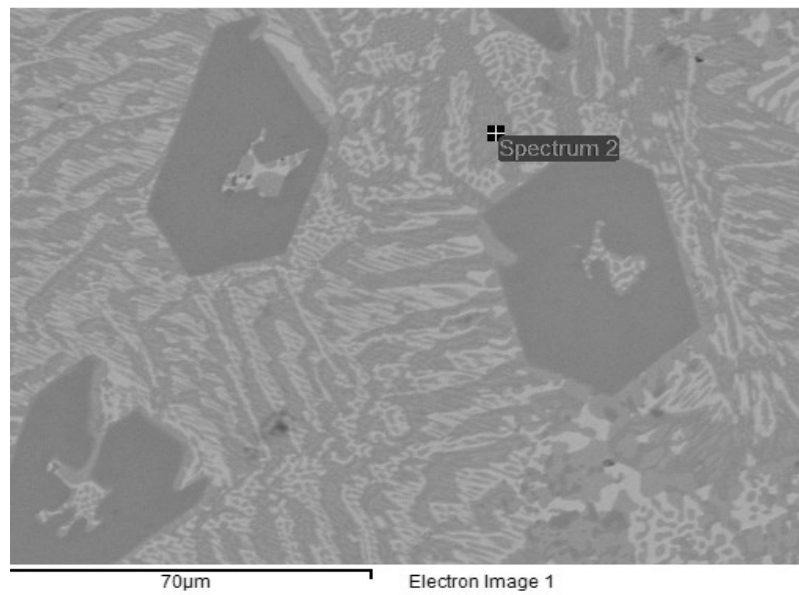
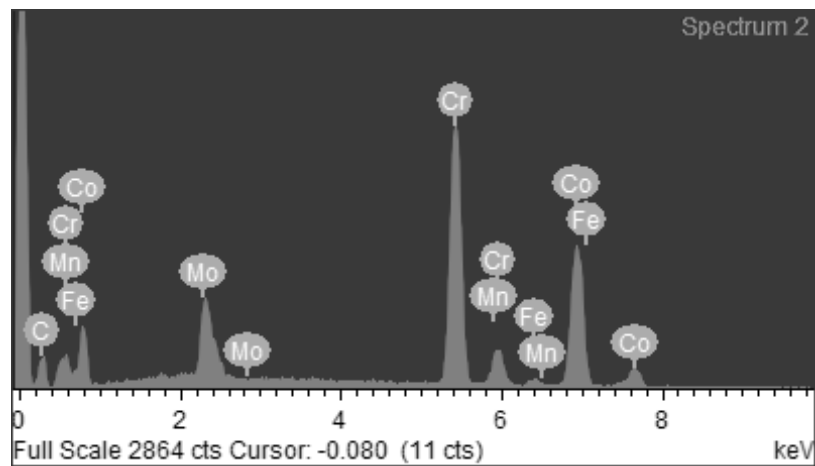


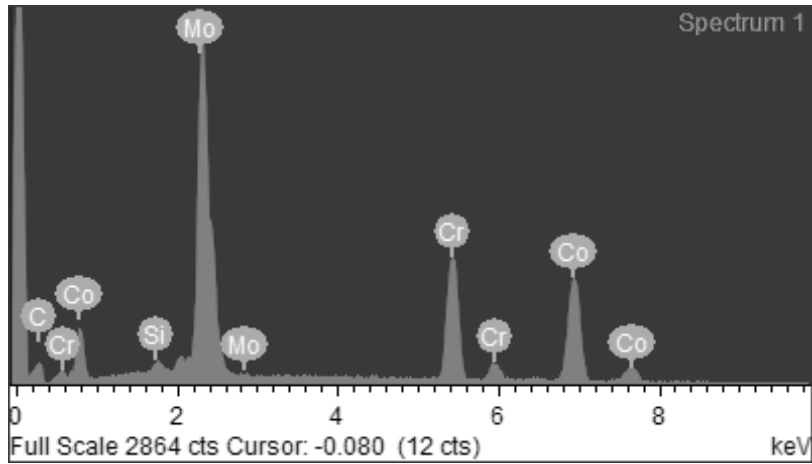
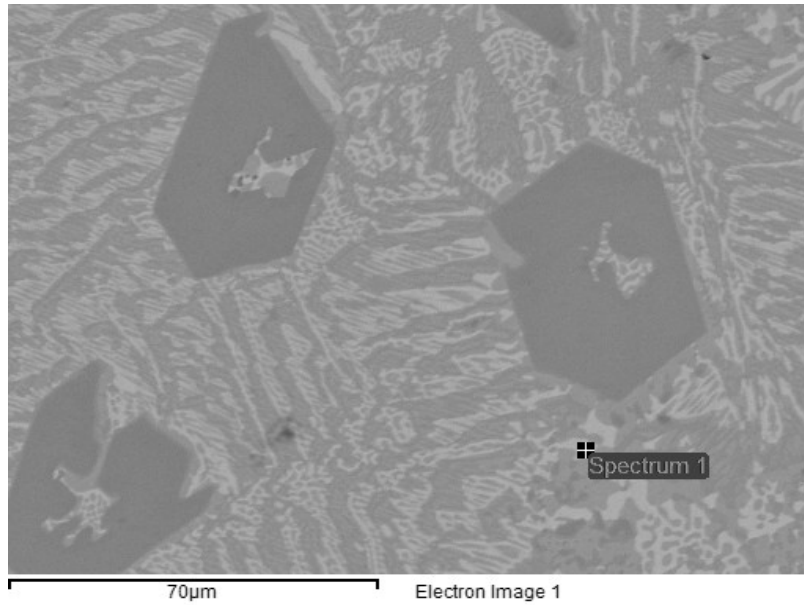
Figure 3-4: SEM microstructure of Stellite 720: (a) at low magnification, and (b) at high magnification.





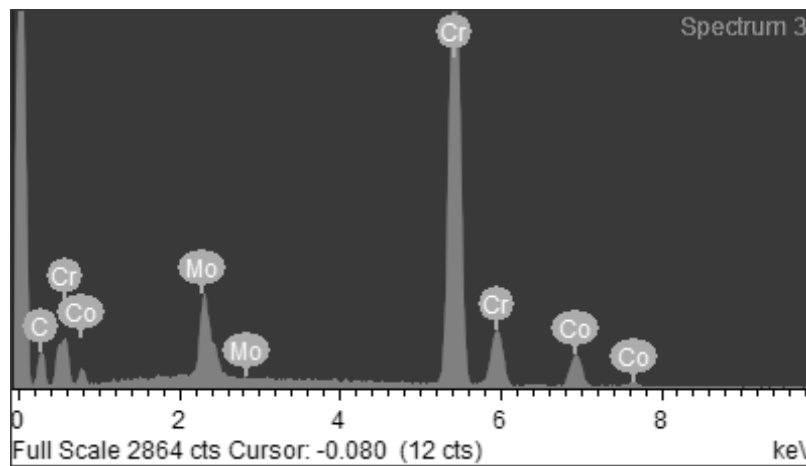
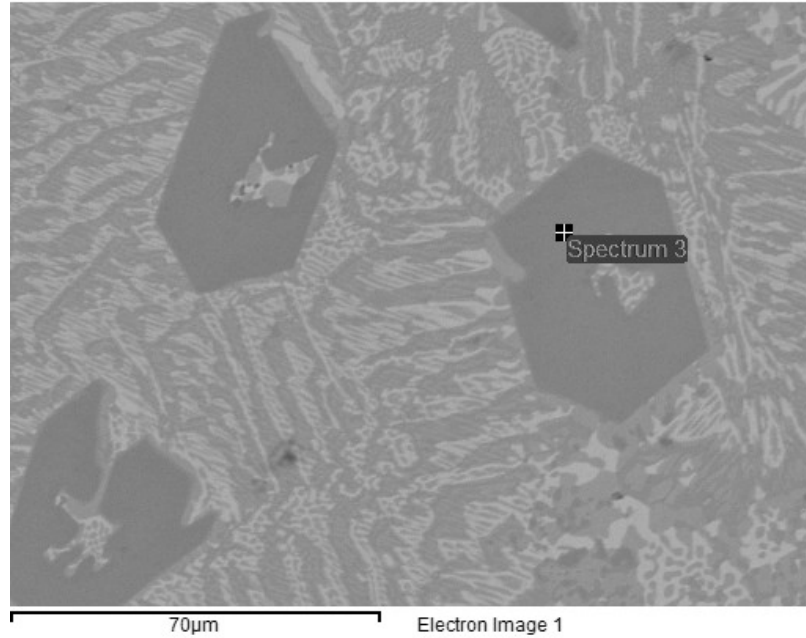
Element	Weight%	Atomic%
Cr K	41.83	37.32
Mn K	1.04	1.11
Fe K	1.52	1.59
Co K	42.44	42.16
Mo L	13.17	8.04
Totals	100	100

(a)



Element	Weight%	Atomic%
Si K	0.58	1.43
Cr K	20.80	27.89
Co K	29.76	35.19
Mo L	48.86	35.49
Totals	100	100

(b)



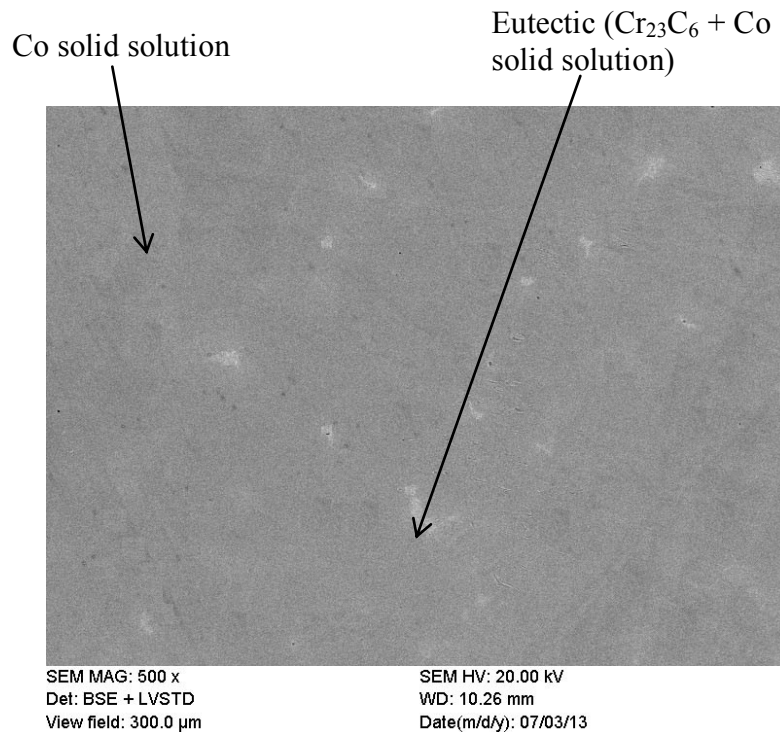
Element	Weight%	Atomic%
Cr K	76.40	82.38
Co K	10.56	10.01
Mo L	13.04	7.61
Totals	100	100

(c)

Figure 3-5: EDX results of Stellite 720: (a) Co solid solution, (b) Mo-rich carbide, and (c) primary Cr_7C_3 carbide.

Modified Stellite 21

The SEM images of microstructure and EDX spectra along with elemental content tables for modified Stellite 21 are presented in Figure 3-6 and Figure 3-7. As shown in Figure 3-6(a), similar to Stellite 21, the microstructure of modified Stellite 21 also contains the primary Co solid solution phase and the eutectic phase (Cr_{23}C_6 carbide + Co solid solution). Differently, the eutectic phase of modified Stellite 21 is finer and the carbide size is much smaller when compared to that of the carbides in Stellite 21. The amount of carbides is also reduced. These can be attributed to the HIP process. The EDX results in Figure 3-7 confirm that the Cr content in the solid solution of modified Stellite 21 is much higher than that in the solid solution of Stellite 21. This is owing to the addition of 10 wt%Cr in the former.



(a)

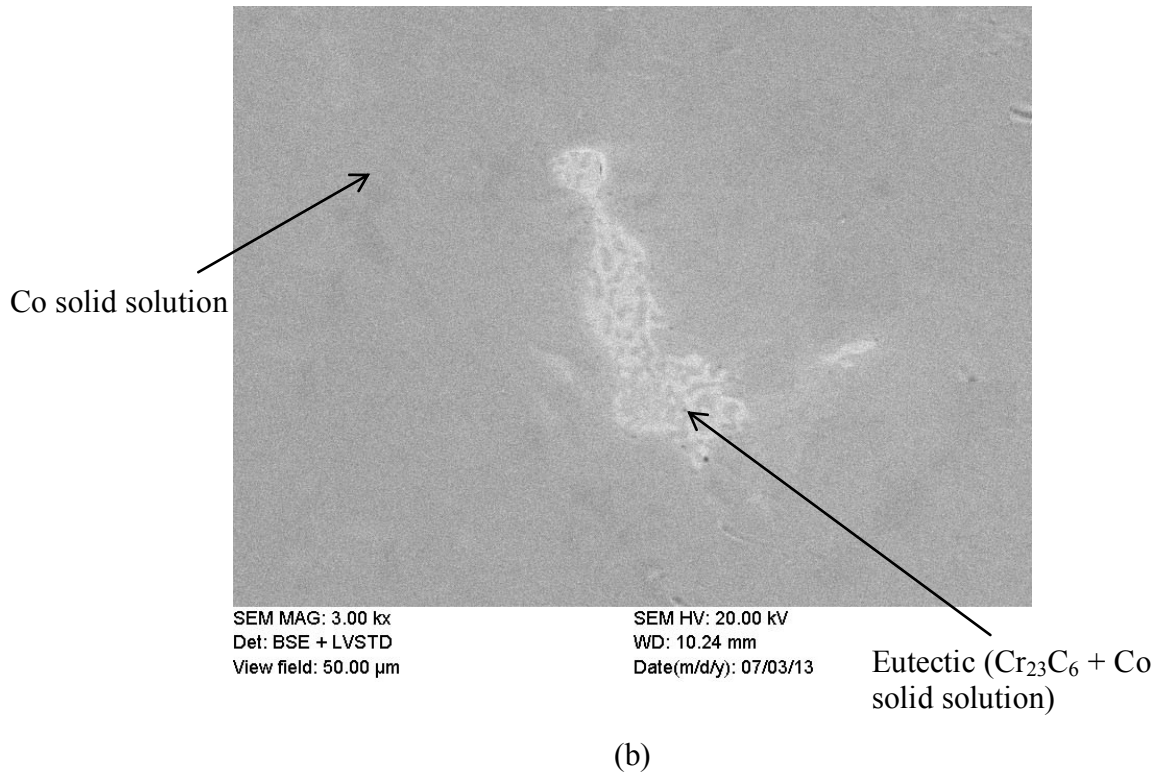
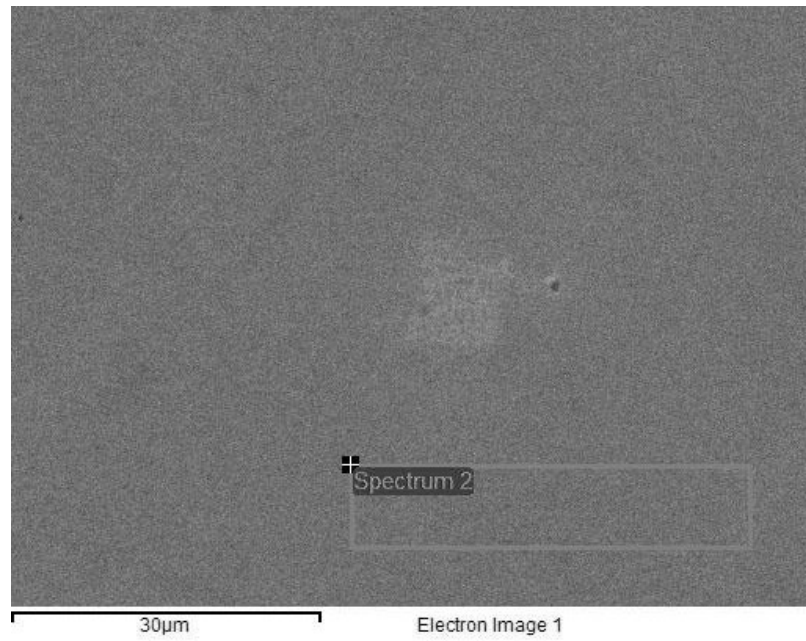
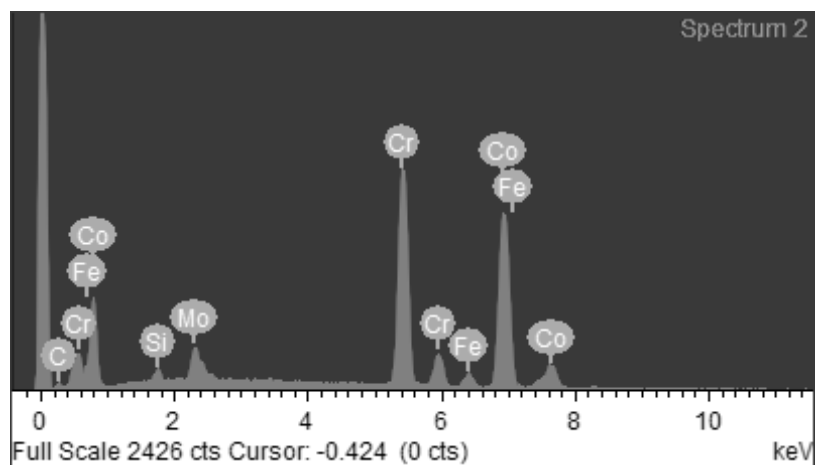


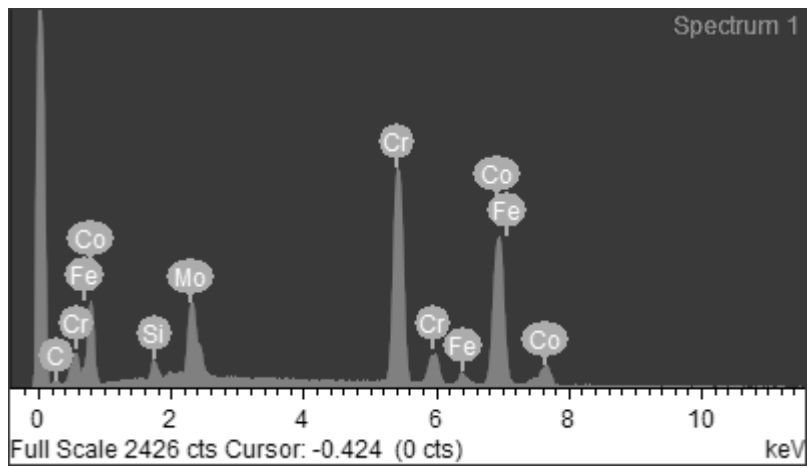
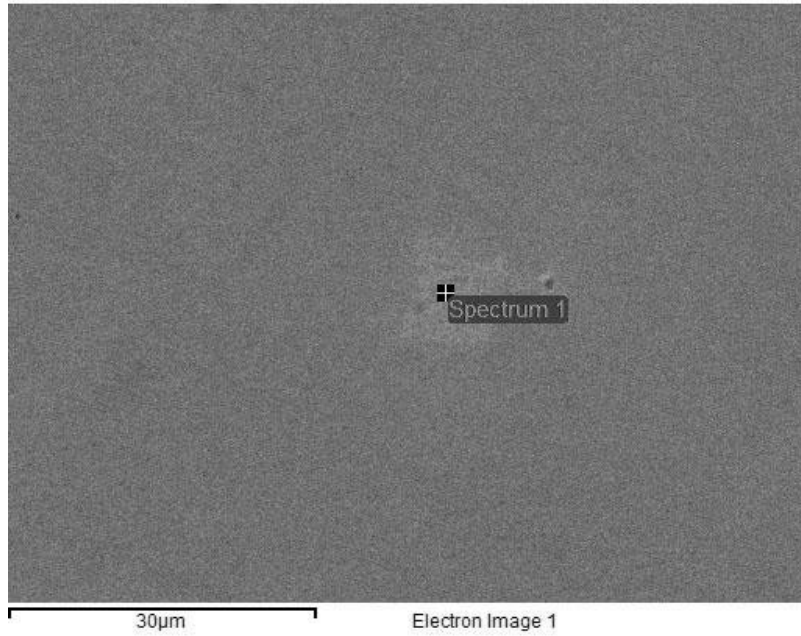
Figure 3-6: SEM microstructure of modified Stellite 21: (a) at low magnification, and (b) at high magnification.





Element	Weight%	Atomic%
Si K	0.88	1.75
Cr K	36.38	39.73
Fe K	3	3.05
Co K	54.12	52.14
Mo L	5.62	3.33
Totals	100	100

(a)



Element	Weight%	Atomic%
Si K	1.31	2.71
Cr K	36.79	41.18
Fe K	2.39	2.49
Co K	45.98	45.41
Mo L	13.53	8.21
Totals	100	100

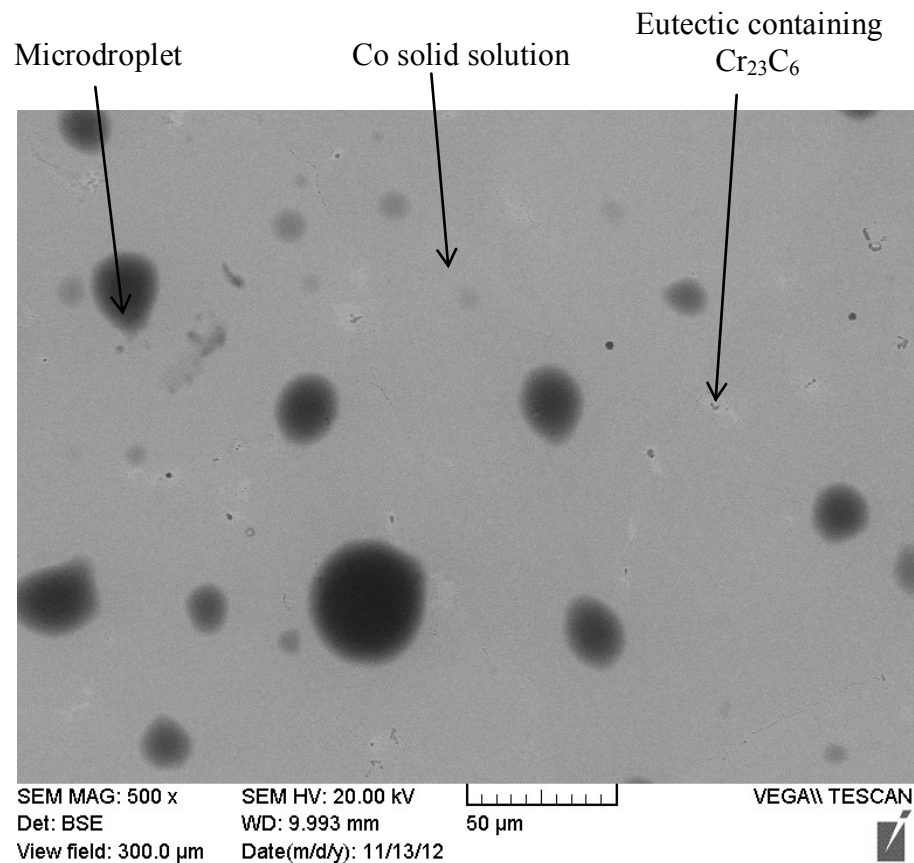
(b)

Figure 3-7: EDX results of modified Stellite 21: (a) Co solid solution, and (b) eutectic (Cr_{23}C_6 carbide + Co solid solution).

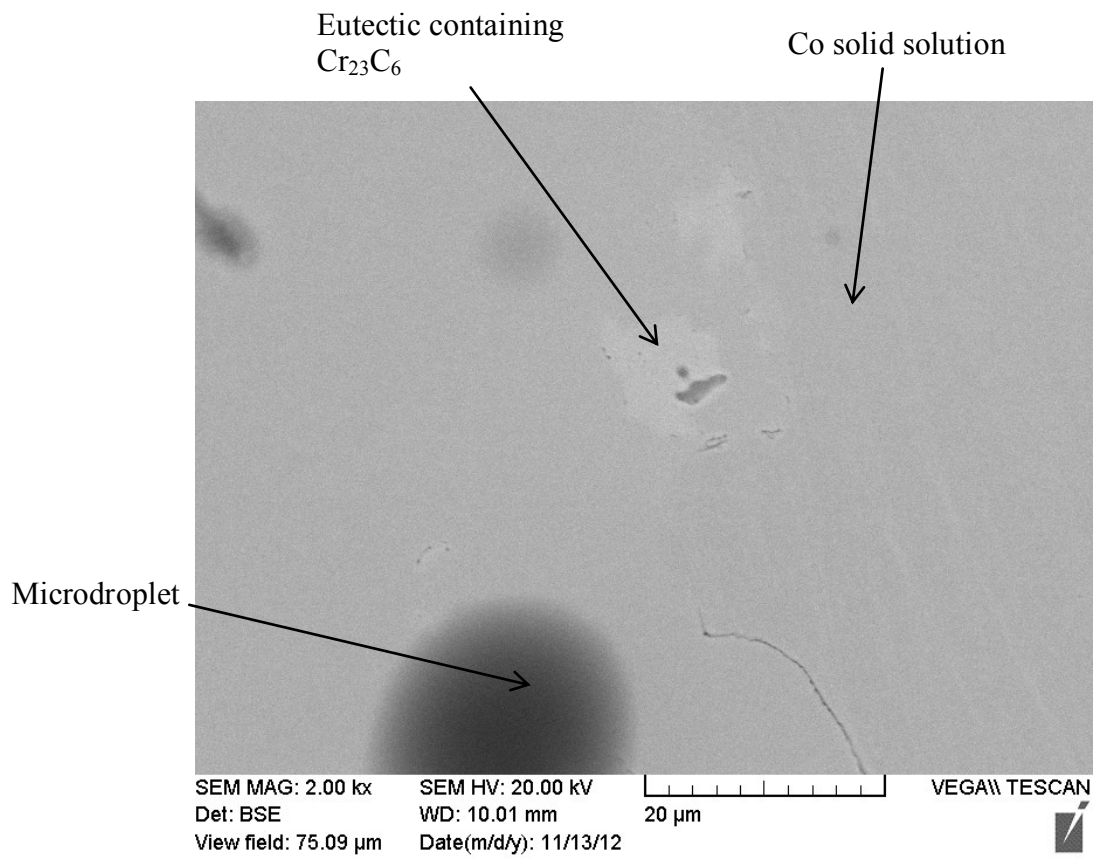
Nitrided Stellite 21

The SEM images of microstructure and EDX spectra along with elemental content tables of nitrided Stellite 21 are presented in Figure 3-8 and Figure 3-9. With addition of minor CrN powder in Stellite 21, the microstructure has an obvious change, as shown in Figure 3-8, lots of microdroplets (black spots) are found in the microstructure. Also, similar to modified Stellite 21, the HIP process made the eutectic phase of nitrided Stellite 21 finer, the carbide size smaller and the carbide amount less, compared with the cast Stellite 21. The EDX analysis on this alloys shows that the solid solution has almost the same elemental contents as that of Stellite 21, but the Cr content in nitrided Stellite 21 is slightly higher, see Figure 3-8(a). This may be due to the reduction of Cr_{23}C_6 carbide amount in nitrided Stellite 21, which resulted in more Cr remaining in the solid solution. The elemental contents of the eutectics of Stellite 21 and nitrided Stellite 21 are very

similar, comparing the EDX results in Figure 3-3(b) and Figure 3-9(b), which means that the carbide did not change and remained to be Cr_{23}C_6 after Stellite 21 was nitrided. The microdroplets are identified to have a similar chemical composition to the solid solution, as shown in Figure 3-9(c), but the O and C elements are abundant in the microdroplets, which imply that the microdroplets are porous and C-rich. No nitrogen was detected by the EDX analysis in this alloy although CrN powder was added. This is due to the small amount of CrN added, only 0.4 ~ 0.6 wt%, and the EDX facility is unable to detect such low content, but CrN and new nitrides, for example, Mo-rich nitride may exist in the microdroplets.

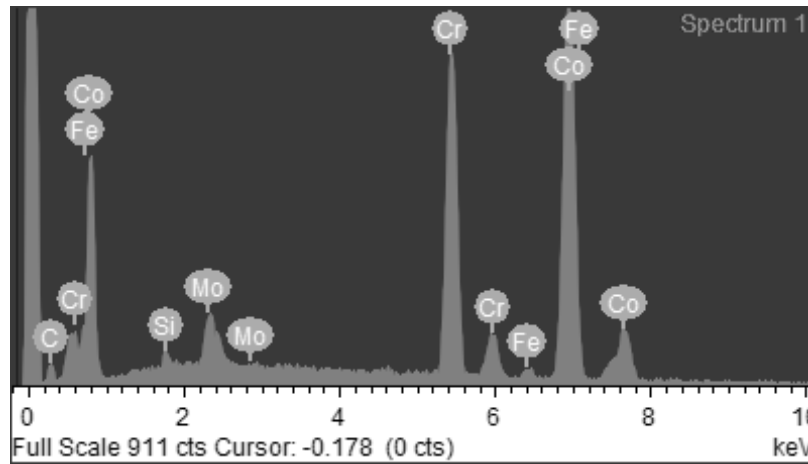
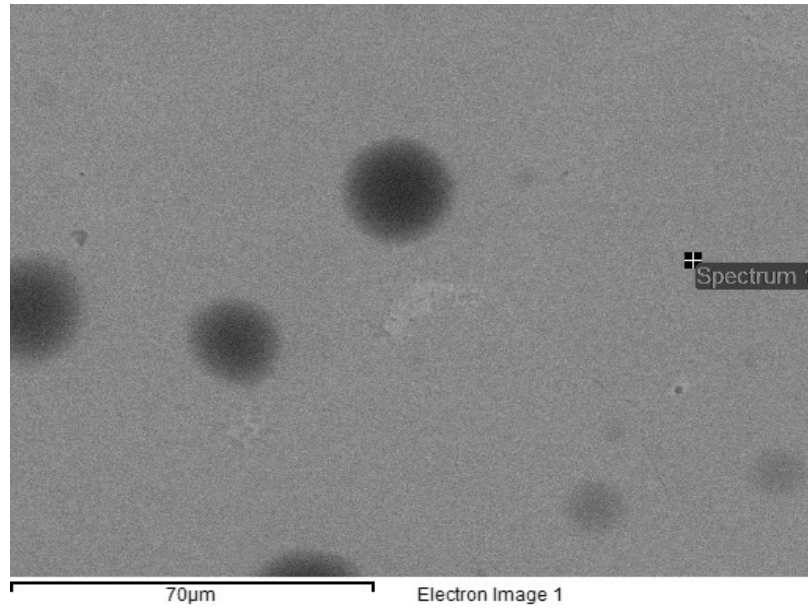


(a)



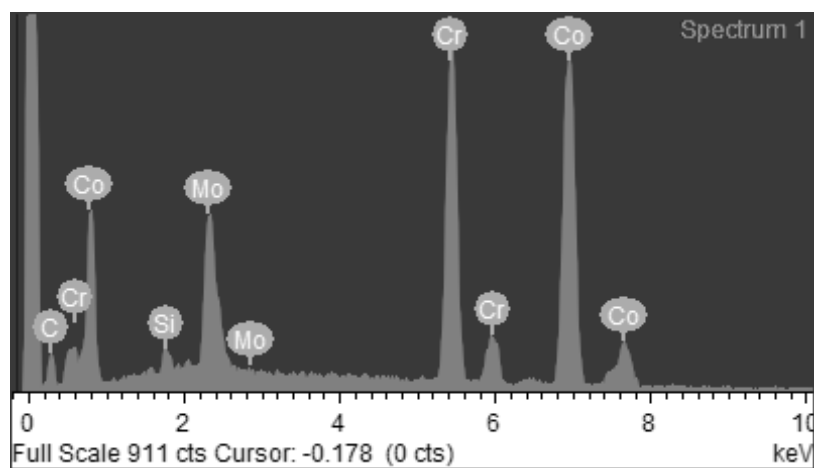
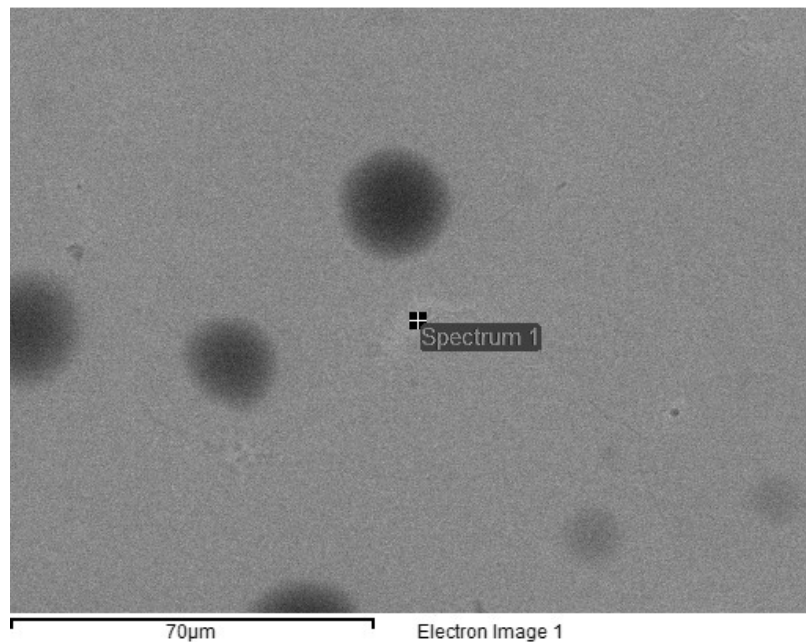
(b)

Figure 3-8: SEM microstructure of nitrided Stellite 21: (a) at low magnification, and (b) at high magnification.



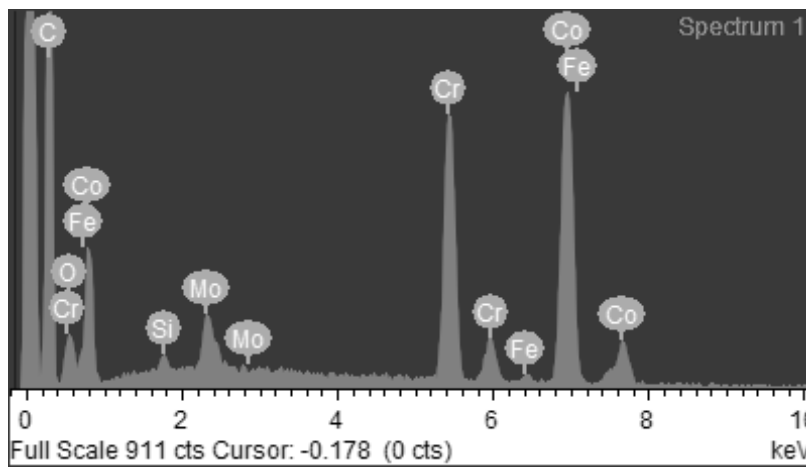
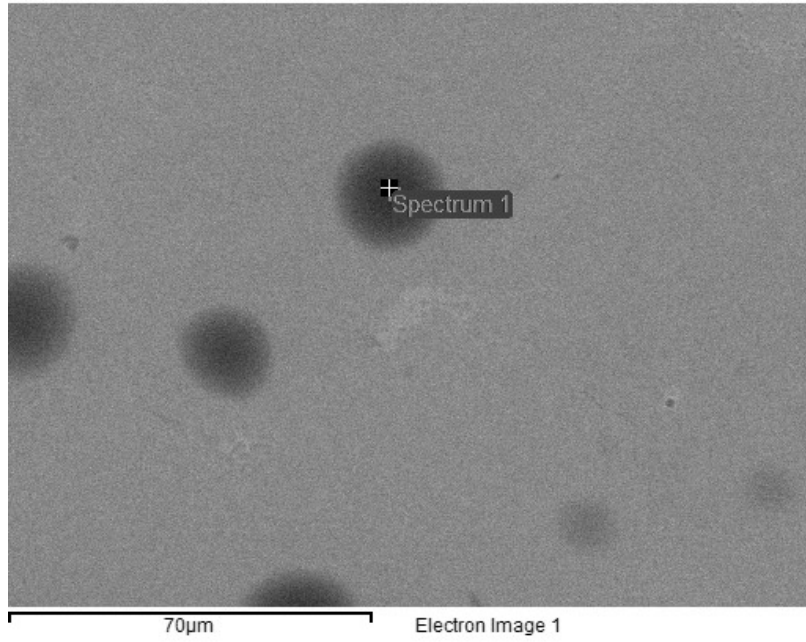
Element	Weight%	Atomic%
Si K	0.65	1.33
Cr K	28.41	31.37
Fe K	1.29	1.34
Co K	64.63	62.95
Mo L	5.02	3.01
Totals	100	100

(a)



Element	Weight%	Atomic%
Si K	1.08	2.30
Cr K	30.07	34.22
Co K	54.32	54.52
Mo L	14.53	8.96
Totals	100	100

(b)



Element	Weight%	Atomic%
O K	4.77	15.16
Si K	0.63	1.18
Cr K	29.37	28.79
Fe K	1.14	1.05
Co K	59.34	51.32
Mo L	4.75	2.50
Totals	100	100

(c)

Figure 3-9: EDX results of nitrided Stellite 21: (a) Co solid solution, (b) eutectic with Cr_{23}C_6 carbide, and (c) microdroplet.

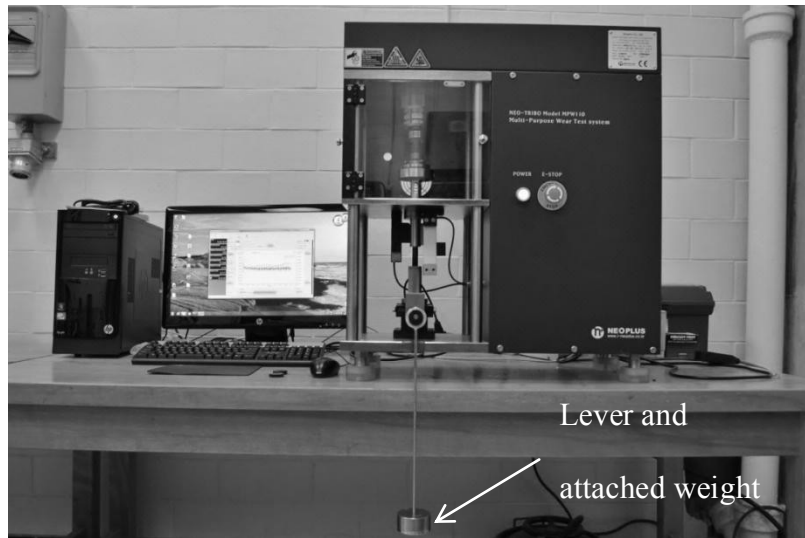
4 Chapter: Wear Resistance Evaluation

The objective of this research was to explore new materials that can improve the MOM bearing of hip implants. Therefore, for the proposed Stellite alloys, wear resistance is one of the major considerations in this research.

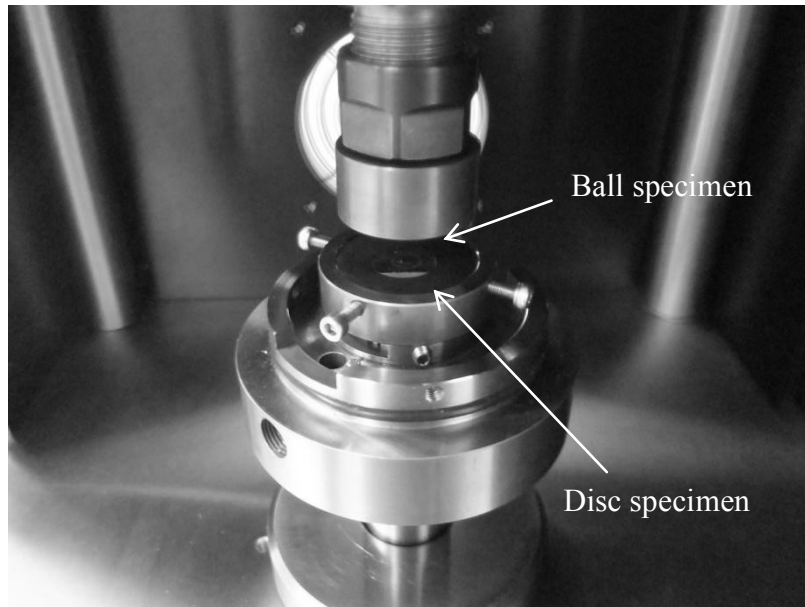
4.1 Wear test

4.1.1 Test equipment

As the experimental limitation, the specimens were not able to be tested with a hip simulator. Therefore, the size and shape of the wear particles were not concluded in this research. The wear behavior of the specimens was characterized by the volumetric wear loss. The wear test on the alloys under study was conducted using a pin-on-disc tribometer (Neoplus Ltd.), shown in Figure 4-1, according to the testing procedure outlined in ASTM Designation G 99 – 95a (2000) [93]. The system consists of a rotating pin that is pressed perpendicularly against a static disc under a constant normal force. This load can be adjusted by a 2-stage lever and attached weights. The pin is a ball having a radius of 2.5 mm and is made of 94% WC and 6% Co with the hardness of HV 1534, while the disc is the tested specimen that is mounted to the base holder. A software controlled system is configured to record the sliding distance, friction force as well as friction coefficient in real time.



(a)



(b)

Figure 4-1: Neoplus pin-on-disc tribometer system: (a) system assembly, and (b) rotating ball pin and static disc specimen.

4.1.2 Test parameters

The specimens had a dimension of approximately $10 \times 10 \times 2$ mm and were mounted by encapsulating into epoxy resin with a thickness of 10 mm. To achieve a flat and smooth surface, each specimen was ground using silicon carbide (SiC) abrasive papers from #240 to #600. The specimens were cleaned by water and dried by compressed air to ensure that no debris was left on the surfaces after polishing. The test parameters used in this research are summarized in Table 4-1. The test was conducted at room temperature and in dry-lubricating condition. A normal force (F) of 5 N was applied against the ball and the disc. The pin (ball) was placed at a distance of 3 mm away from the rotation center with a rotation speed (N) of 350 rpm, which resulted in a 6 mm diameter (D) circular wear track on the disc specimen surface. The test duration (t) was set to be 2.5 hr. These test parameters were selected based on the previous wear loss data of similar alloys, ensuring that the wear losses of the tested alloys could be large enough to be identified under the load for the testing period, in the meanwhile, the load was not too high to cause the vibration and excessive friction heat. Three specimens were tested for each alloy under the same condition to verify the wear characteristics.

Table 4-1: Pin-on-disc wear test parameters.

Test environment	Room temperature
Sliding condition	Dry lubrication
Normal force (F)	5 N
Rotation speed (N)	350 rpm
Test duration (t)	2.5 hr
Diameter of wear track (D)	6mm

4.2 Experimental results

4.2.1 Wear track

After the wear tests, a circular wear track was generated in the worn surface of each specimen, as shown in Figure 4-2. It is the photographic worn surface of Stellite 21, shown as an example.

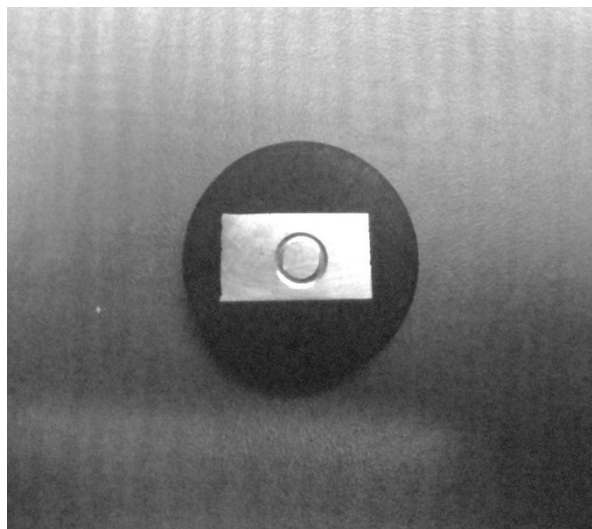


Figure 4-2: Worn surface of Stellite 21 after the pin-on-disc wear test.

According to ASTM G99-05(2010) [93], the wear test result is reported as the volume loss (V , mm^3) of tested material. To evaluate the volume of the wear track, which represents the amount of material removed from the specimen surface, a DEKTAK 150 surface profile measuring system, shown in Figure 4-3, was utilized to simulate the cross-section profile of each wear track. The system would collect the cross-sectional area by using the stylus sensor and then transfer the data to the plugged-in software. A two-dimensional cross-section profile was mapped by the software and the cross-sectional area was processed finally. In order to minimize the inaccuracy of the cross-sectional area, four locations were selected uniformly along each wear track to obtain the average cross-sectional area. The volume of each wear track (V , mm^3) was then calculated as the average cross-sectional area (A , mm^2) multiplied by the periphery length of the wear track (πD , mm), as illustrated in Figure 4-4.

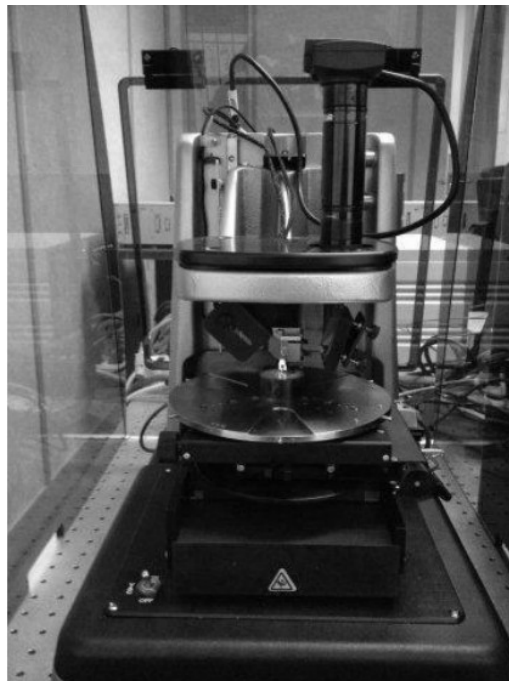


Figure 4-3: The DEKTAK 150 surface profile measuring system.

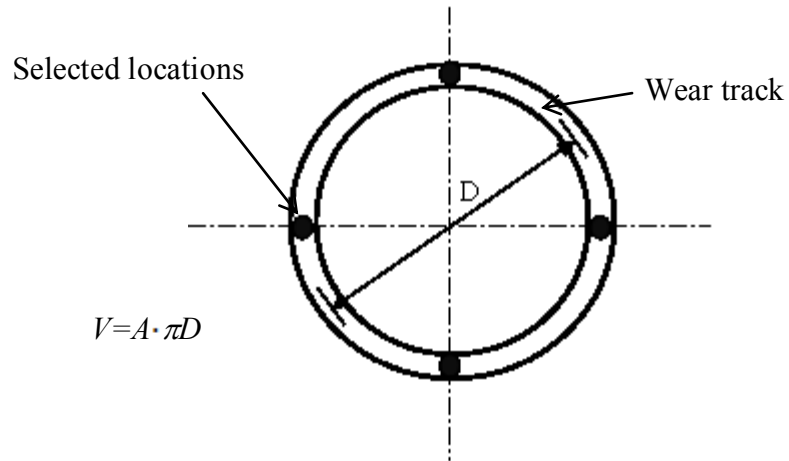
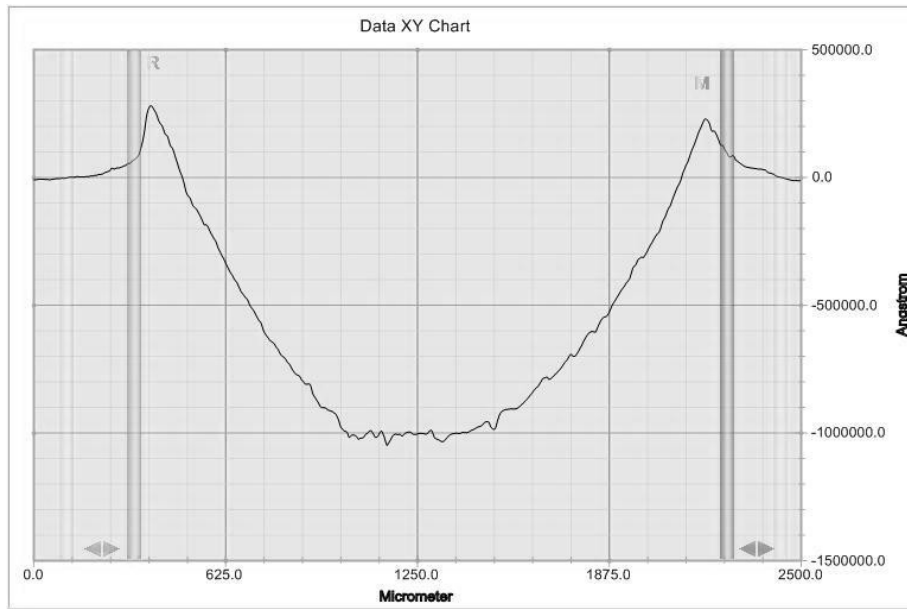


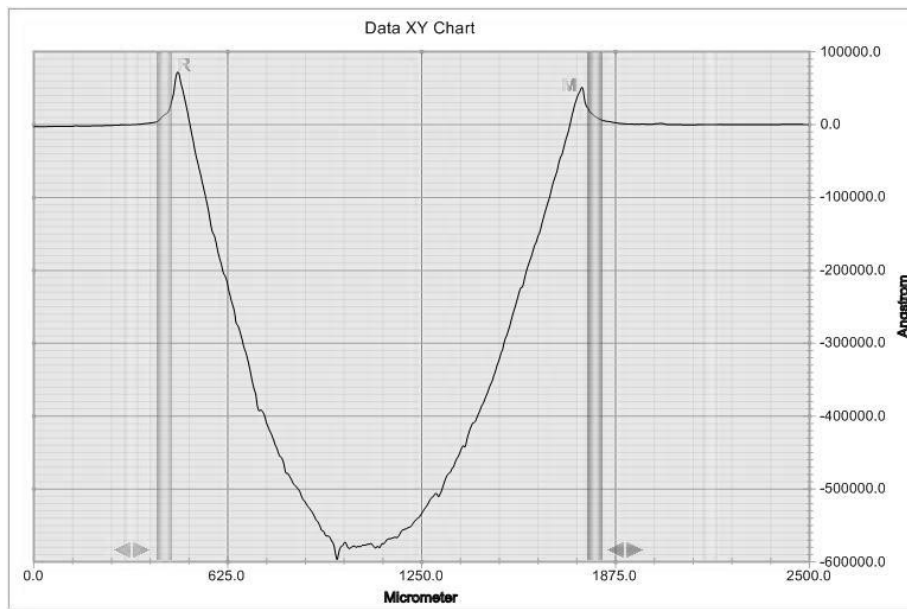
Figure 4-4: A schematic drawing for volume estimation of wear track.

4.2.2 Wear loss

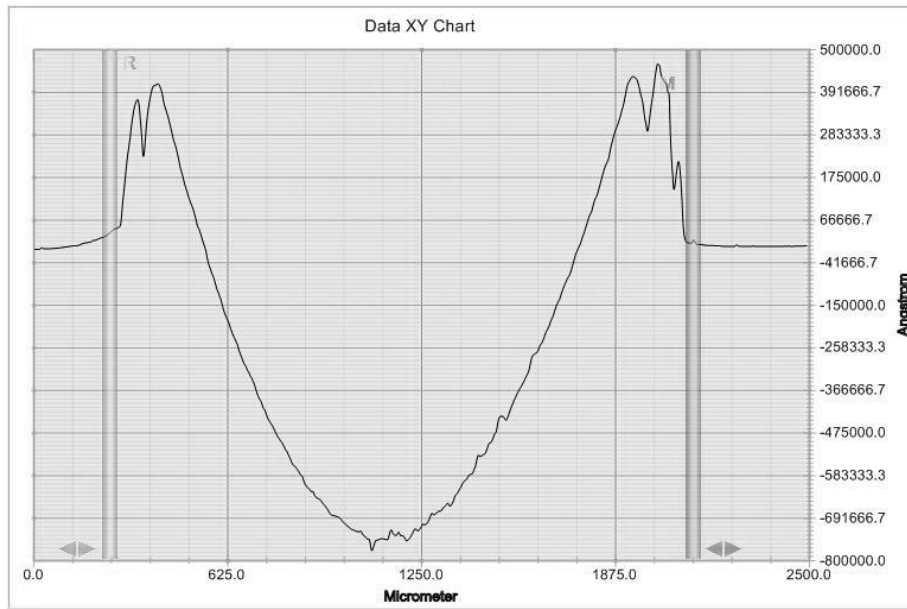
The typical cross section profiles of wear track for each tested alloy, obtained from the software in the DEKTAK 150 surface profile measuring system, are presented in Figure 4-5. The calculated volume values of the wear tracks, known as wear loss, are summarized in Figure 4-6. It is shown that under the same test condition Stellite 21 exhibited the lowest wear resistance while Stellite 720 the highest. This is explainable, because the volume fraction of carbides in the latter is much larger than in the former and the carbides are hard and wear-resistant which can strengthen the alloys. Compared with Stellite 21, the wear resistance of both modified Stellite 21 and nitrided Stellite 21 had been increased with additions of Cr or CrN. Between modified Stellite 21 and nitrided Stellite 21, the latter displayed better wear resistance.



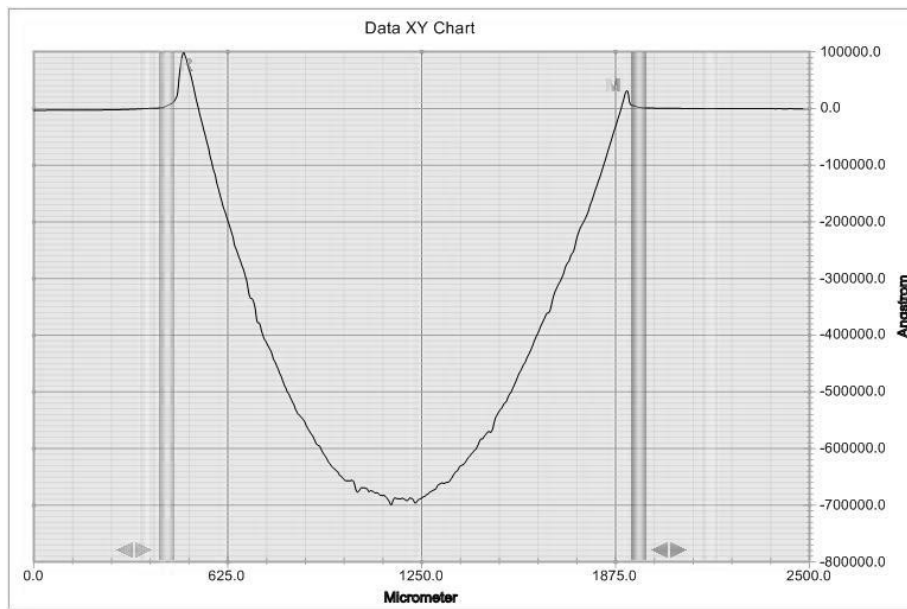
(a)



(b)



(c)



(d)

Figure 4-5: Cross section profiles of wear tracks: (a) Stellite 21, (b) Stellite 720, (c) modified Stellite 21, and (d) nitrided Stellite 21.

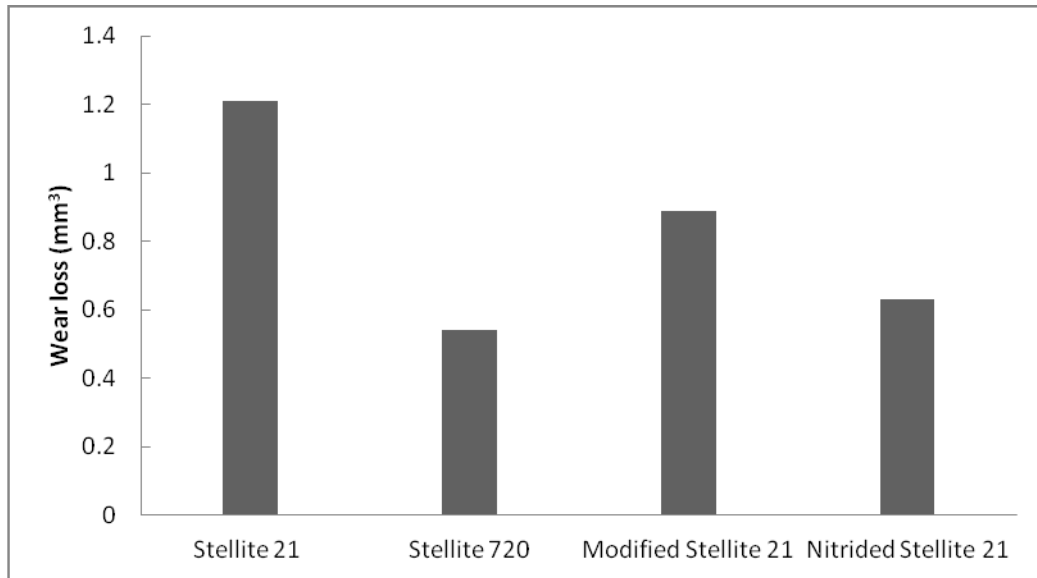


Figure 4-6: Wear losses (mm³) of the tested alloys.

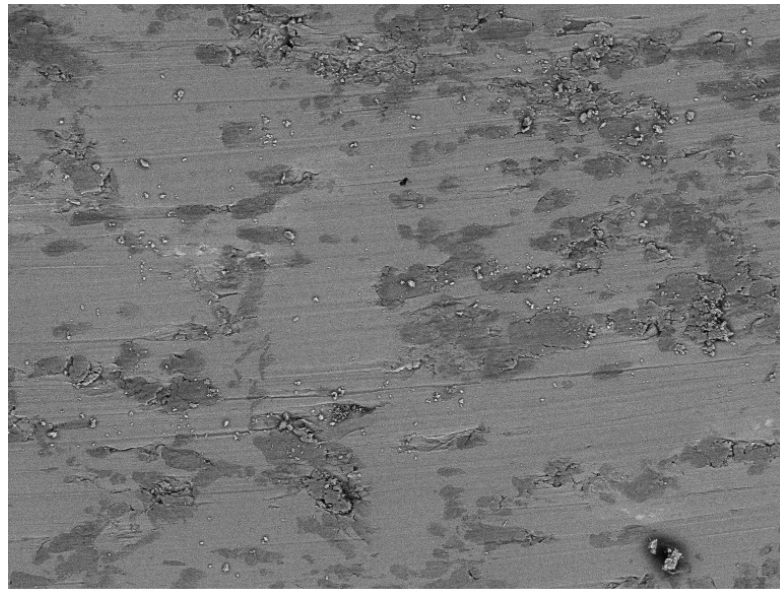
4.3 Worn surface analysis

To better understand the wear test results and further investigate the wear mechanisms of tested alloys, the worn surfaces of the alloy specimens were analyzed using SEM/EDX.

Stellite 21

The SEM images of worn surface of Stellite 21 specimen are shown in Figure 4-7. The morphology of the worn surface displayed severe plough scars with material removal in bulk (dark grey). In the image at high magnification, it is more evident that the material was dug out from the specimen surface, which left pits or scars in the surfaces. In addition, oxidation products (light spots) were found in the wear track, which implies that oxidation had occurred in the worn surface due to friction heat during the wear process. To further investigate the elemental compositions of the pits, EDX analysis was

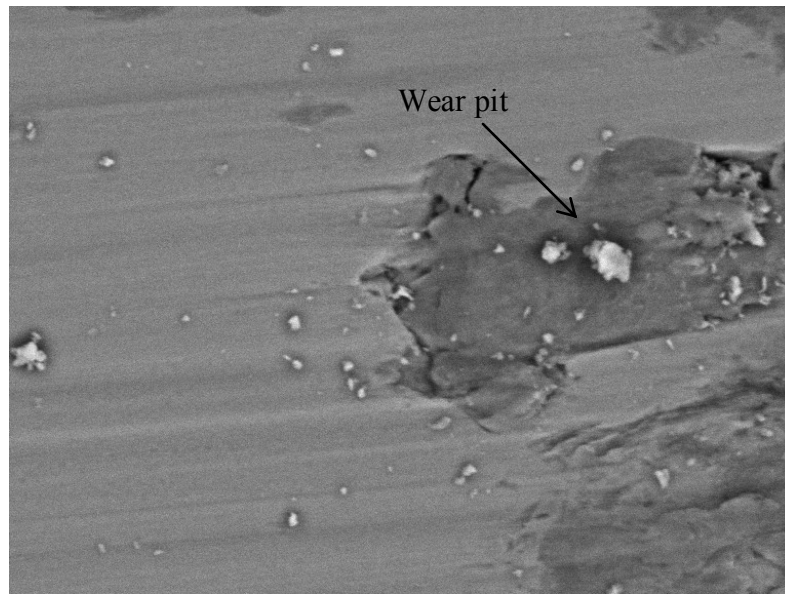
performed in the wear track and the results are presented in Figure 4-8. In the EDX spectrum, high oxygen was observed, which represents oxides (Cr-rich).



SEM MAG: 500 x
Det: BSE + LVSTD
View field: 300.0 μm

SEM HV: 20.00 kV
WD: 8.563 mm
Date(m/d/y): 03/20/13

(a)

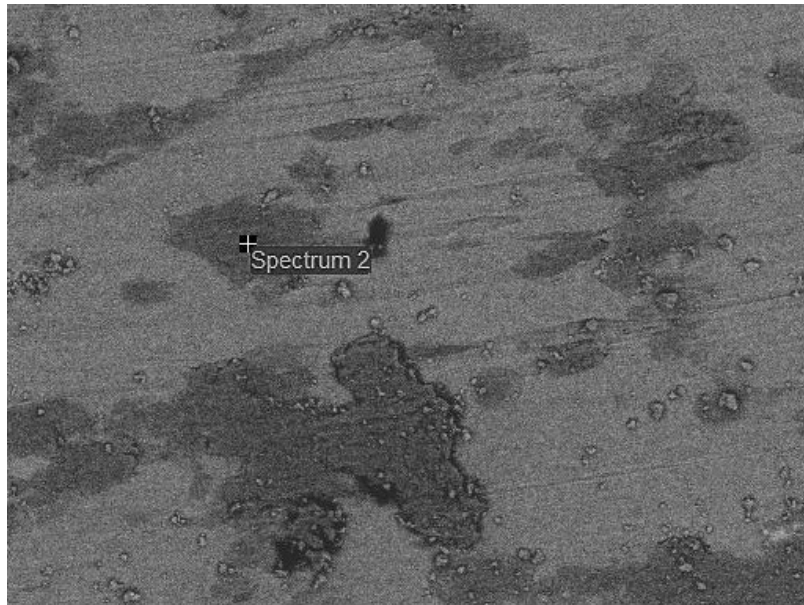


SEM MAG: 3,000 x
Det: BSE + LVSTD
View field: 50.00 μm

SEM HV: 20.00 kV
WD: 8.572 mm
Date(m/d/y): 03/20/13

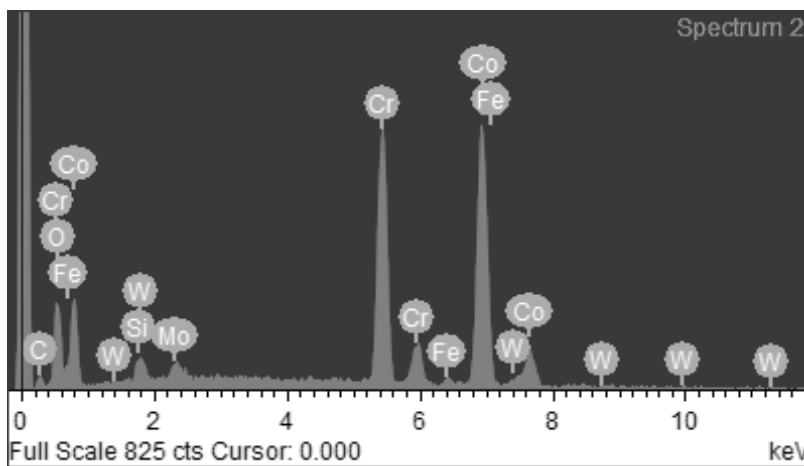
(b)

Figure 4-7: Worn surface of Stellite 21: (a) at low magnification, and (b) at high magnification.



90µm

Electron Image 1

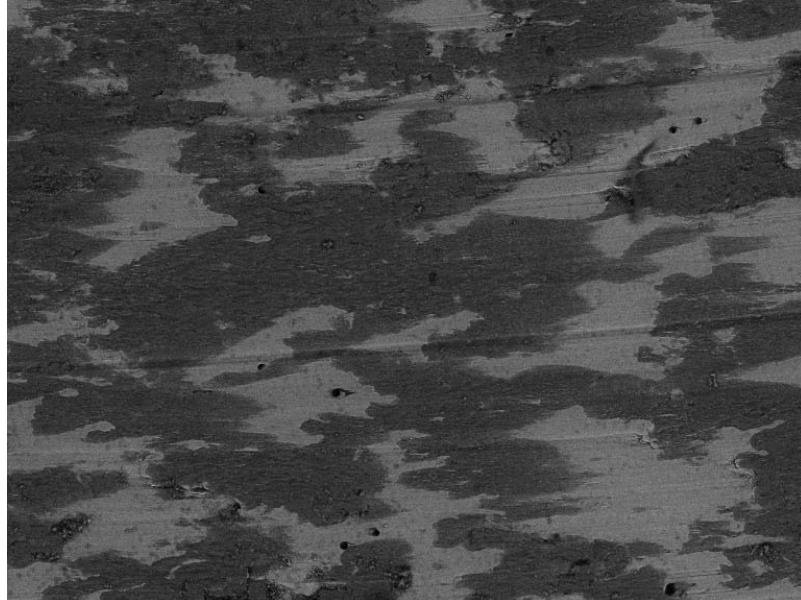


Element	Weight%	Atomic%
O K	10.3	29.18
Si K	0.68	1.09
Cr K	29.51	25.73
Fe K	1.03	0.84
Co K	54.17	41.67
Mo L	1.93	0.91
W M	2.38	0.58
Totals	100	100

Figure 4-8: EDX spectrum of wear track in the worn surface of Stellite 21.

Stellite 720

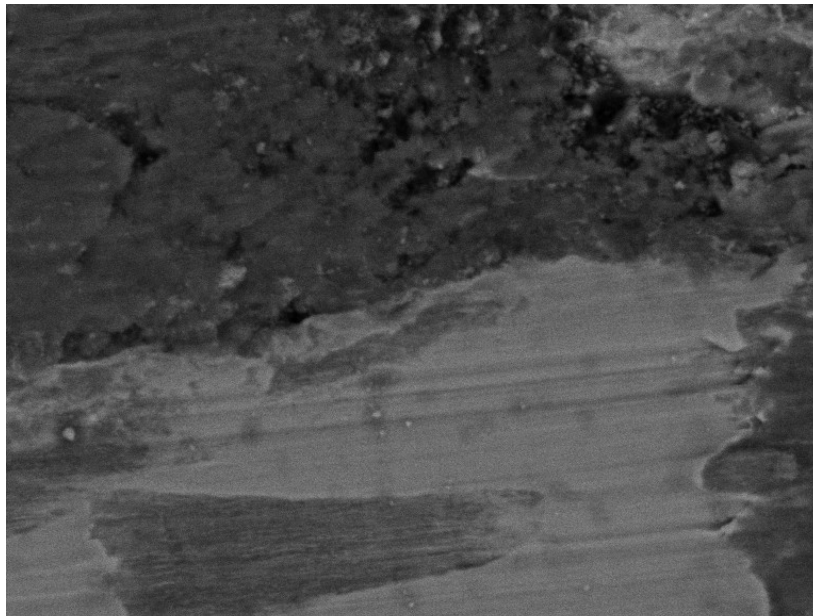
Compared with Stellite 21 specimen, the worn surface of Stellite 720 specimen was much smoother and no obvious material removal was observed, as seen in Figure 4-9. The wear loss of this alloy mainly came from chips but not bulk material. This is attributed to the large amount of carbides in this alloy, which enhanced its wear resistance. However, in the image at high magnification, local cracking and fracture were observed. This may be the result of carbides breaking. The EDX analysis results in Figure 4-10 also showed high oxygen content in the wear track, which indicates that Cr-rich oxides had been generated during the wear process.



SEM MAG: 500 x
Det: BSE + LVSTD
View field: 300.0 μ m

SEM HV: 20.00 kV
WD: 9.091 mm
Date(m/d/y): 07/03/13

(a)

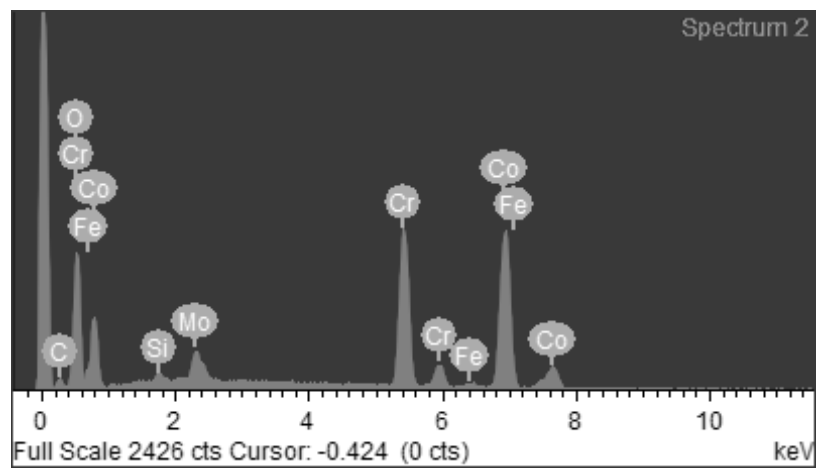
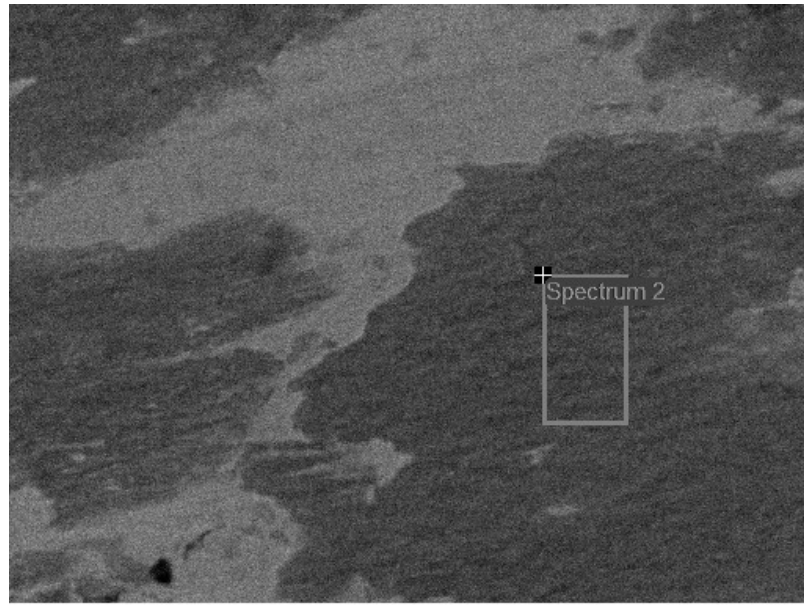


SEM MAG: 3.00 kx
Det: BSE + LVSTD
View field: 50.00 μ m

SEM HV: 20.00 kV
WD: 9.091 mm
Date(m/d/y): 07/03/13

(b)

Figure 4-9: Worn surface of Stellite 720: (a) at low magnification, and (b) at high magnification.

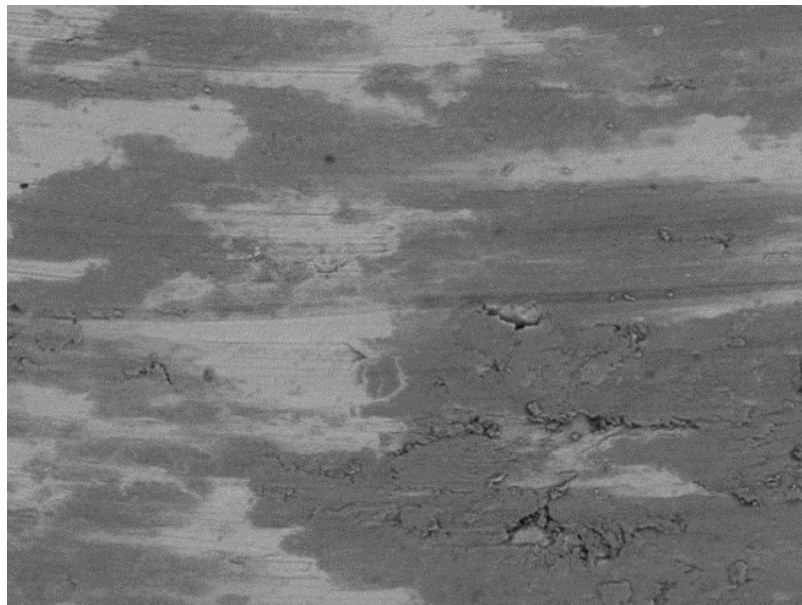


Element	Weight%	Atomic%
O K	23.33	29.18
Si K	0.39	1.09
Cr K	24.74	25.73
Fe K	0.66	0.84
Co K	46.28	41.67
Mo L	4.6	1.49
Totals	100	100

Figure 4-10: EDX spectrum of wear track in the worn surface of Stellite 720.

Modified Stellite 21

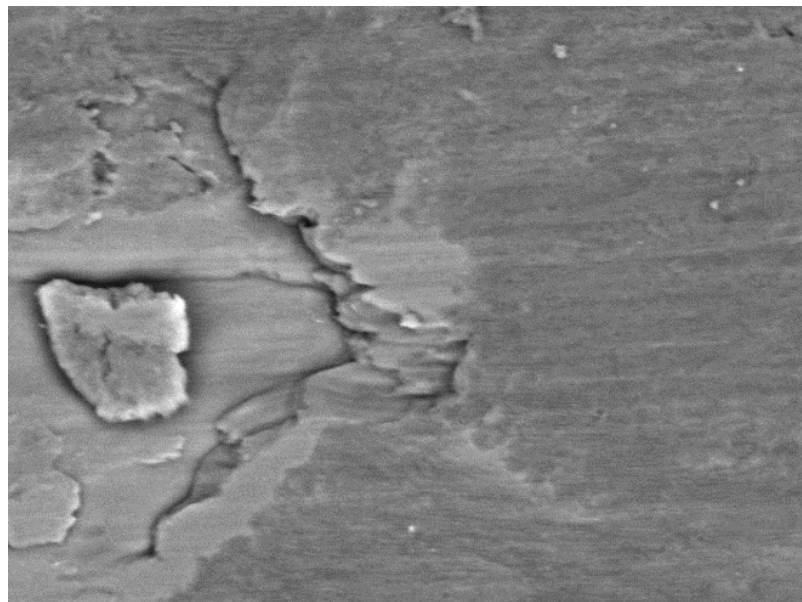
For the specimen of Stellite 21 with additional Cr content, modified Stellite 21, although the overall morphology of the worn surface showed plowing, the pits or scars in the surface were much less and shallow, as shown in Figure 4-11, compared with those in the worn surface of Stellite 21 specimen. The worn surface of modified Stellite 21 specimen also displayed local cracking and fracture within the wear track, as seen in Figure 4-11. Oxidation products were also observed in the worn surface, as can be seen from the image at high magnification in Figure 4-11(b). The EDX results of the fracture area are presented in Figure 4-12. Similarly, high oxygen was detected in this area, which confirms oxidation occurring in the surface during the wear process.



SEM MAG: 500 x
Det: BSE + LVSTD
View field: 300.0 μ m

SEM HV: 20.00 kV
WD: 8.400 mm
Date(m/d/y): 03/20/13

(a)

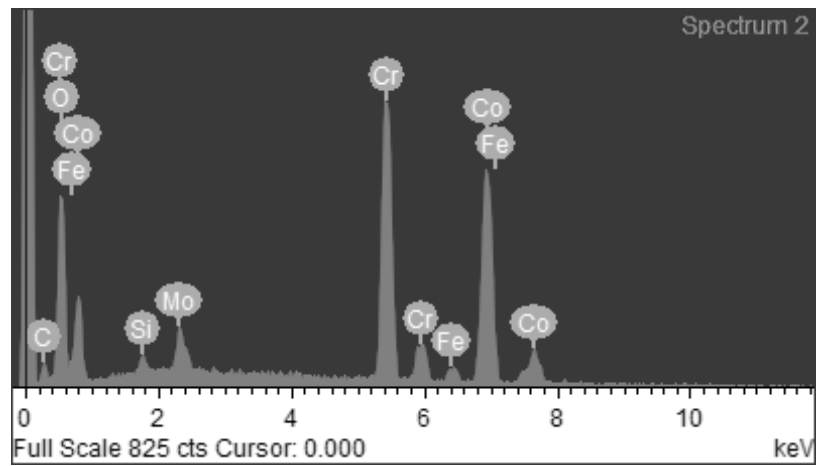
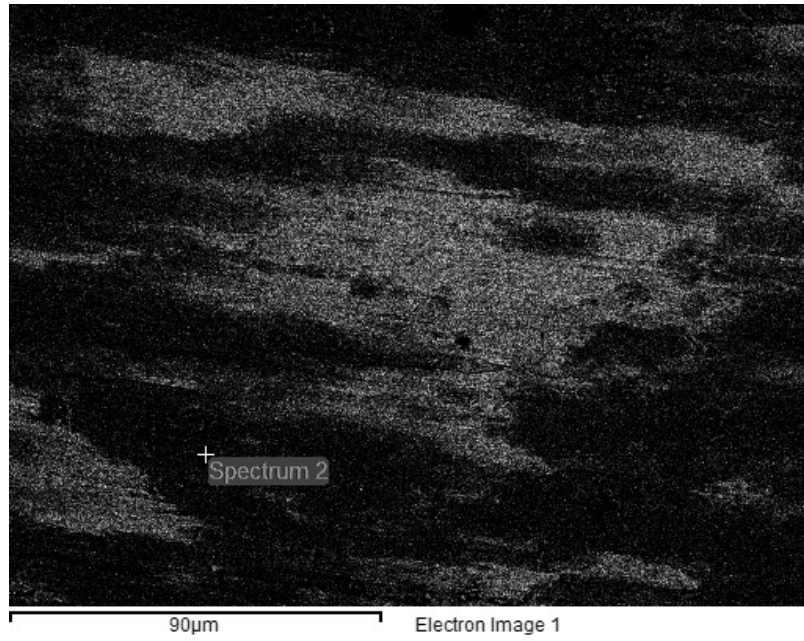


SEM MAG: 3.00 kx
Det: BSE + LVSTD
View field: 50.00 μ m

SEM HV: 20.00 kV
WD: 8.708 mm
Date(m/d/y): 03/20/13

(b)

Figure 4-11: Worn surface of modified Stellite 21: (a) at low magnification, and (b) at high magnification.

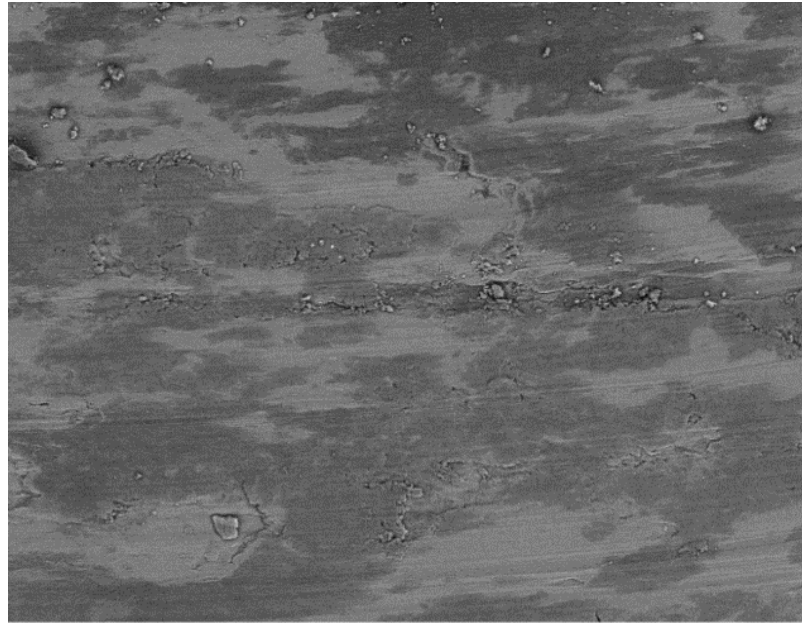


Element	Weight%	Atomic%
O K	21.64	29.18
Si K	0.73	1.09
Cr K	32.74	25.73
Fe K	2.10	0.84
Co K	38.23	41.67
Mo L	4.56	1.49
Totals	100	100

Figure 4-12: EDX spectrum of wear track in the worn surface of modified Stellite 21.

Nitrided Stellite 21

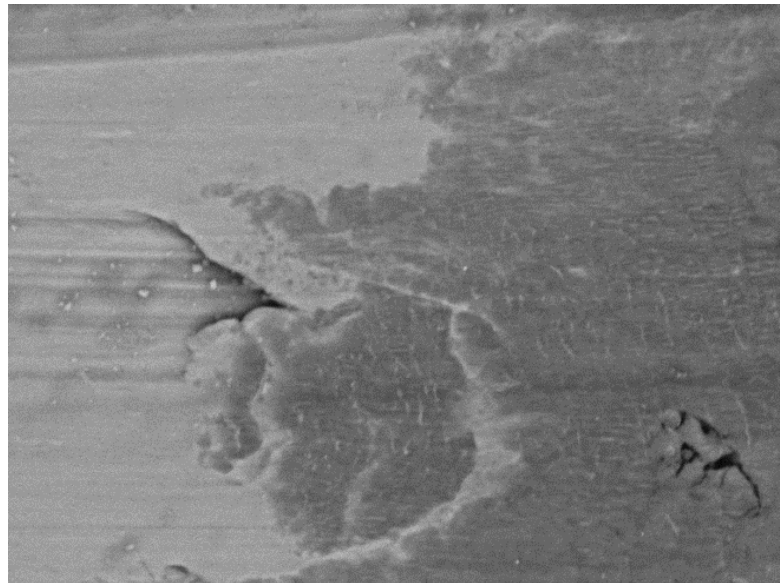
Comparing the worn surface of nitrided Stellite 21 in Figure 4-13 with those of Stellite 21 and modified Stellite 21, one may find that the nitrided Stellite 21 was much less damaged. The plowing scars were not obvious and very little local fracture can be observed in this alloy surface. However, similarly, high oxygen content was also detected in this worn surface by the EDX analysis, indicating the generation of Cr-rich oxide. The EDX spectrum is given in Figure 4-14.



SEM MAG: 500 x
Det: BSE + LVSTD
View field: 300.0 μ m

SEM HV: 20.00 kV
WD: 8.719 mm
Date(m/d/y): 03/20/13

(a)

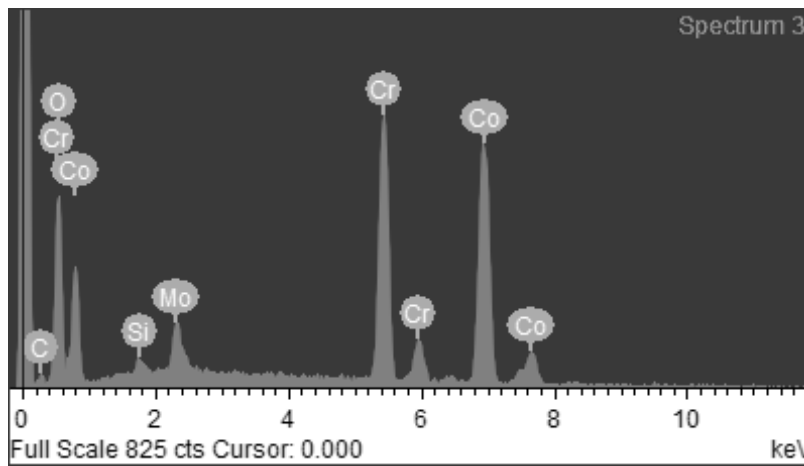
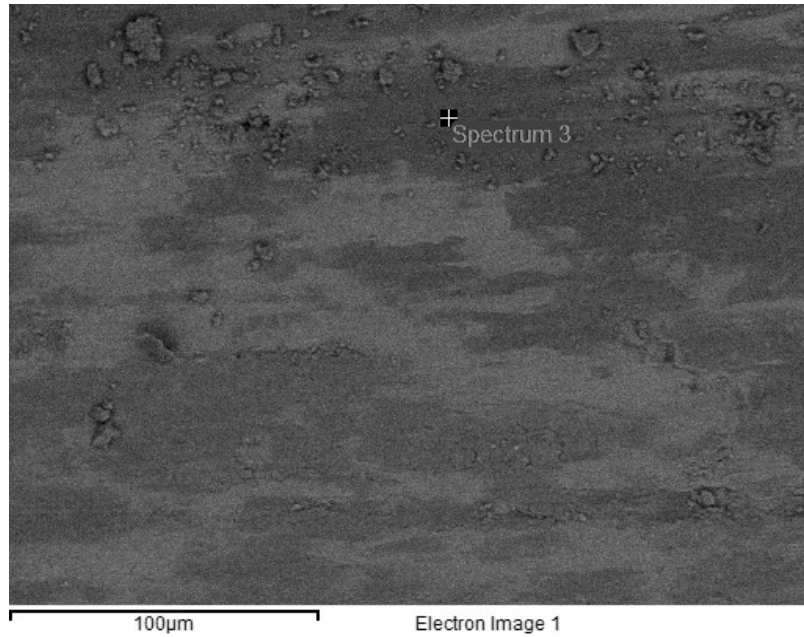


SEM MAG: 3.00 kx
Det: BSE + LVSTD
View field: 50.00 μ m

SEM HV: 20.00 kV
WD: 8.518 mm
Date(m/d/y): 03/20/13

(b)

Figure 4-13: Worn surface of nitrided Stellite 21: (a) at low magnification, and (b) at high magnification.



Element	Weight%	Atomic%
O K	20.23	47.54
Si K	0.65	0.88
Cr K	27.03	19.55
Co K	47.18	30.11
Mo L	4.91	1.92
Totals	100	100

Figure 4-14: EDX spectrum of wear track in the worn surface of nitrided Stellite 21.

As demonstrated in Figure 4-6, Stellite 21 had the worst wear resistance among the alloys under study, whereas Stellite 720 the best. The wear loss of the former was about double of that of the latter. The wear loss results are consistent with the morphologies of worn surface of these alloys. Due to the low carbon content thus a small volume fraction of carbides, the wear loss of Stellite 21 was mainly caused by material removal of the softer solid solution matrix under the wear load, which can be clearly seen in the high magnification image in Figure 4-7(b). Cracking and fracture of the solution matrix were found everywhere in the worn surface of this alloy, see Figure 4-7(a), which corresponds to the large wear loss of this alloy. On the contrary, owing to the very high C content (2.5 wt%), the high Cr content (33 wt%) and high Mo content (18 wt%), Stellite 720 are strengthened by both the solid solution matrix and the carbides, which rendered its worn surface with less cracking and damage. As seen in Figure 4-9, although the feature of plowing can be observed in the solid solution, the scars were shallow and no bulk material removal was found. On the other hand, due to brittleness of carbides, breaking and fracture of carbides can also be seen in the worn surface, which may contribute to the wear loss.

When compared with Stellite 21, modified Stellite 21 exhibited an improved wear resistance with 26% increase, see Figure 4-6. It was observed clearly in Figure 4-7 and Figure 4-11 that the overall wear scars and damage of the modified Stellite 21 surface were less than those of the Stellite 21. The main contribution to the increased wear resistance should be the additional Cr content in the former, which strengthened the solid solution matrix. As discussed previously, Stellite 21 contains a low level of C so that it is

a solution-strengthened alloy rather than a carbide-strengthened alloy. Therefore, its wear resistance is mainly controlled by the strength and hardness of the solid solution. Addition of Cr into Stellite 21 would benefit both of the properties, but not promote the formation of carbide due to the low C content. Strengthening of the solid solution matrix would lead to the increase in wear resistance for modified Stellite 21.

Addition of minor CrN into Stellite 21 had increased its wear resistance significantly, as seen in Figure 4-6, about 48%. The CrN particle itself can have strengthening effect when presented in the alloy and also new nitrides such as Mo-rich nitride may form with the presence of N during the HIP process at the high temperature. The great increase in wear resistance of nitrided Stellite 21 should be attributed to the formation of microdroplets which are C-rich and may also contain various nitrides. The presence of nitrides in the alloy can promote dissolution of C within the alloy. On the other hand, the C dissolved in the nitrides can reduce their brittleness and thus enhance their strength [77]. In consistence with the wear loss results, the worn surface of nitrided Stellite 21 showed much less severe wear scars, compared with that of Stellite 21.

The EDX spectra of wear track for the four alloys all showed high oxygen content, which implies that oxidation had occurred on the alloy surfaces during the wear processes. The temperature that caused oxidation of the alloys came from the friction heat. However, since the wear tests were conducted at room temperature, the friction heat, once generated, could dissipate immediately. In this case, oxidation of the specimen surfaces was not serious, as can be seen in the worn surfaces, oxides are found only in local

areas, not over the whole wear track. Therefore, the influence of oxides on the wear resistance of these alloys in this test condition was not concerned.

5 Chapter: Corrosion Resistance Evaluation

When immersed in the corrosive human body environment as hip implants, the materials will suffer from corrosion attack. Therefore, the corrosion resistance of the proposed Stellite alloys is another major consideration in this research.

5.1 Test specimens and solution

5.1.1 Specimen preparation

For corrosion tests, smooth and specular surfaces are required according to ASTM G5-13, standard reference test method for making potentiostatic and potentiodynamic anodic polarization measurements [94]. In this research, the specimens for corrosion tests were manufactured to round plates in a diameter of 16 mm and thickness of 1.6 mm. The specimens were then ground by using different sizes of silicon carbide (SiC) abrasive paper #240, #320, #400, and #600 to remove the received coarse surfaces, followed by polishing processes using polishing cloths plus 6 μm and 0.3 μm alumina powders. The specimens were cleaned up using water at each step of grinding and polishing to avoid debris sustaining. After polishing, chemical cleaning was employed to eliminate any traces of foreign particles from the specimen surfaces using methanol and the surfaces were then dried by compressed air. The specimens were degreased and rinsed in distilled water shortly before the corrosion tests.

5.1.2 Solution preparation

To simulate the real fluid environment of human body, numerous artificial physiological isotonic saline solutions have been applied in vitro studies, including Ringer's solution, Hank's solution and newborn calf serum [83]. In this research, the corrosion studies of the proposed alloys were conducted in Hank's solution. The composition of Hank's solution is given in Table 5-1.

Table 5-1: Chemical composition of Hank's solution [95].

Salt	Concentration (g/L)
NaCl	8.00
KCl	0.40
MgSO ₄ ·7H ₂ O	0.049
MgCl ₂ ·6H ₂ O	0.10
CaCl ₂ ·2H ₂ O	0.185
Na ₂ HPO ₄ ·12H ₂ O	0.121
KH ₂ PO ₄	0.06
NaHCO ₃	0.35
Glucose	1.00

The preparation of Hank's solution took the procedure as follows:

- (1) Pour 750 ml distilled water into a 1 L long neck glass vessel;
- (2) Weigh 0.121 g of Na₂HPO₄·12H₂O, 0.06 g of KH₂PO₄, 0.049 g of MgSO₄·7H₂O, 1.00 g of Glucose, 8.00 g of NaCl, 0.40 g of KCl, and 0.10 g of MgCl₂·6H₂O separately;
- (3) Mix the above chemicals and dilute them slowly into the 1 L long neck glass vessel;
- (4) Weigh 0.185 g of CaCl₂·2H₂O;
- (5) Dilute the CaCl₂·2H₂O with 100 ml distilled water in a 500 ml beaker;
- (6) Pour the CaCl₂ solution from the beaker to the 1 L long neck glass vessel;
- (7) Weigh 0.35 g of NaHCO₃;
- (8) Dilute the NaHCO₃ with 100 ml distilled water in a 500 ml beaker;

- (9) Pour the NaHCO_3 solution from the beaker to the 1 L long neck glass vessel;
- (10) Fill the glass vessel with distilled water until it gets to 1 L, stir the solution with a glass stick to make sure that the chemicals are homogeneously dissolved;
- (11) Seal the vessel and store it in the fridge at 4°C .

The solution was measured by a pH meter to ensure a pH value of 7.4.

5.2 Electrochemical tests

5.2.1 Test setup

The corrosion behavior of the Stellite alloys studied in this research was investigated under electrochemical tests first, which included open circuit potential (OCP), cyclic polarization, potentiostatic and electrochemical impedance spectroscopy (EIS) tests. The experimental system consists of an electrochemical cell and a control system that includes a data acquisition and analysis system. A schematic diagram of the experimental test setup is shown in Figure 5-1.

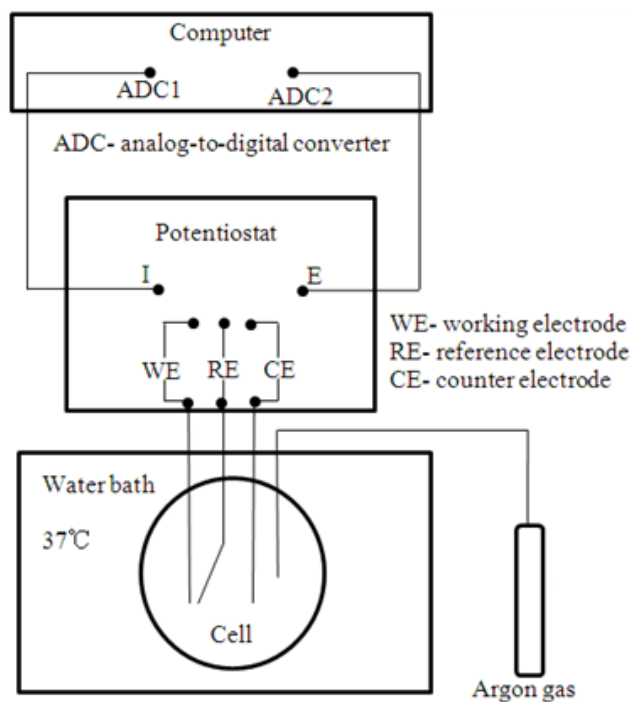


Figure 5-1: The schematic diagram of the electrochemical test setup.

Two types of potentiostats were used for the data gathering: Solartron 1287 potentiostat with a Solartron 1255 gain/phase analyzer and Gamry PC4/300 potentiostat. The results derived from the two instruments for a same sample were very close. Instead of measuring the impedance directly, the potentiostats measure the potential (E) and the current (I) [96]. Both test systems use a four-terminal connection scheme. The four leads that connect to the cell under test are grouped into two pairs. One pair is ‘current-carrying leads’ that conduct the current between the cell and the potentiostat, and the other is ‘sense leads’ that measure the voltage across two points in the cell [97]. With the different potentiostats, different computer programs were employed to perform the measurements and data analysis. In the case of the Solartron potentiostat, for performing the direct current (DC) experiments and cyclic polarization, CorrWare (3.2c) and CorrView (3.2d) software packages (Scribner Associates) were used. For performing the

EIS experiments, ZPlot (3.2c) and ZView (3.2d) software packages (Scribner Associates) were used. For the Gamry systems, GamryFramework (4.35) software was used for the data collection while EchemAnalyst (5.3) was used for data viewing and analysis.

As shown in Figure 5-2, the electrochemical cell provides the corrosive environment (600 ml Hank's solution). The corrosion cell is a 1 liter flat bottom flask with ground glass joints, which can be used at temperatures ranging from room temperature up to 100°C and is inert to common solutions. The cell is a typical three-electrode cell which includes a working electrode (WE), a counter electrode (CE), and a reference electrode (RE). The WE was placed in the center of the flask. The specimen was mounted on a Teflon holder and the testing surface was pressed against an O-ring, which resulted in an exposed surface area of 0.785 cm². The O-ring also ensured a tight-sealed surface. A CE was introduced so that the circuit between the WE and the electrolyte can be either applied or measured. The CE is often fabricated from electrochemically inert materials such as gold, platinum, or carbon. In this research, a carbon rod was employed as the CE and was adjusted to face the specimen surface so as to balance the current flow. As the absolute potential of the WE could not be measured, a RE with a stable and well-known electrode potential was introduced. A saturated calomel electrode (SCE, Fisher scientific) with a potential of +0.244 V was taken as the RE and all potential values measured were quoted against the SCE. To minimize the extraneous potentials caused by the potential ($V = IR$) drop between the electrolyte and the WE, a bridge probe was employed and extended from the RE to ensure that the RE and the WE was very

close to each other but not touching. The bubbling tube (consisting of gas inlet and gas outlet) was used for argon gas purging.

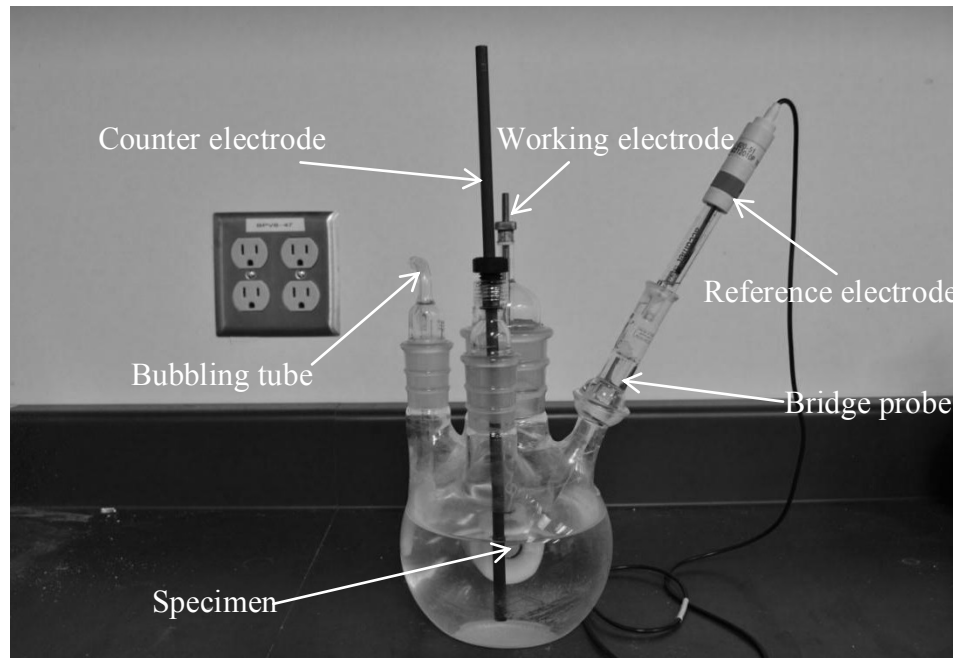


Figure 5-2: Electrochemical cell assembly.

The cell was then put in a water bath (Anova Inc.) filled with tap water. The test environment was set at a constant temperature of 37°C. The electrodes were connected to the potentiostat. The whole setup for the electrochemical tests is shown in Figure 5-3.

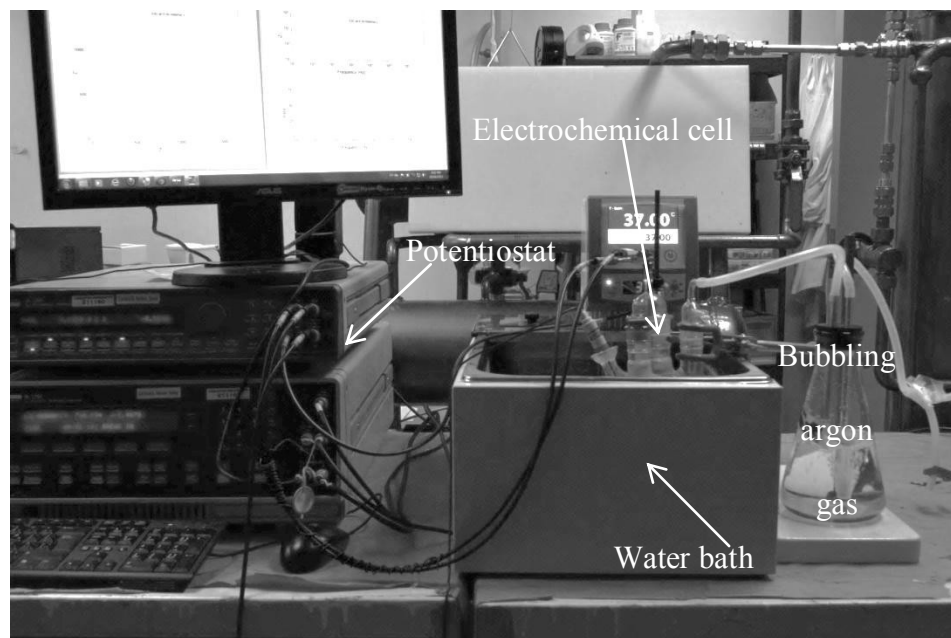


Figure 5-3: The experimental setup for electrochemical tests.

5.2.2 Test procedure

Before each test, the electrolyte (Hank's solution) was bubbled and deaerated by pure argon gas through the bubbling tube for at least 40 min. Electrochemical tests were performed on each type of alloy: (1) corrosion potential measurement, (2) cyclic polarization, and (3) potentiostatic measurements. During the potentiostatic tests, the current response was monitored as a function of time and EIS spectra were periodically recorded to characterize the corrosion behavior of the metal.

As described in Chapter 2, the corrosion potential (E_{corr}) or the open circuit potential (OCP) is the equilibrium potential when the net current measured on the metal/electrolyte interface is zero. The E_{corr} was recorded as a function of time for 40 hr in this test whose value reflected all of the processes causing corrosion. The potential can be considered steady if the fluctuation of the E_{corr} is within 0.003 V/hr.

The cyclic polarization was performed to predict long term tendency of phenomena such as localized corrosion or high levels of general corrosion. After the E_{corr} reached a steady state, the polarization scan departed at E_{corr} and reached 1 V_{SCE} with a scan rate of 1 mV/s, the scan was then immediately reversed from 1 V_{SCE} back to E_{corr} at the same scan rate. It is important to mention that the cyclic polarization scan must be generated only after the OCP is stable. Potentials such as E_{pit} and E_{prot} themselves have little meanings. Only relative to E_{corr} , their values have meanings for corrosion prediction of the tested materials. The scan rate was controlled at a low speed of 1 mV/s so that the current/voltage relationship could reflect the interfacial corrosion process at every potential of the polarization scan. In the meantime, a reasonable amount of experimental time was guaranteed.

Each specimen was rested for at least 1 hr before measurement until the equilibrium status was reached. The potential was then stepped to a preselected value of 0.2 V_{SCE}, 0.5 V_{SCE}, 0.75 V_{SCE}, and 0.9 V_{SCE}, respectively. The corresponding current was recorded for a period of 1000 s. An interval time of 15 min was guaranteed between two potentiostatic potentials so that the specimens could be fully rested. The current was also recorded for 40 hr at E_{corr} .

The EIS was measured after each potentiostatic step. In order to obtain satisfactory EIS data and avoid any external noises, an integration function is available in the Solartron instrument. Integration time is the period over which the analyzer measures the input

signal. Defined in second, the integration time is rounded up or down to cover different numbers of cycle. For example, it would take $1/10^{-6}$ s to complete the 1 MHz measurement in 1 cycle and 17 min to do 1 cycle at 10^{-3} Hz, while over 11 days will be required to complete the 10^{-3} Hz measurement in 1000 cycles. In this research, as a balance between the test time and the satisfactory EIS curve, all the EIS spectra were performed from a high frequency (10^5 Hz) down to a low frequency (10^{-1} Hz) within an integration time of 300 s at an AC excitation voltage of 20 mV. In this method, 30 cycles were performed at 10^{-1} Hz so that smooth EIS curves could be obtained.

Duplicate tests were performed for each case to verify the repeatability of the test data.

5.3 Electrochemical tests results and analysis

5.3.1 Open circuit potential

The open circuit potential results of the tested alloys are presented in Figure 5-4. It is shown that the OCPs of Stellite 720 ($-0.142 V_{SCE}$) and modified Stellite 21 ($-0.2218 V_{SCE}$) were established quickly in about 20 min and 40 min, respectively. This is due to the high Cr content in the alloys which is the main contributor of forming protective oxide film. It took about 3 hr for nitrided Stellite 21 to reach the steady-state value ($-0.065 V_{SCE}$), which may be due to the fact that nitrided Stellite 21 was sluggish in forming a passive film. The OCP of Stellite 21 was stable at about $-0.336 V_{SCE}$ in 1.5 hr and fluctuated a bit over the measurement. The previous studies [98, 99] reported that the OCP of an alloy was not necessary to be directly proportional to the corrosion resistance

of the alloy. However, it is closely related to the pitting potential and the repassive potential, which can be described by the cyclic polarization curves.

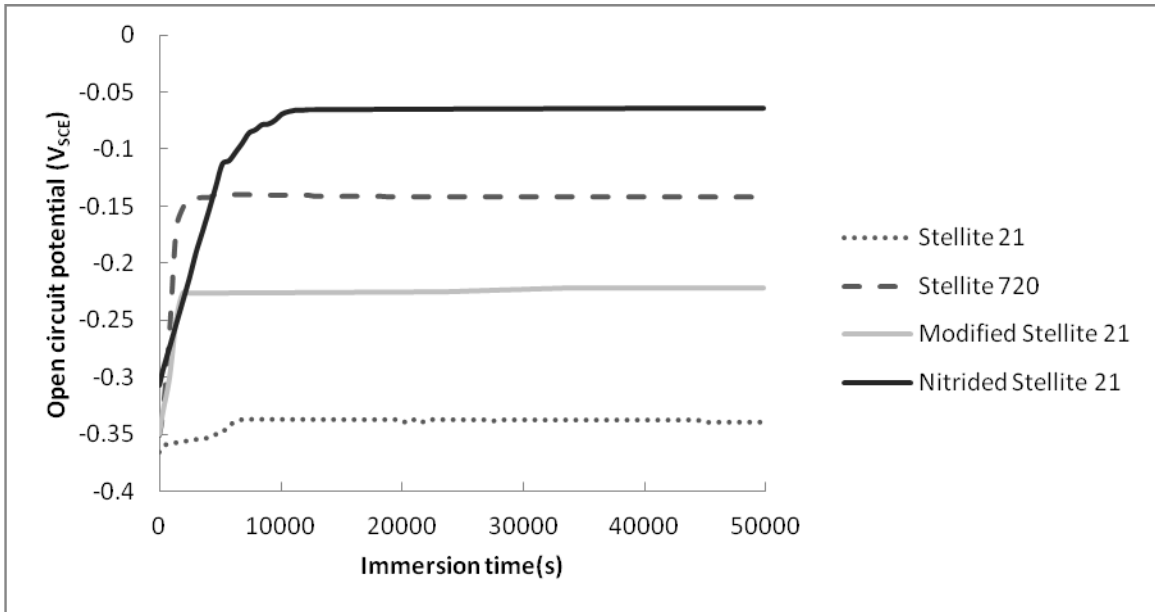


Figure 5-4: OCP curves as a function of time for the Stellite alloys in Hank's solution with pH 7.4 at 37°C. For clarity, data are shown only for the first 50000 s of the exposure time.

5.3.2 Cyclic polarization curves

The cyclic polarization curves of the tested alloys after 40 hr immersion in Hanks's solution at 37°C are presented in Figure 5-5 to Figure 5-8. For comparison, these curves are also plotted together in Figure 5-9. With the current density varying from 10^{-9} A/cm² to 10^{-2} A/cm², the current density axis (the horizontal axis) is plotted logarithmically. It is seen that nitrided Stellite 21 achieved the highest corrosion current density (9.92×10^{-6} A/cm²), which was almost three-order higher than that of modified Stellite 21 (9.5×10^{-9} A/cm²).

A remarkable increase in current was observed in the forward scan of all the four alloys at potential $\sim 0.4 V_{SCE}$. Moreover, when the potential was $\sim 0.75 V_{SCE}$ and above, the corrosion behavior of the alloys was almost the same. These can be explained by the Cr and Co pourbaix diagrams in Figure 5-10 and Figure 5-11. Other researchers found the similar potential-pH behavior of Cr at $100^{\circ}C$ when compared to that at $25^{\circ}C$ [100], from which one can assume that the difference of diagrams between $25^{\circ}C$ and $37^{\circ}C$ is likely to be small. At the solution pH value of 7.4, the current was relatively small at the potential below $0.4 V_{SCE}$ because of the formation of Cr_2O_3 oxide film. With the different type and amount of alloying elements, the thickness of the Cr_2O_3 film might vary, resulting in variable current values. For example, with higher Cr content in Stellite 720 and modified Stellite 21, these alloys had lower current values at the same potential when compared to the other two alloys. From $0.4 V_{SCE}$ to $0.75 V_{SCE}$, the Cr_2O_3 scale broke down and the metal/solution interface started to generate chromite ion CrO_4^{2-} , which was one of the reasons causing the increased current. In this potential range, the Co stayed in the state of Co^{2+} . When the potential arrived at $0.75 V_{SCE}$ and above, the working electrodes had completely dissolved as chromite ions CrO_4^{2-} while the Co started to form Co hydroxide $Co(OH)_3$. In this potential zone, the current values showed the second distinct increase and were similar for the four alloys. Moreover, obvious fluctuation was found on every working electrode, indicating a relatively slow $Co(OH)_3$ formation and a relatively fast CrO_4^{2-} dissolution.

For the reverse scan, only modified Stellite 21 showed negligible electronegative hysteresis and carried a higher E_{prot} ($0.531 V_{SCE}$). A small difference between E_{prot} and

E_{pit} (0.488 V_{SCE}) indicated better pitting resistance of this alloy. On the other hand, the other three alloys had various degrees of hysteresis. Electrochemical parameters such as corrosion potential (E_{corr}), corrosion current density (i_{corr}), pitting potential (E_{pit}) and protection potential (E_{prot}) obtained from these curves are summarized in Table 5-2.

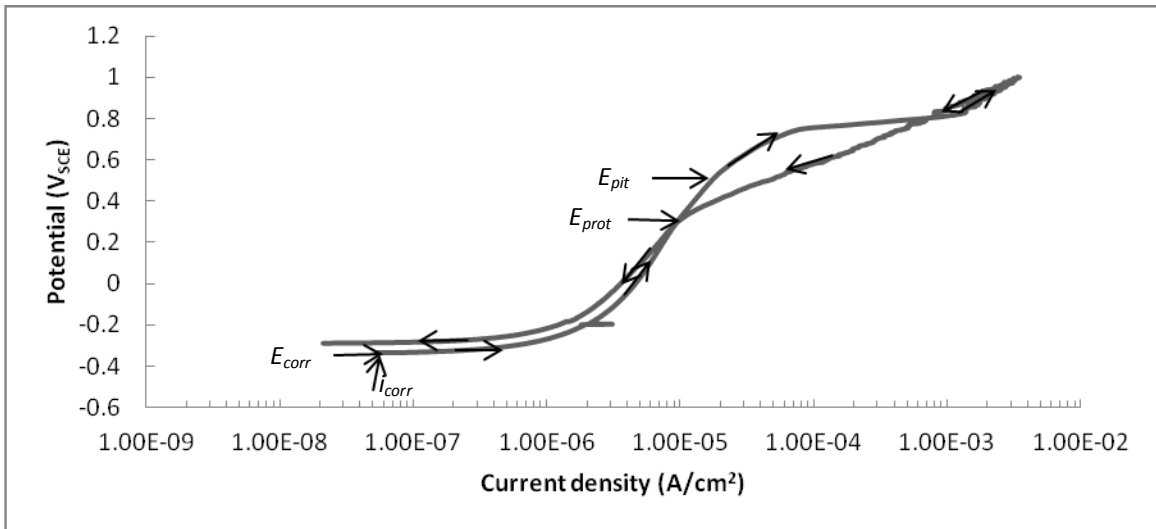


Figure 5-5: Cyclic polarization curve of Stellite 21 in Hank's solution with pH 7.4 at 37°C.

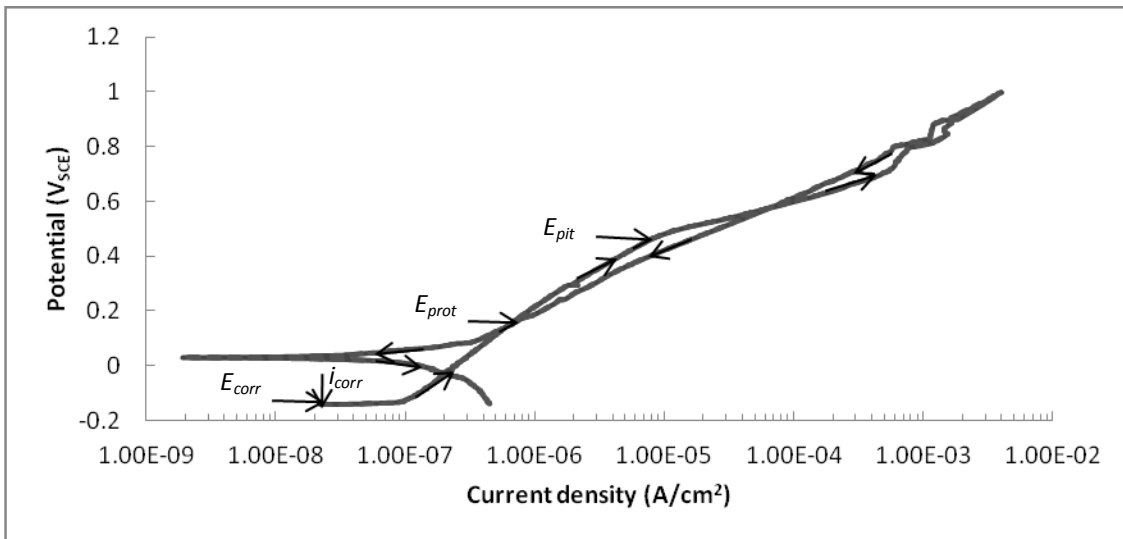


Figure 5-6: Cyclic polarization curve of Stellite 720 in Hank's solution with pH 7.4 at 37°C.

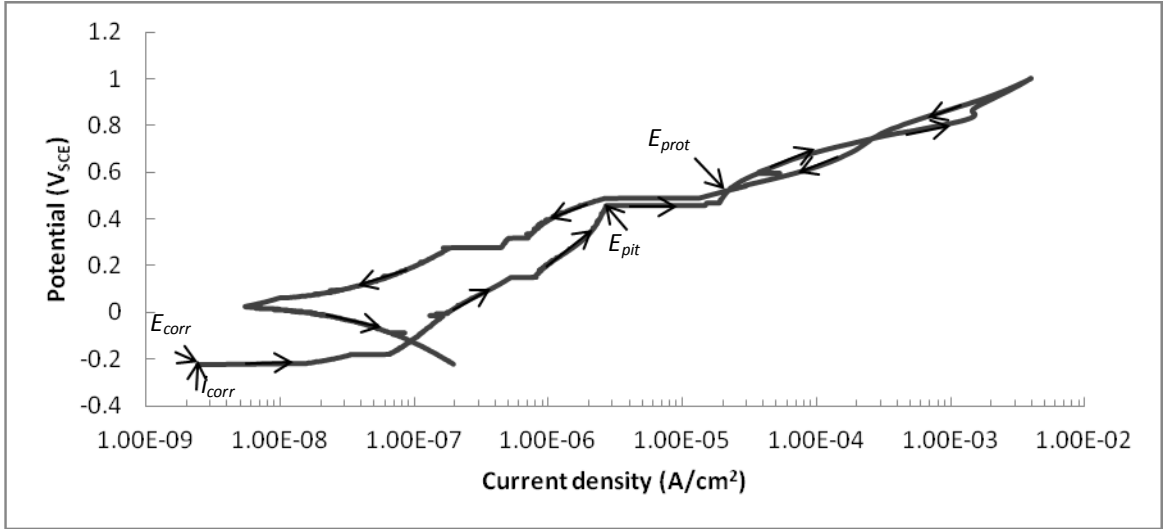


Figure 5-7: Cyclic polarization curve of modified Stellite 21 in Hank's solution with pH 7.4 at 37°C.

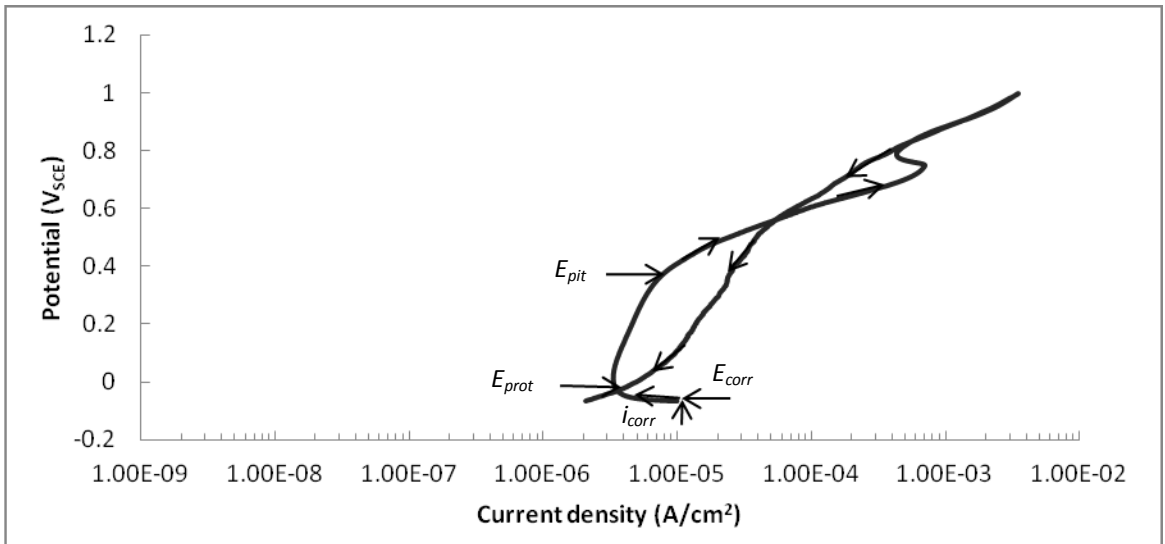


Figure 5-8: Cyclic polarization curve of nitrided Stellite 21 in Hank's solution with pH 7.4 at 37°C.

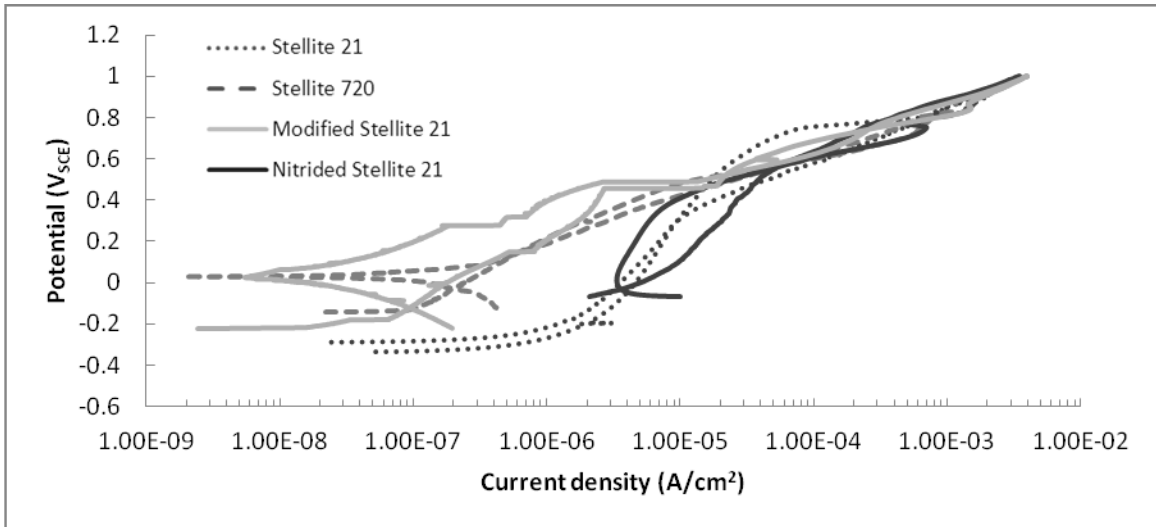


Figure 5-9: Cyclic polarization curves of Stellite alloys in Hank's solution with pH 7.4 at 37°C.

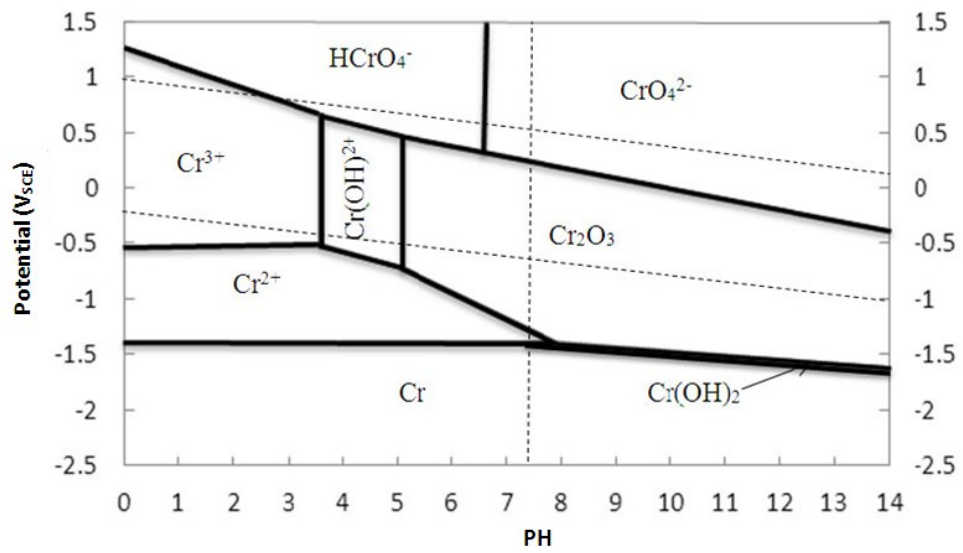


Figure 5-10: Potential-pH equilibrium diagram for the deaerated chromium-water system at 25°C.

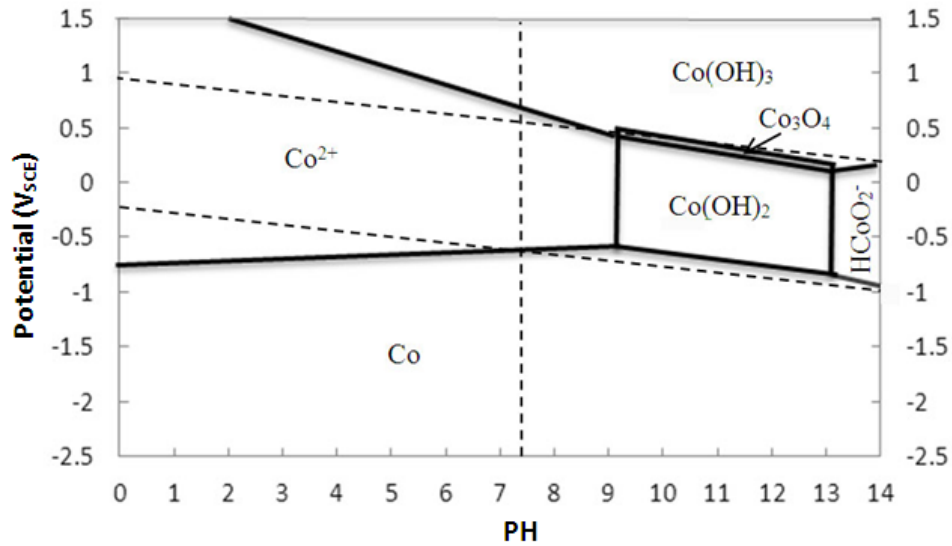


Figure 5-11: Potential-pH equilibrium diagram for the deaerated cobalt-water system at 25°C.

Table 5-2: Cyclic polarization data of the tested alloys in Hank's solution with pH 7.4 at 37°C.

Alloy	E_{corr} (V _{SCE})	i_{corr} (A/cm ²)	E_{pit} (V _{SCE})	E_{prot} (V _{SCE})
Stellite 21	-0.336	5.21×10^{-8}	0.449	0.303
Stellite 720	-0.142	2.22×10^{-8}	0.461	0.171
Modified Stellite 21	-0.2218	2.42×10^{-9}	0.488	0.531
Nitrided Stellite 21	-0.065	9.92×10^{-6}	0.333	-0.049

The differences between E_{corr} and E_{pit} , and between E_{pit} and E_{prot} are plotted in Figure 5-12. The values of $E_{pit} - E_{corr}$ of Stellite 21 and modified Stellite 21 were close, but the values of $E_{pit} - E_{prot}$ of these two alloys were very different. As illustrated in Figure 5-12, the former was 0.148 V_{SCE} while the latter was -0.043 V_{SCE}, which indicates a superior localized corrosion resistance of modified Stellite 21. Although the current value of

Stellite 720 at the same potential was almost one-order lower than that of Stellite 21, the hysteresis loop size of Stellite 720 was larger than that of Stellite 21, which implies that more pits and ion release would occur in Stellite 720 after a long period of exposure in the solution. Nitrided Stellite 21 displayed the worst localized corrosion resistance with respect to both of the measurements.

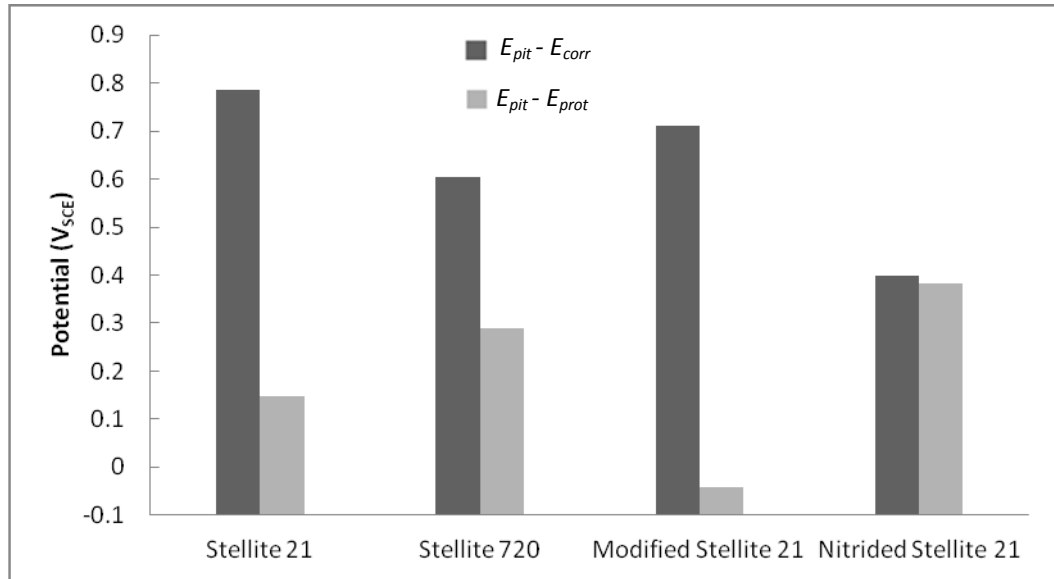


Figure 5-12: Localized corrosion resistance of the tested alloys.

5.3.3 Potentiostatic measurements

Although the cyclic polarization test can provide guiding information about the corrosion behavior of the alloys, more details can be illustrated by the potentiostatic and EIS curves, which are obtained with longer time duration at each potential stage.

The overall corrosion behavior of the four tested alloys at each potentiostatic stage was similar so that only two of them were analyzed here as examples. The potentiostatic current transients for modified Stellite 21 and Stellite 21 are shown in Figure 5-13. As

the potentials were directly stepped to the designed potentials, the initial current was normally two orders higher in the first few seconds before it became relatively stable. As can be seen in the figure, this duration time was shorter for modified Stellite 21 than for Stellite 21 which can be attributed to the higher Cr content in the former. At $0.2 V_{SCE}$, the current decreased slowly and steadily along with the time shifting after the short-term drop. The corrosion behavior at this potential can be related to the characteristics of Cr_2O_3 film growth. At $0.5 V_{SCE}$ the current difference between the two alloys was smaller than at $0.2 V_{SCE}$, which indicates that the protective film started to break down by the anodic potential attack at this higher potential. The current at this potential was still relatively stable, unlike the currents at $0.75 V_{SCE}$ and $0.9 V_{SCE}$. This may be due to the sustaining film on the surface. From $0.75 V_{SCE}$ and above, the current fluctuated considerably throughout the testing time, which was consistent with the instability observed in the cyclic polarization tests. This fluctuation resulted in totally corroded surfaces. The currents at $0.9 V_{SCE}$ for these two alloys were almost the same.

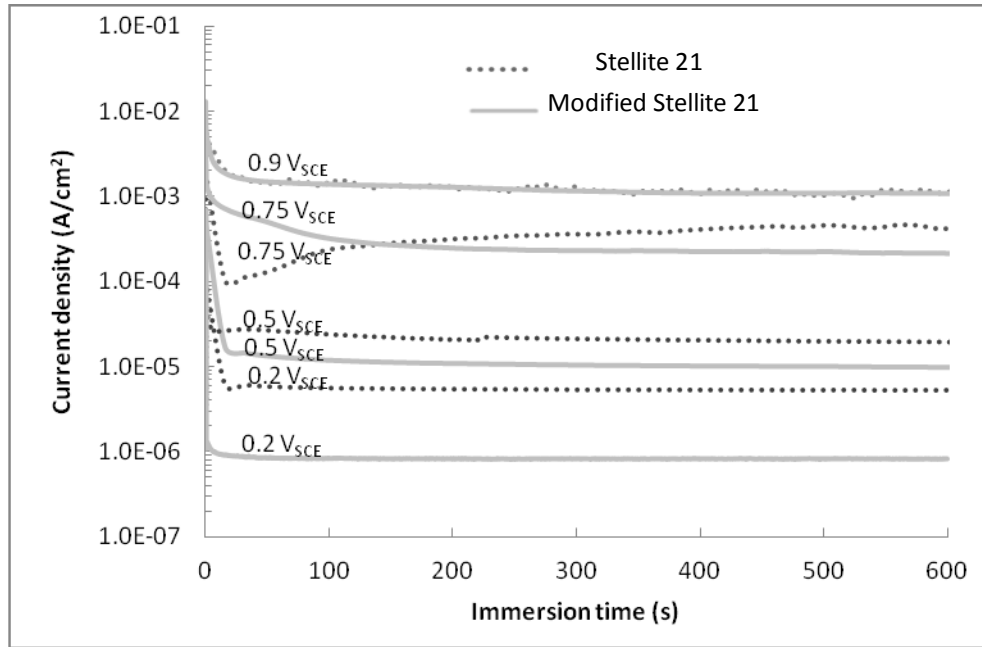


Figure 5-13: Potentiostatic current transients for Stellite 21 and modified Stellite 21 at constant potentials of 0.2 V_{SCE}, 0.5 V_{SCE}, 0.75 V_{SCE}, and 0.9 V_{SCE}, respectively. For clarity, data are shown only for the first 600 s of the exposure time.

The current behavior of the tested alloys at E_{corr} for about 40 hr was recorded and is illustrated in Figure 5-14. According to ASTM G102-89 [101], standard practice for calculation of corrosion rates and related information from electrochemical measurements, the obtained current density can be converted to general corrosion rate. The equations are given as follows:

$$CR = K_1 \frac{i_{corr}}{\rho} EW, \quad (5.1)$$

where

CR is corrosion rate in mm/yr;

EW is alloy equivalent weight, i.e., the mass of the alloy in gram that will be oxidized by the passage of one Faraday ($96489 \pm 2C$) of electric charge;

i_{corr} is the current density of the alloy in $\mu\text{A}/\text{cm}^2$. In this calculation, the average of the

i_{corr} value after relative stability was taken as the calculation value of i_{corr} ;

$K_I = 3.27 \times 10^{-3} \text{ mm}\cdot\text{g}/\mu\text{A}\cdot\text{cm}\cdot\text{yr}$, and;

ρ is the density of the alloy in g/cm^3 . The density of Stellite 21 specimen used in this study is $8.33 \text{ g}/\text{cm}^3$ [95] and the density of Stellite 720 is $8.53 \text{ g}/\text{cm}^3$ [96]. The densities of modified Stellite 21 and nitrided Stellite 21 are unknown and can be approximately $8.33 \text{ g}/\text{cm}^3$ for this calculation.

$$EW = \frac{1}{\sum \frac{n_i f_i}{W_i}}, \quad (5.2)$$

where f_i = mass fraction of the i^{th} element in the alloy;

W_i = atomic weight of the i^{th} element in the alloy and;

n_i = valence of the i^{th} element of the alloy.

The value of EW is independent of the unit system chosen and so that it may be considered dimensionless. It should be noted that normally only the elements that are above 1 mass percent in the alloy are included in the calculation [101]. According to equation (5.1) and equation (5.2), the corrosion rates of the tested alloys were calculated and the results are presented in Figure 5-15. Modified Stellite 21 exhibited the lowest corrosion rate ($5.4 \times 10^{-4} \text{ mm}/\text{yr}$). The corrosion rate of nitrided Stellite 21 was $2.8 \times 10^{-3} \text{ mm}/\text{yr}$ which was the highest among the four tested alloys and was more than 5 times higher than that of modified Stellite 21. Stellite 21 showed a bit less material loss in corrosion than Stellite 720 in the long term prediction.

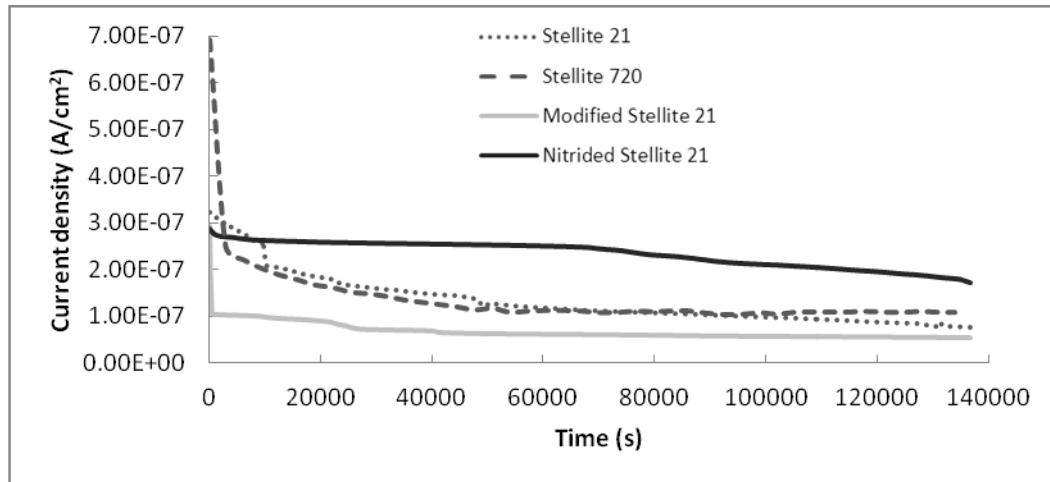


Figure 5-14: Current densities of the tested alloys at E_{corr} for 40 hr.

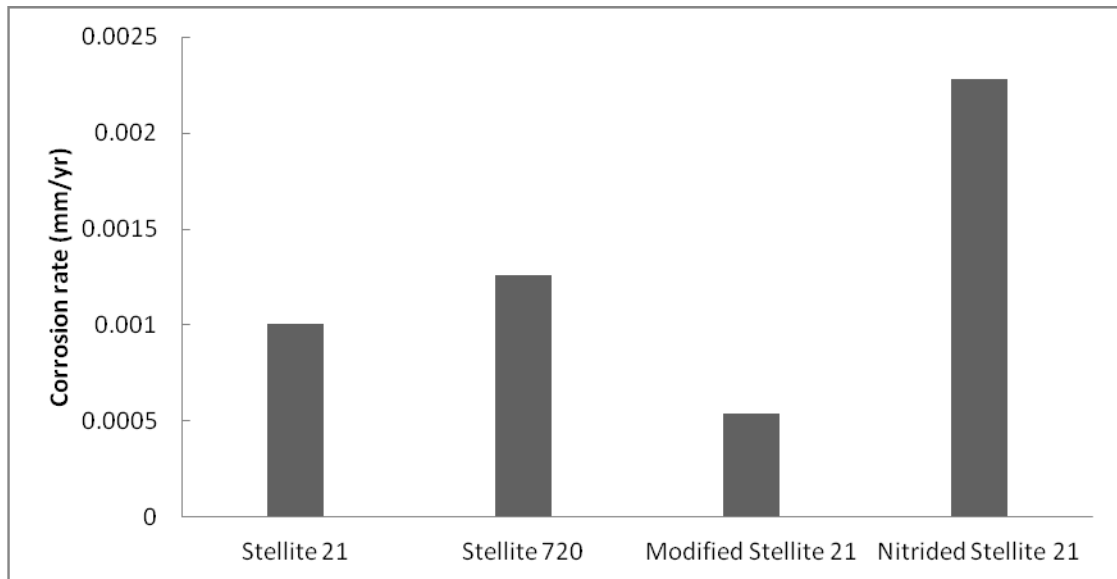


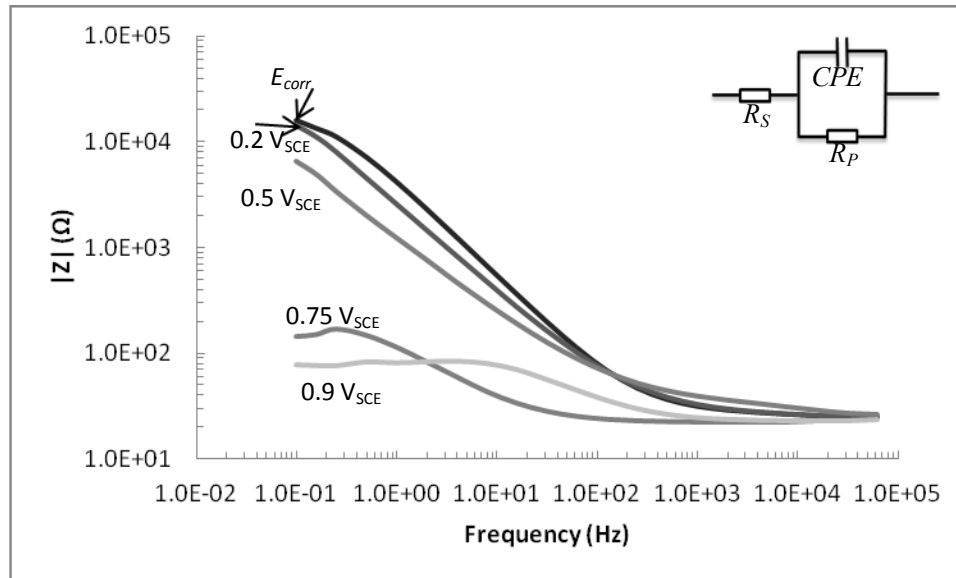
Figure 5-15: Calculated corrosion rates of the tested alloys.

5.3.4 EIS results

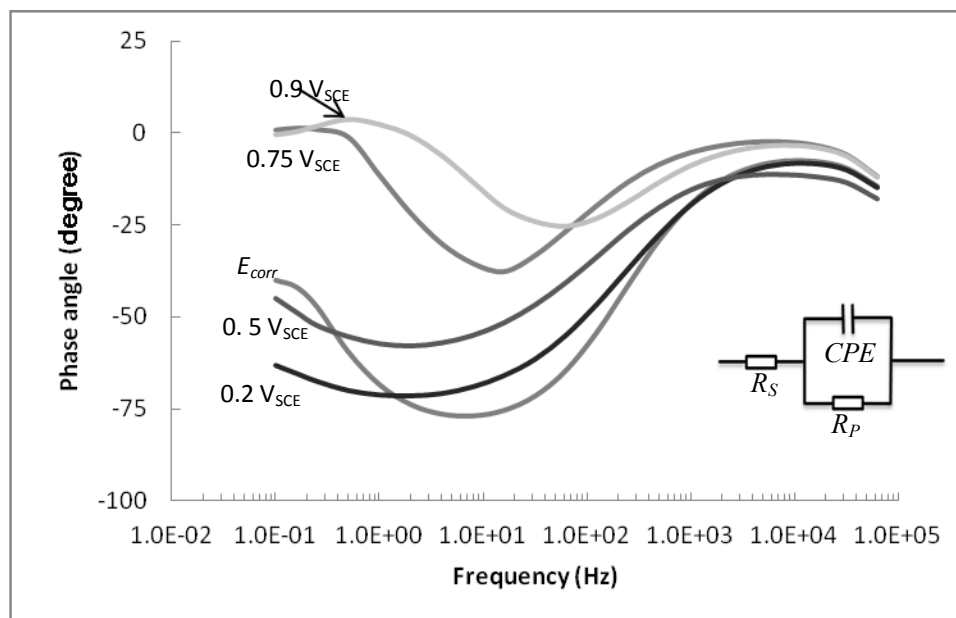
As described in Chapter 2, an equivalent Randles circuit can be fitted to the metal/electrolyte system for EIS data analysis. The constant phase element (CPE) is employed as an oxide film on the metal surface acting like a non-ideal capacitor. It can be seen from the EIS spectra in Bode plots for Stellite 21 in Figure 5-16 that, in the

high-frequency region from 1000 Hz to 10^5 Hz, the modulus of impedance, $|Z|$, was independent of the frequency with the phase angle θ approaching to zero. The impedance of the system was controlled by solution resistance, R_S , in this region. At the low frequency of 0.1 Hz, the impedance of the system was equal to the sum of solution resistance and polarization resistance, $R_S + R_P$. In the lower to intermediate frequency region (1-1000 Hz), the system was determined by the CPE (oxide film) characteristic with a slope close to -1.

From Figure 5-16, it is further confirmed that at the potentials of 0.75 V_{SCE} and 0.9 V_{SCE}, the metal surface was absolutely corroded with the R_P value of only 117 Ω and 54 Ω , respectively. The phase angles at these two potentials barely showed much capacitive effect and they turned out to be greater than zero at 1 Hz or less, indicating a pseudo-inductive effect and an actively corroding surface [91]. The EIS data of the other alloys at 0.75 V_{SCE} and 0.9 V_{SCE} are not presented here due to their similar behavior at these two potentials.



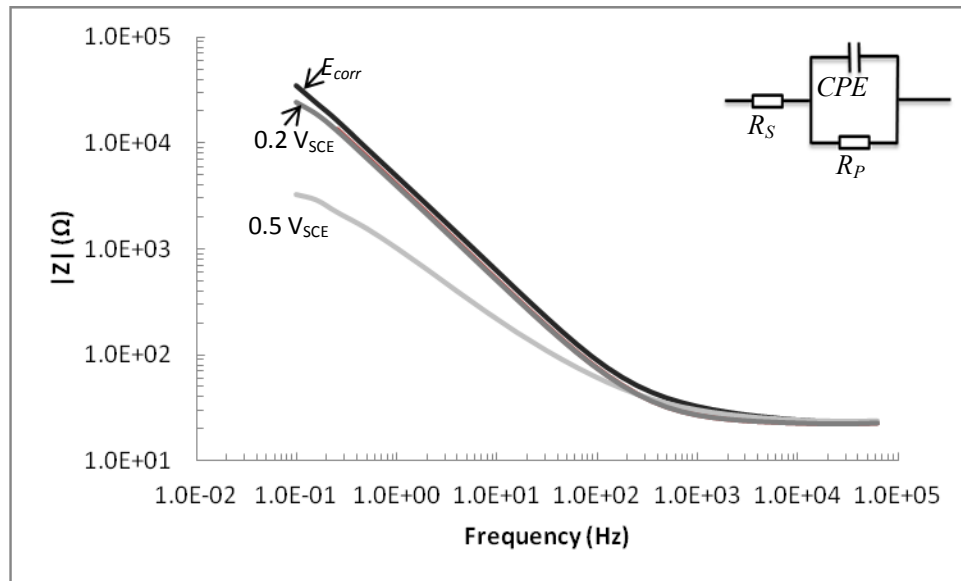
(a)



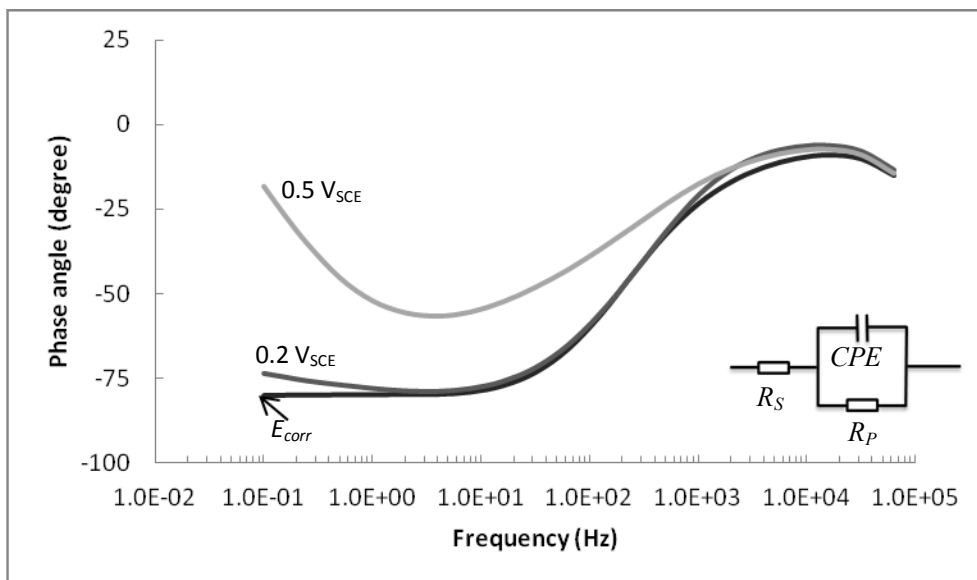
(b)

Figure 5-16: Electrochemical impedance spectra at E_{corr} , $0.2 V_{SCE}$, $0.5 V_{SCE}$, $0.75 V_{SCE}$ and $0.9 V_{SCE}$ for Stellite 21 in Hank's solution with pH 7.4 at 37°C: (a) Bode plots of impedance magnitude, and (b) Bode plots of phase angle. The equivalent circuit is attached to both diagrams.

The electrochemical impedance spectra for Stellite 720, modified Stellite 21 and nitrided Stellite 21 in Hank's solution with pH 7.4 at 37°C at the potentials of E_{corr} , 0.2 V_{SCE} and 0.5 V_{SCE} are presented from Figure 5-17 to Figure 5-19 with the equivalent circuit attached. Figure 5-20 summarizes the EIS data of all the alloys at E_{corr} for comparison.

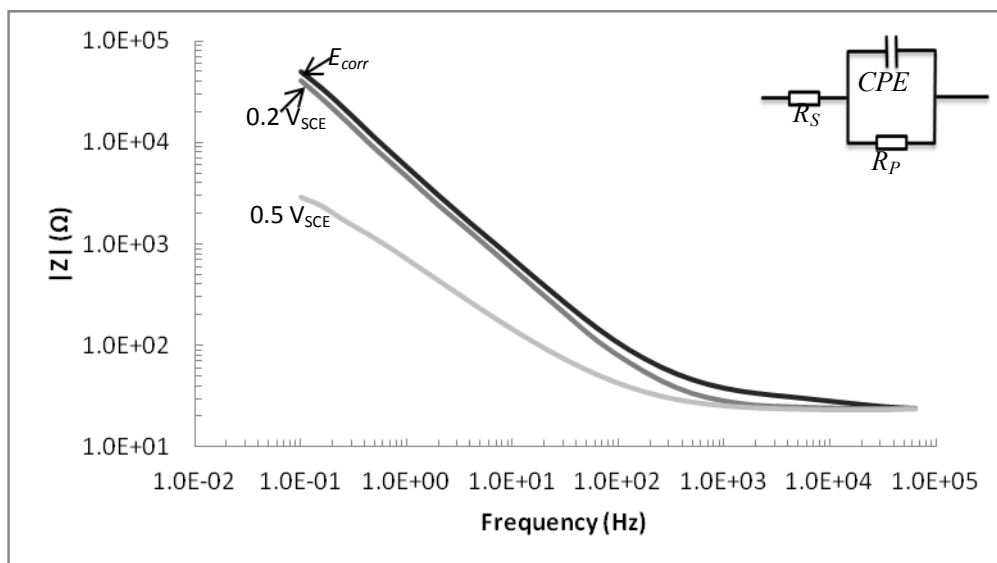


(a)

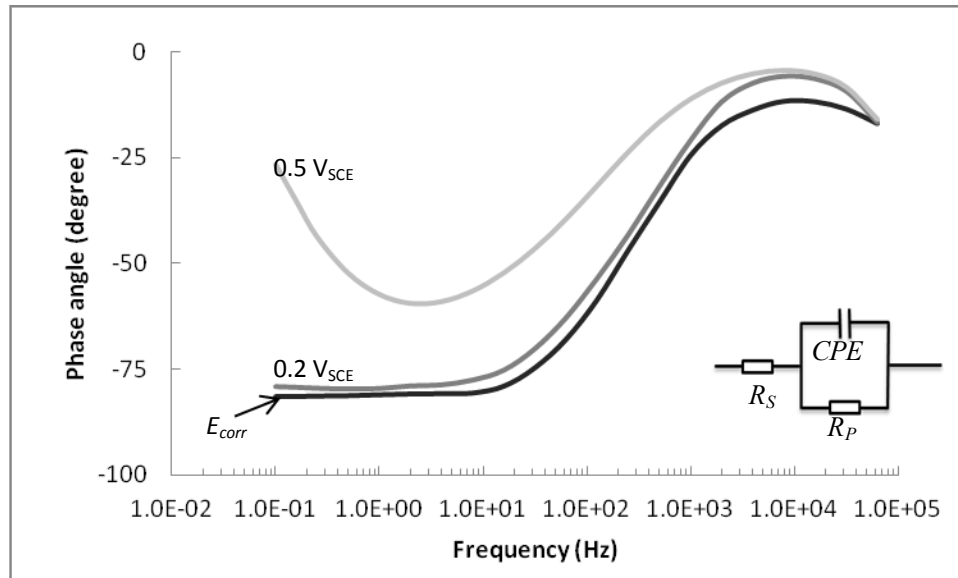


(b)

Figure 5-17: Electrochemical impedance spectra at E_{corr} , 0.2 V_{SCE}, and 0.5 V_{SCE} for Stellite 720 in Hank's solution with pH 7.4 at 37°C: (a) Bode plots of impedance magnitude, and (b) Bode plots of phase angle. The equivalent circuit is attached to both diagrams.

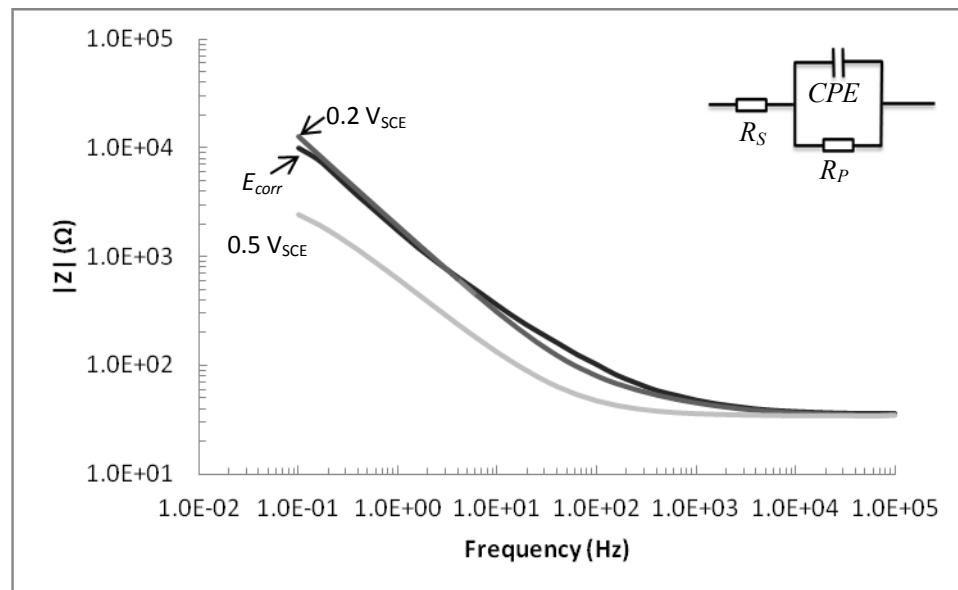


(a)

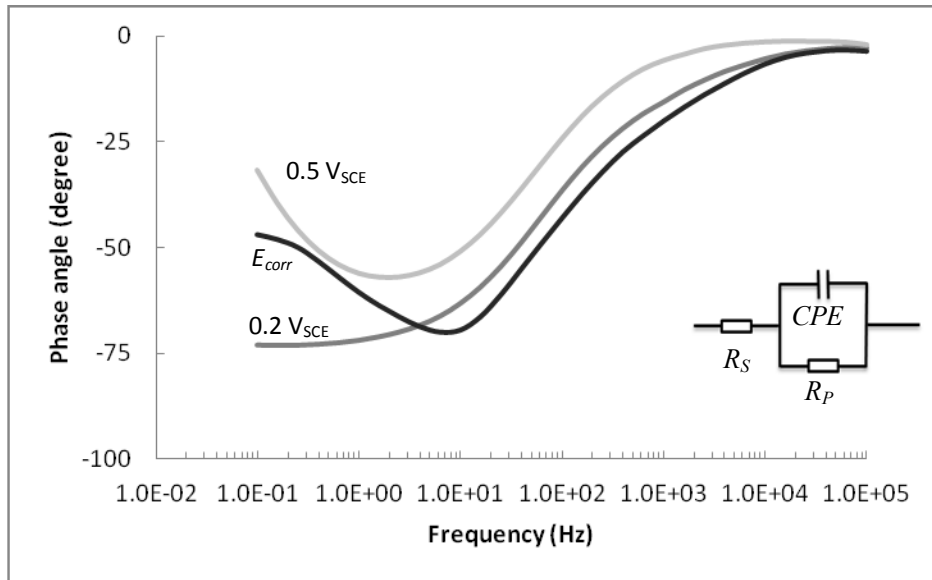


(b)

Figure 5-18: Electrochemical impedance spectra at E_{corr} , 0.2 V_{SCE}, and 0.5 V_{SCE} for modified Stellite 21 in Hank's solution with pH 7.4 at 37°C: (a) Bode plots of impedance magnitude, and (b) Bode plots of phase angle. The equivalent circuit is attached to both diagrams.

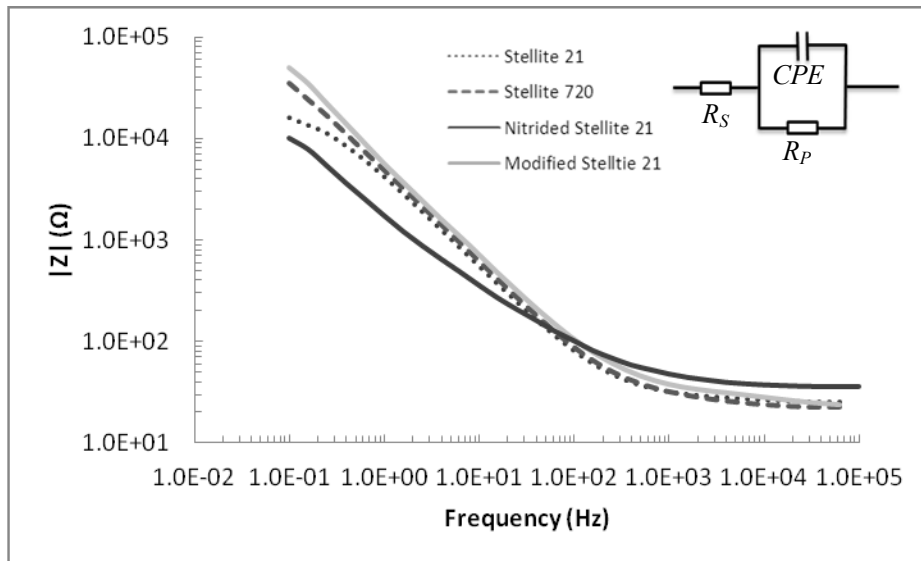


(a)

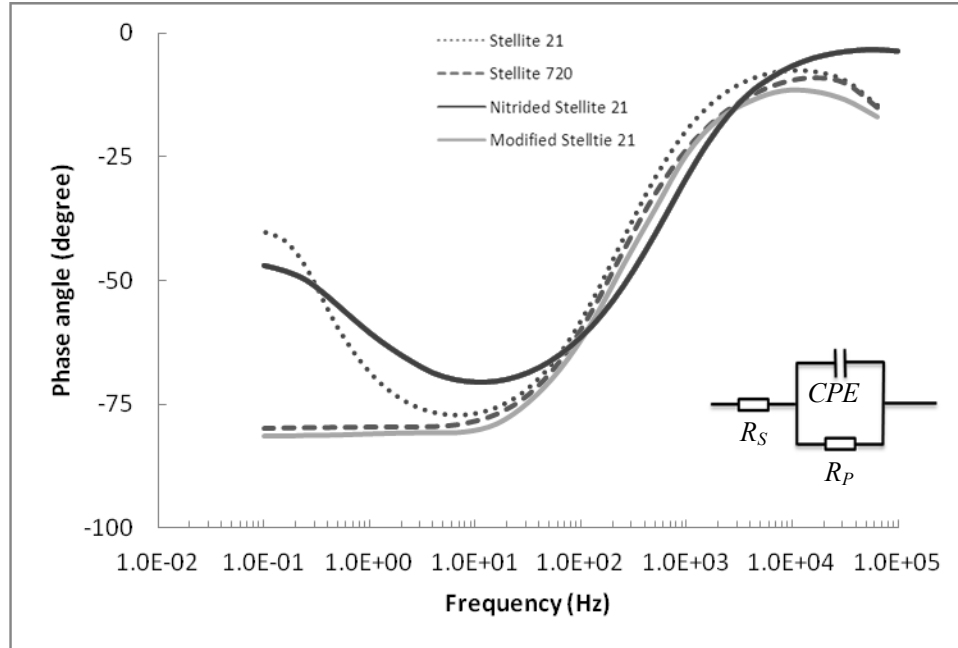


(b)

Figure 5-19: Electrochemical impedance spectra at E_{corr} , 0.2 V_{SCE}, and 0.5 V_{SCE} for nitrided Stellite 21 in Hank's solution with pH 7.4 at 37°C: (a) Bode plots of impedance magnitude, and (b) Bode plots of phase angle. The equivalent circuit is attached to both diagrams.



(a)



(b)

Figure 5-20: Electrochemical impedance spectra at E_{corr} for the tested alloys in Hank's solution with pH 7.4 at 37°C: (a) Bode plots of impedance magnitude, and (b) Bode plots of phase angle. The equivalent circuit is attached to both diagrams.

The values of R_S , R_P , Y_0 , and α for each alloy can be obtained based on the EIS spectra in Figure 5-16 to Figure 5-19. For each potential, one may select the part of $|Z| \sim f$ curve within medium frequency, which is approximately linear, and re-plot the curve with converting log-transformation for both $|Z|$ and f axes, then the absolute slope of the curve can be the α value. Then utilize the following expression [90]:

$$Y_0 = \frac{1}{|Z|(j\omega)^\alpha}, \quad (5.3)$$

where $j = \sqrt{-1}$, ω is the angular frequency ($\omega = 2\pi f$), the value of Y_0 can be obtained.

The values of R_S and R_P are determined according to the following equations [90]:

$$|Z|(\omega) = R_S, \text{ at high } f \quad (5.4)$$

$$|Z|(\omega) = R_S + R_P, \text{ at low } f \quad (5.5)$$

These values for different potentials are summarized in Table 5-3. For all of the EIS spectra, the fitting procedure resulted in a relatively independent α at E_{corr} and 0.2 V_{SCE}, ranging from 0.79 to 0.92, which justified the use of CPE. However, as the absence in the spectra of the low frequency resistive response, the accuracy in determining the R_P value was limited. It can also be seen that the R_S value remained almost constant (25 Ω ~ 35 Ω) and was independent of applied potential and frequency during the test, indicating a stable test environment.

Table 5-3: Values of equivalent circuit components.

Alloy	Potential (V _{SCE})	α	$Y_0 \times 10^{-6}$ ($\Omega^{-1} \text{ s}^{-n}$)	R_S (Ω)	R_P (k Ω)
Stellite 21	-0.336	0.884	46.69	25.056	15.9
	0.2	0.814	49.89	25.172	14.08
	0.5	0.7	224.3	26.286	6.5
Stellite 720	-0.142	0.886	40.1	22.902	35
	0.2	0.887	49	22.848	24.5
	0.5	0.672	284	23.604	3.26
Modified Stellite 21	-0.2218	0.921	28.6	23.884	50.1
	0.2	0.902	39.4	23.971	41
	0.5	0.701	220	23.407	2.89
Nitrided Stellite 21	-0.065	0.79	127.8	35.6691	10.08
	0.2	0.83	117	35.2651	12.6
	0.5	0.692	447	35.0423	2.44

It is known that when α equals 1, the CPE acts as a perfect capacitance. In this research, modified Stellite 21 had the highest α with a value of 0.921 at E_{corr} , indicating a very good oxide film formed on the surface. The values obtained for Stellite 720 and Stellite 21 were similar. Further results of CPE parameter Y_0 confirmed this prediction. According to equation (2.7), it can be assumed that [104]:

$$Y_0 = \frac{\varepsilon\varepsilon_0 A}{d}, \quad (5.6)$$

where ε is the relative dielectric constant of the oxide film, ε_0 is the absolute permittivity of the air/vacuum, with a constant value of 8.854×10^{-12} F/m, A is the exposure surface area and d is the thickness of oxide film.

Thus,

$$d = \frac{\varepsilon\varepsilon_0 A}{Y_0} \quad (5.7)$$

In this research, the surface area A equaled 0.785 cm^2 and the ε of the Cr_2O_3 was taken to be 12 [105]. The thickness d is therefore inversely proportional to Y_0 . Except for nitrided Stellite 21, Y_0 increased for the other alloys as the potentials stepped up to $0.5 \text{ V}_{\text{SCE}}$. The thickness of the oxide film for each of the alloys was calculated and the values are provided in Table 5-4.

According to the R_p values in Table 5-3 and Table 5-4, modified Stellite 21 had the best corrosion resistance among the four alloys because of the highest R_p value (50.1 k Ω) and the thickest oxide scale (2.92 nm) at E_{corr} , whereas nitrided Stellite 21 had the worst. These calculation results agree well with the cyclic polarization test results. In the cases of Stellite 21 and Stellite 720, the latter had slightly thicker oxide film and its R_p was approximately 20 k Ω greater than that of the former. However, at the potentials of 0.2 V_{SCE} and 0.5 V_{SCE} , the R_p value of Stellite 21 decreased at a lower rate and the oxide film remained thicker, indicating a slower corrosion process as time shifted. At 0.5 V_{SCE} , the oxide films on all the alloy surfaces were consumed and the thickness was reduced to less than 0.5 nm, which corroborated the theory of pitting potential.

Table 5-4: Cr₂O₃ film thickness values on specimen surfaces at selected potentials

Alloy \ d (nm)	At E_{corr}	At 0.2 V_{SCE}	At 0.5 V_{SCE}
Stellite 21	1.79	1.67	0.37
Stellite 720	2.07	1.07	0.29
Modified Stellite 21	2.92	2.12	0.38
Nitrided Stellite 21	0.65	0.71	0.19

5.4 Immersion test

5.4.1 Experimental details

Immersion test was conducted on the alloy specimens to investigate the element concentrations in the Hank's solution after each test thus to further understand the corrosion behavior of these alloys in the solution. The round plate specimens with polished surfaces were immersed in 20 ml Hank's solution in conical tubes. The tubes

were then put in a water bath (Anova Inc.) that was filled with tap water. The test environment was set at a constant temperature of 37°C, as shown in Figure 5-21. Before the test, the 20 ml Hank's solution was deaerated with pure argon gas. The specimens were immersed for 1 day, 2 days, 5 days and 10 days, respectively. In each test condition, two specimens of each alloy were investigated. After the immersion test for a set time, the specimens were removed from the solution and placed in tight-sealed vials. In the meantime, 10 ml of each tested solution, as sample solution, was taken for inductively couple plasma optical emission spectroscopy (ICP-OES) analysis. This technique can detect the released ion concentrations within the solution. The equipment used in this research is an Agilent Vista Pro ICP-OES instrument, as shown in Figure 5-22.



Figure 5-21: Immersion test set-up.

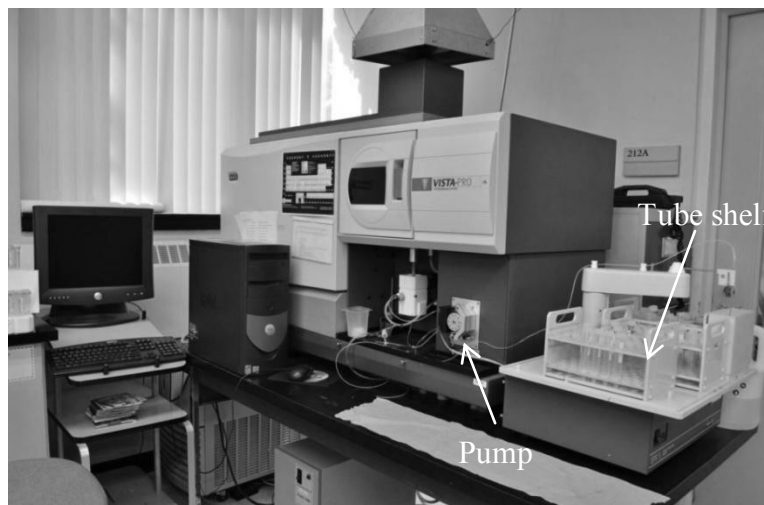
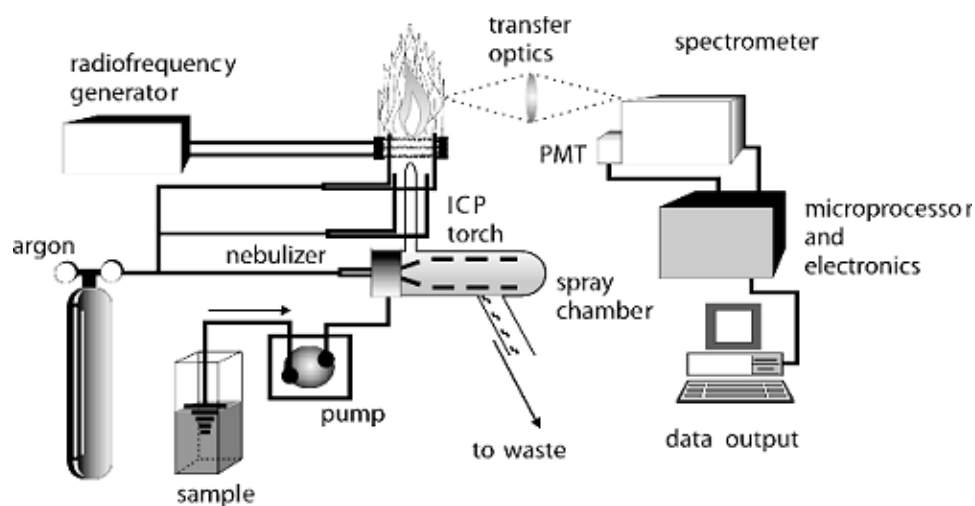


Figure 5-22: The Agilent Vista Pro ICP-OES instrument.

Before the sample solution was put in the instrument, it was acidified with concentrated HNO_3 using a micropipette (Fisher Scientific). The purpose of acidifying was to make sure that the metallic ions stayed in the solution instead of being on the wall of the containers. The amount of the concentrated HNO_3 was recommended to be 2 vol% of each sample solution, which was about 0.2 ml. The tube containers were shaken to ensure homogeneous solution after acidification. The tubes were then placed on a shelf, as shown in Figure 5-22.

As shown in Figure 5-23, the ICP-OES system consists of two parts: ICP torch and optical spectrometer. The sample solution is pumped to the nebulizer. At the same time, the argon gas joins in the nebulizer with the solution, converting to aerosol, which is also called sample carrier gas. The nebulizer is connected to the spray chamber where big droplets of aerosol are eliminated as wasted and fine droplets are sprayed to the ICP torch as the analytical aerosol. The ICP torch consists of three concentric quartz glass tubes. The radio frequency (RF) generator creates high power RF signal (27 MHz) flowing into

the coil which surrounds the tube. The aerosol, plasma argon gas and auxiliary/intermediate argon gas flow to the top of the tube, forming the torch. When the torch is turned on, an intense electromagnetic field is created within the coil. The highest temperature of the flame can be 10,000°C while the normal flame temperature can only reach 2000 - 3000°C. After the argon gas and aerosol are ignited, various molecules break up into their respective atoms, which then lose electrons and recombine repeatedly in the plasma, giving off radiation at the characteristic wavelengths of the elements involved. Within the optical chamber, after the light is separated into its different wavelengths $\lambda_1\lambda_2\lambda_3\dots$, the separated colors of different light intensities fall upon an array of semiconductor photo detectors such as charge coupled devices (CCDs). The intensities of all wavelengths (within the system's range) can be measured simultaneously, allowing the instrument to analyze for every element to which the unit is sensitive all at once. The intensity of each line is then compared to previously measured intensities of known concentrations of the elements, and their concentrations are then computed by interpolation along the calibration lines [106].



(a)

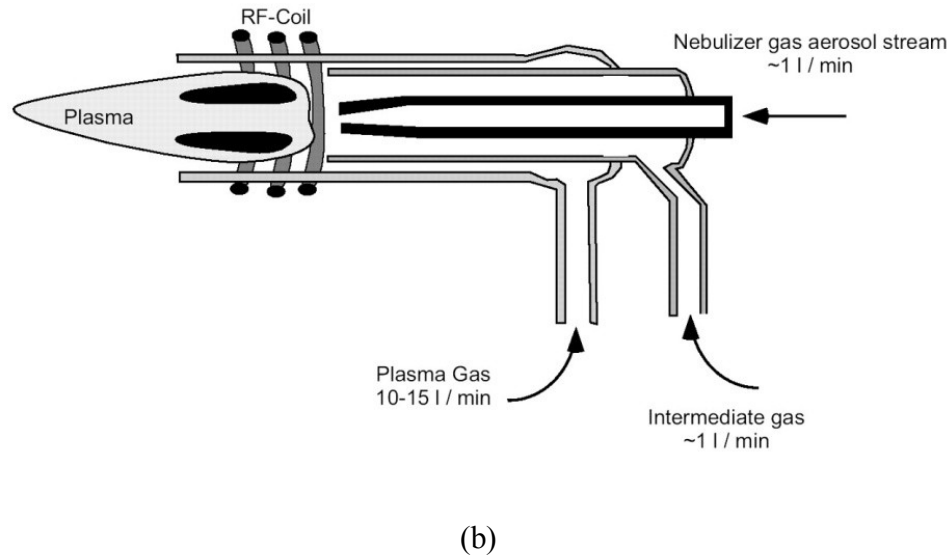


Figure 5-23: ICP-OES system: (a) a schematic diagram of ICP-OES setup, and (b) a schematic diagram of the ICP torch [107, 108].

5.4.2 Element concentration results and analysis

The concentrations of Co, Cr, Ni and Mo ions in the solutions where the alloy specimens experienced the immersion tests were of interest in this research because of their possible side effects on the human body cells, as discussed in Chapter 2. Low ion release of the alloy implies its better corrosion resistance performance in the solution. The results obtained from the ICP-OES analysis are presented in Figure 5-24 to Figure 5-27. The data reported were the mean values of the two specimens for each alloy. The concentrations of the released ions were originally given in the unit of ppb (part per billion) and were then converted to the unit of $\mu\text{g/L}$. As Hank's solution is hypotonic, the density of the solution is taken as 1 g/ml when converting the data.

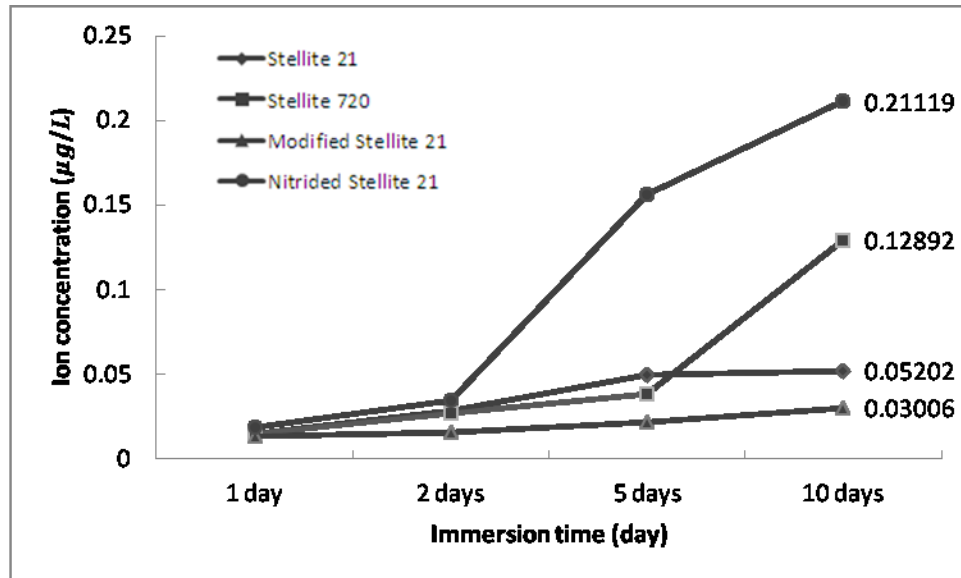


Figure 5-24: Cobalt ion concentrations in sample solution for the Stellite alloys after immersion tests.

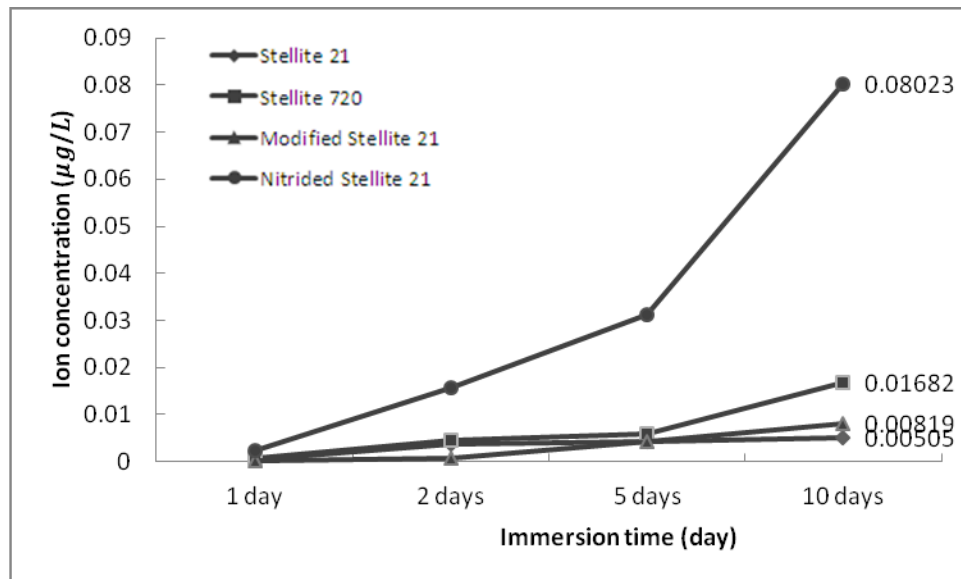


Figure 5-25: Chromium ion concentrations in sample solution after immersion tests of the Stellite alloys.

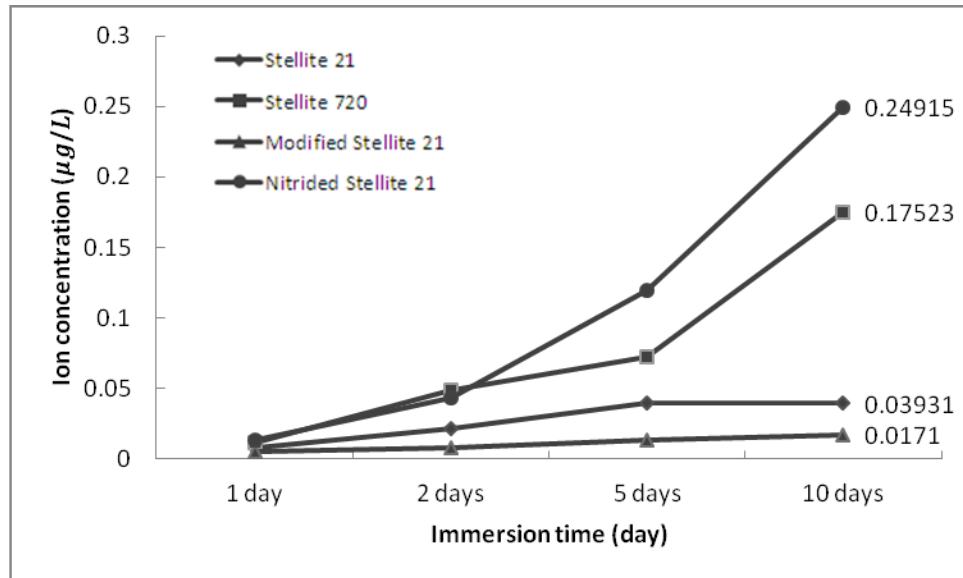


Figure 5-26: Molybdenum ion concentrations in sample solution after immersion tests the Stellite alloys.

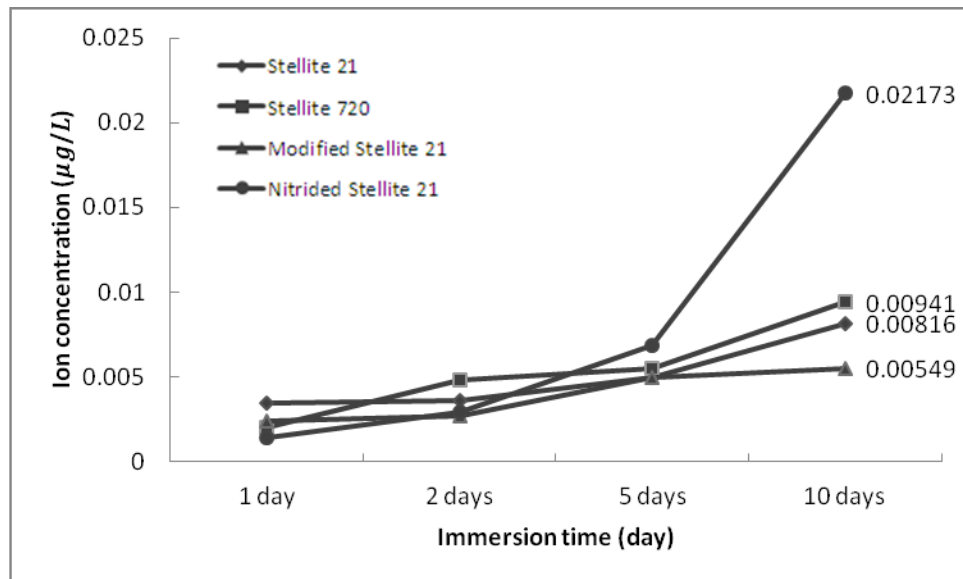


Figure 5-27: Nickel ion concentrations in sample solution after immersion tests of the Stellite alloys.

For the Co ion release, as shown in Figure 5-24, there was no much difference in concentration value between the alloys after the first day immersion, with the highest concentration value of 0.019 $\mu\text{g/L}$ for nitrided Stellite 21 and the lowest of 0.0134 $\mu\text{g/L}$

for modified Stellite 21. The Co ion release of nitrided Stellite 21 increased at the highest rate and the ion concentration reached about $0.21\mu\text{g/L}$ after 10 day immersion test, which was more than 20 times larger than that after 1 day immersion test. The concentrations of released Co ion in the solution for Stellite 21 and Stellite 720 after 1, 2, and 5 day immersion tests increased slightly and also little difference between these two alloys was observed. However, between 5 day and 10 day immersion tests, a significant increase in Co ion concentration was found on Stellite 720, with accumulated concentration amount of $0.09\mu\text{g/L}$, whereas only $0.003\mu\text{g/L}$ of Co ion was released from Stellite 21. Modified Stellite 21 exhibited the least ion release throughout the test duration time.

In regard to the Cr ion concentration, as shown in Figure 5-25, for all the alloys the concentration levels were 10 ~ 20 times lower than those of the Co concentration. Again, the Cr concentration in sample solution was the highest for nitrided Stellite 21, with the value of $0.08\mu\text{g/L}$ after 10 day immersion test. The increase rates of the Cr concentration of Stellite 21 and modified Stellite 21 were lower as time shifted, with the values of $0.008\mu\text{g/L}$ and $0.005\mu\text{g/L}$, respectively. The Cr concentration of Stellite 720 was similar to that of Stellite 21 and modified Stellite 21 in 1 day, 2 day, and 5 day immersion tests. However, a significant release of Cr ion from this alloy was found in the 5 to 10 day immersion tests and the concentration reached $0.0169\mu\text{g/L}$ after 10 day immersion test.

The Mo ion release for the alloys was similar to the Co ion release, as shown in Figure 5-26. The values were 0.039 $\mu\text{g/L}$, 0.175 $\mu\text{g/L}$, 0.017 $\mu\text{g/L}$, and 0.249 $\mu\text{g/L}$ for Stellite 21, Stellite 720, modified Stellite 21, and nitrided Stellite 21, respectively, after 10 day immersion test. Notably, the Mo level in the solution of Stellite 720 was higher than that in the solution used for Stellite 21 throughout the test duration.

The Ni ion concentration, as shown in Figure 5-27, was relatively low when compared with the other elements, which may be attributed to its low content in the alloys. The solution used for nitrided Stellite 21 exhibited the highest Ni ion release rate, reaching an ion concentration value of 0.021 $\mu\text{g/L}$. The Ni ion concentrations in the solutions for other three alloys were less than 0.01 $\mu\text{g/L}$ after 10 day immersion test.

The ion concentrations in sample solutions after 10 day immersion test for the four alloys are summarized in Figure 5-28.

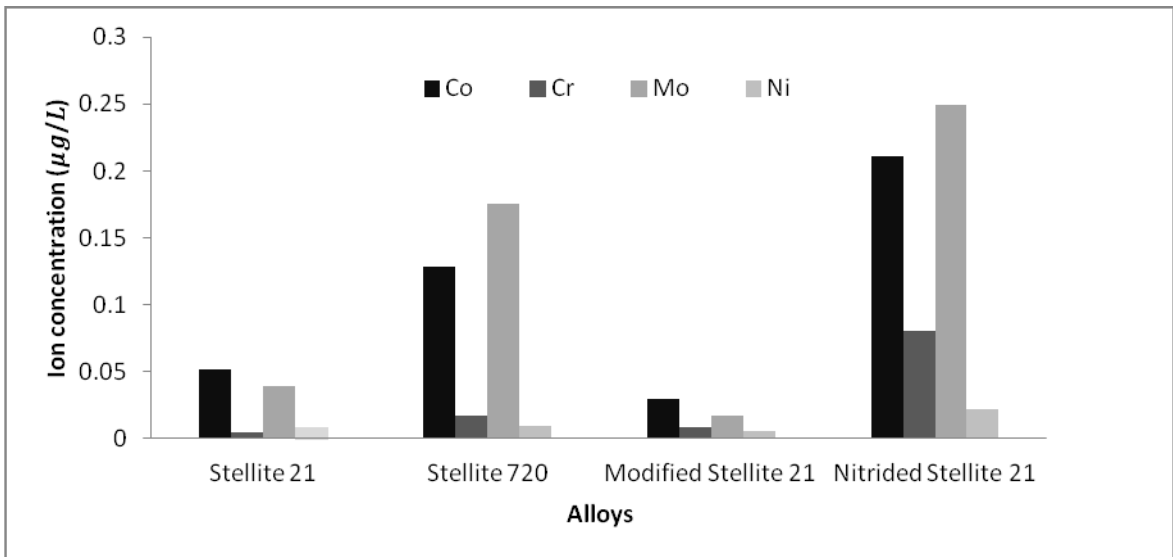


Figure 5-28: Ion concentrations in sample solutions for the Stellite alloys after 10 day immersion tests.

6 Chapter: Discussion on Results and Correlations

This chapter provides the discussion on the experimental results, focussing on the effects of chemical composition and manufacturing process on the microstructure, wear and corrosion behaviour of the Stellite alloys in the designated test conditions. The correlations among these results are analyzed and reported.

6.1 Effects of chemical composition and manufacturing process on microstructure

As potential hip implant materials for improving the MOM bearing performance, cast Stellite 720, HIPed modified Stellite 21 with addition of 10 wt%Cr and HIPed nitrided Stellite 21 with addition of 0.4 ~ 0.6 wt%CrN were studied in this research with respect to wear and corrosion resistance. Cast Stellite 21, which is a conventional orthopedic implant material, was also investigated as a reference material. As analyzed in Chapter 3, the four alloys bear different microstructure morphologies due to various chemical compositions and manufacturing processes. Since the test parameters of wear and corrosion resistance on these alloys are the same, it is believed that chemical composition and manufacturing process are the dominant causes for the difference in microstructure among the alloys.

As shown in Table 3-1, Stellite 720 contains very high C content (2.5 wt%) and higher Cr and Mo contents so that it has a large volume fraction of carbides. The volume fraction of carbides in Stellite 720 was estimated using the associated software with the SEM system. The SEM image with identified carbide phase is shown in Figure 6-1. Two specimens of this alloy were examined and the average carbide volume fraction in Stellite

720 is about 35.5%, whereas the volume fraction of carbides in Stellite 21 is only about 4% [57] as it contains a very low C content (0.25 wt%). Also, the high C content in Stellite 720 induces the primary Cr_7C_3 , while the low C content in Stellite 21 forms the eutectic Cr_{23}C_6 .

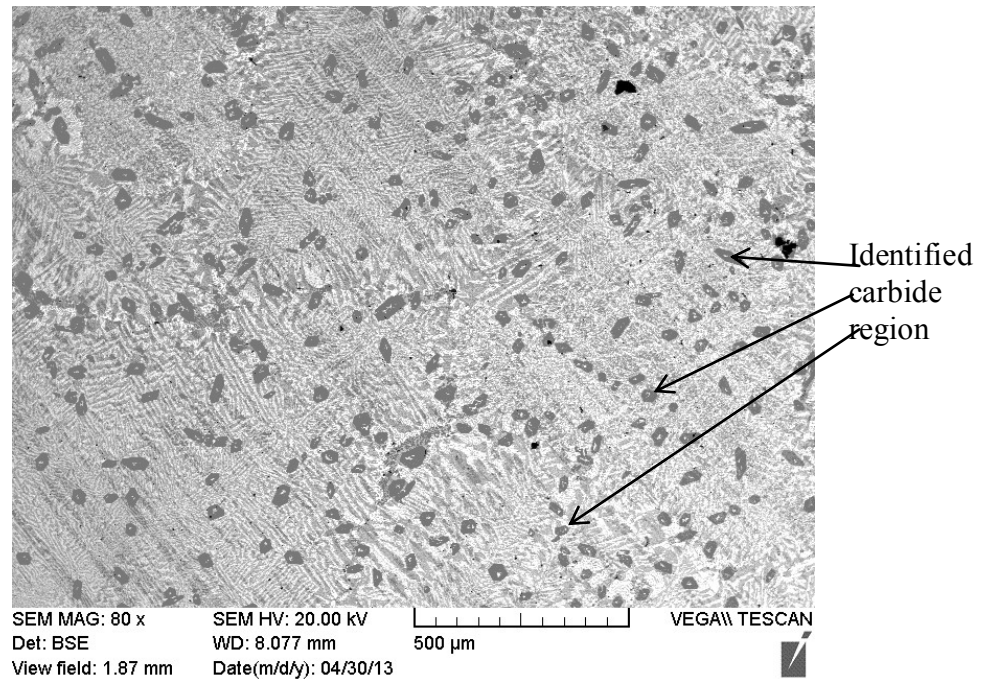


Figure 6-1: SEM image of identified carbide region in Stellite 720.

Comparing the microstructures in Figure 3-2, Figure 3-6 and Figure 3-8, it can be seen that modified Stellite 21 and nitrided Stellite 21 have the same phases (Co solid solution phase + eutectic phase) as Stellite 21, which is due to the similar chemical compositions. The increased Cr content in modified Stellite should be added in the solid solution phase but not induce additional carbides due to the limited C content. As observed in the images, the microstructure morphologies of these alloys are slightly different. The carbides in modified Stellite 21 and nitrided Stellite 21 are smaller or finer and their shape is also different from that of the carbides in Stellite 21. This may be caused by the

different manufacturing processes. As concerns addition of CrN into Stellite 21, it is found that in addition to Cr_{23}C_6 carbide the presence of N induced the C-rich microdroplets, as seen in Figure 3-8. As discussed earlier, the microdroplets may also contain minor CrN and Mo-rich nitride, but the EDX analysis could not identify N element existence due to the very small content. Addition of CrN into Stellite 21 can enhance the hardness of the alloy [109] and the presence of CrN in the alloy can promote the dissolution of C [77] thus to diffuse into the nitrides. Since the melting point of CrN is much higher than the HIPing temperature, CrN may still be in solidus state during the HIPing process of alloy fabrication [110, 111]. However, dissolution of CrN possibly occurred at the high temperature, which invoked formation of the C-rich microdroplets that may also contain various nitrides.

6.2 Effects of microstructure on wear behavior

The pin-on-disc wear test results in Figure 4-6 demonstrate that the wear resistance of the Stellite alloys is governed by their carbide volume fraction and the solid solution strengthening also plays an important role. Stellite 720 has the largest volume fraction of carbides, accordingly, it exhibited the best wear resistance. On the contrary, Stellite 21 has the least volume fraction of carbides so that it displayed the worst wear resistance. Among Stellite 21, modified Stellite 21 and nitride Stellite 21, although they contain the same C content, the additive Cr in modified Stellite 21 strengthens its solid solution matrix, which enhanced its wear resistance. The addition of CrN into Stellite 21 induced the C-rich microdroplets, which benefited the wear resistance of the alloy.

Moreover, it is widely accepted that the hardness property is a critical indicator when selecting a material for a designated application because it is closely associated with ductility, elasticity, toughness and strength properties of materials. It is commonly agreed that for most materials, the harder the material, the greater the wear resistance. To verify this relation on these Stellite alloys, microhardness indentation test was conducted on them using a Microhardness Tester Unit, Model SMT-X7 Dual Indenter. The measurement was tried to make on each individual phase of the microstructures. However, due to the very small sizes of carbides in the Stellite 21 group, the indentation could not be made on the single carbide phase even with a very low load applied. Therefore, the hardness discussed here among the Stellite 21 group is of the solid solution only. As the size of the primary Cr_7C_3 carbide in Stellite 720 is large enough for the indentation, the carbide hardness for this alloy is available. The indentation test results are illustrated in Figure 6-2.

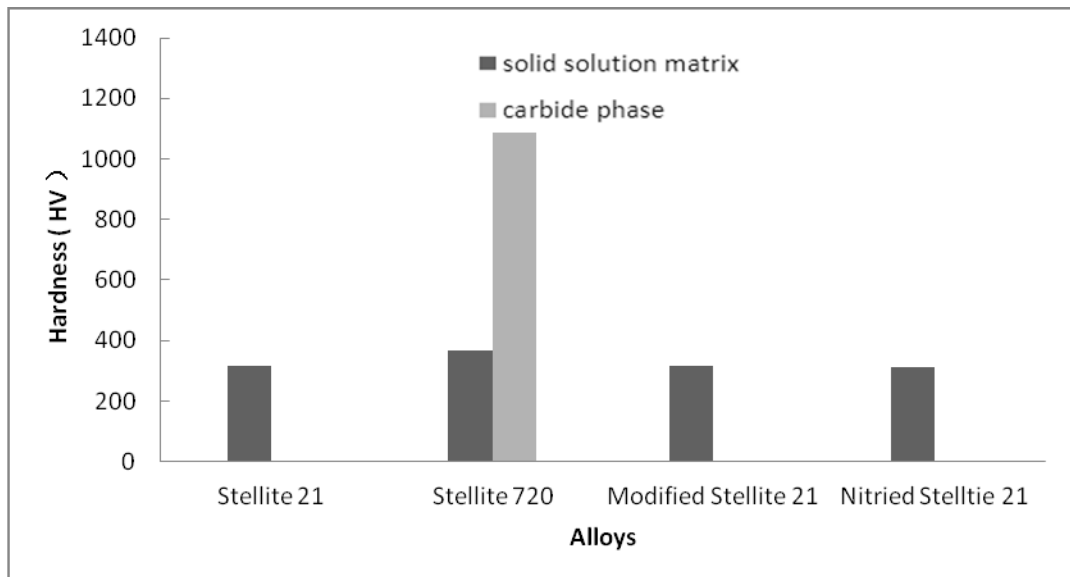


Figure 6-2: Microhardness test results of the Stellite alloys.

It is shown that the hardness of the solid solution matrix of Stellite 720 was approximately 50 HV higher than that of Stellite 21. The higher Cr and Mo contents, which strengthen the solution matrix, and the eutectic $(\text{Mo,Co})_6\text{C}$ or $(\text{Mo,Co})_2\text{C}$ precipitates may all be responsible for the higher hardness. The carbide is much higher than the solid solutions, as seen in Figure 6-2. The hardness of carbide Cr_7C_3 was about 3.5 times higher than that of the solid solution of Stellite 720, which greatly contributed to the overall hardness of the alloy.

For the Stellite 21 group, the hardness of solid solution of the three alloys was very close, which implies that the manufacturing or fabrication process of the alloys did not affect the hardness very much. However, as well known, HIPing is a manifest stress-enhanced process, the bonding between solid solution matrix and carbide phase in the HIPed alloys may be strengthened [112]. Thus, during the wear process, the strengthened bonding prevented the carbides from spalling off, thus achieving better wear performance. For nitrided Stellite 21, although the presence of CrN was unable to be detected by the EDX analysis, it was assumed to exist. The CrN particle has a hardness value about 2740 HV [113], therefore it also contributed to the increased wear resistance, compared to Stellite 21. However, since the amount of CrN in the alloy is too small, its beneficial effect on the hardness cannot be identified by the hardness tests.

6.3 Effects of microstructure on corrosion behavior

The results of cyclic polarization, potentiostatic and EIS tests, as well as immersion tests in Chapter 5 show that modified Stellite 21 exhibited the best corrosion resistance in

Hank's solution while nitrided Stellite 21 the worst among the four alloys in all the corrosion tests. Between the high-carbon Stellite 720 and the low-carbon Stellite 21, the former displayed better corrosion resistance at the initial testing period but with time shifting it was more rapidly corroded with a larger amount of Co ion and Cr ion released.

Comparing the chemical compositions between Stellite 21 and Stellite 720, this observation can be explained. When immersed in Hank's solution, Stellite 720 would form thicker protective Cr_2O_3 film on the specimen surface due to its higher Cr content. In the meantime, Stellite 720 contains very high C content, resulting in two distinct regions with Cr content: Cr-rich carbide and Cr-depleted surrounding solid solution zone. The larger volume fraction of carbides in Stellite 720 can induce more severe galvanic corrosion between the primary carbide phase and the solid solution phase where the Cr_7C_3 carbide acted as the cathode in the electrochemical reaction and the surrounding solution matrix performed as the anode. The more carbides the alloy has, the more sites for electrochemical battery the alloy produces. On the contrary, Stellite 21 contains a very small amount of C so that the microstructure appears to be an entire solid solution matrix and have fewer galvanic sites. Therefore, the overall corrosion loss of Stellite 21 was less in the long run of the test.

For modified Stellite 21, addition of Cr enhanced the formation of oxide film, which would produce a thicker Cr_2O_3 layer on the alloy surface. The thicker oxide layer should perform better capacitance behavior and therefore would decrease corrosion current and corrosion rate. Furthermore, compared with cast satellite 21, the HIPing process

provided modified Stellite 21 with smaller size carbides, which also benefited corrosion resistance due to smaller galvanic areas.

In the case of nitrided Stellite 21, the largest current density in the polarization and potentiostatic tests, the thinnest oxide layer in the EIS results and the highest levels of ions release in the immersion tests may be caused by the microdroplets formed due to the addition of CrN. The microdroplets created additional sites for electrochemical battery in Hank's solution thus resulted in more corrosion damage. In addition, the worst corrosion resistance of this alloy could also be attributed to the stronger affinity of CrN to chromium than to Co, which led to a partial weakening of original chemical bonding within the alloy [114].

6.4 Correlations among various factors

The objectives of this research were to explore new alloys which display improved MOM bearing for hip implants and also to test their corrosion resistance in human body fluid environment. Based on the experimental results in Chapter 4 and Chapter 5, the wear and corrosion behavior of the four alloys are summarized in Table 6-1.

From the experimental results obtained, Stellite 720, modified Stellite 21 and nitrided Stellite 21 all had better wear resistance than the conventional hip implant material, Stellite 21. In particular, Stellite 720 and nitrided Stellite 21 had about twice higher wear resistance than Stellite 21. This means that these alloys are superior to the existing hip implant material, Stellite 21, in consideration of the MOM bearing property.

Regarding corrosion resistance, modified Stellite 21 was much better than Stellite 21 whether in the aspect of corrosion loss, or in that of oxide film thickness or in that of element ion concentrations. The higher Cr concentration for modified Stellite 21 may be attributed to the 10 wt% higher Cr content. When the thicker Cr₂O₃ layer broke in the corrosive environment, the oxide debris in the solution would be more. For the other two alloys, Stellite 720 and nitrided Stellite 21, although their corrosion resistance is worse than Stellite 21, the corrosion losses of these alloys in the solution are still very small, in consideration for orthopedic implants.

Integrating the results of microstructure, wear tests and corrosion tests, it can be concluded that improved MOM bearing can be achieved by introducing additional carbides (Stellite 720), but more carbides would generate more sites for electrochemical battery in Hank's solution thus leading to more corrosion loss. It is very often that improvement in one attribute is accomplished at the expense of other desirable properties of materials. For example, improving wear resistance of materials often results in reduced toughness, weldability and corrosion resistance [115]. Therefore, a balance among various properties for a material should be concerned when it is selected for a designated application that involves a complex working environment such as high temperature, high stress, wear and corrosion, otherwise one property will be prior to the others in consideration for a material having a given application. Based on this discussion, for hip implant application, the results from this research demonstrate that modified Stellite 21 is the best candidate to replace Stellite 21 as a novel hip implant material, because it has superior both wear and corrosion resistance to Stellite 21 as a

result of Cr addition, rather than increasing wear resistance by introducing carbides that worsen corrosion resistance.

Table 6-1: Wear and corrosion results of the test alloys.

Alloy	Wear loss (mm ³)	Corrosion loss (mm/yr)	Oxide thickness (nm)	Co ion concentration (µg/L)	Cr ion concentration (µg/L)
Stellite 21	1.21	1.0×10^{-3}	1.79	0.052	0.005
Stellite 720	0.54	1.1×10^{-3}	2.07	0.129	0.017
Modified Stellite 21	0.89	5.4×10^{-4}	2.92	0.03	0.0082
Nitrided Stellite 21	0.63	2.8×10^{-3}	0.65	0.211	0.08

7 Chapter: Conclusions and Future Work

This chapter summarizes this research, including the conclusions drawn from this research, the limitation of this research and the future work towards to the goals of the entire project.

7.1 Summary of the research

In this research, the wear and corrosion behavior of three advanced Stellite alloys, as potential materials for hip implant application, along with the conventional hip implant material, Stellite 21, for comparison or reference, were investigated under the conditions simulating the real operating environment in human body. Dry sliding wear test was conducted on a pin-on-disc tribometer at room temperature. Corrosion tests were performed in Hank's solution whose chemical composition is similar to human body fluid, with pH value of 7.4 at the temperature of 37°C, including the electrochemical tests (open circuit potential, cyclic polarization, potentiostatic and EIS tests) and immersion test. The following conclusions can be drawn from the experimental results and associated analyses and discussion:

1. The proposed three Stellite alloys, Stellite 720, modified Stellite 21 with addition of 10 wt%Cr and nitrided Stellite 21 with addition of 0.4 ~ 0.6 wt%CrN all exhibited better wear resistance than the conventional hip implant material, Stellite 21. The excellent wear resistance of Stellite 720 was attributed to the large volume fraction of carbides and the enhanced wear resistance of nitrided Stellite 21 came from the formation of C-rich microdroplets which was induced by the presence of CrN. On

- the contrary, the increased wear resistance of modified Stellite 21 was a result of the solid solution strengthening by the additional Cr content.
2. Modified Stellite 21 exhibited the best corrosion resistance under the electrochemical tests and immersion test in Hank's solution among the alloys. This can be attributed to the high Cr content thus thicker Cr_2O_3 protective film. Owing to the high Cr content, Stellite 720 exhibited better corrosion resistance than Stellite 21 in the initial testing period because of the better Cr_2O_3 protective film. However, due to the presence of the large amount of carbides which generated more sites for electrochemical battery thus expedited the corrosion of the Cr-depleted solid solution surrounding the carbides. Nitrided Stellite 21 exhibited the worst corrosion resistance in the electrochemical and immersion tests among the alloys under study. The main reasons for this can be two: relatively low Cr content compared with Stellite 720 and modified Stellite 21 and the formation of C-rich microdroplets which have the same effect as carbides in electrochemical reaction during the corrosion process.
 3. The wear and corrosion resistance of the Stellite alloys strongly depend on their microstructures. The volume fraction of carbides present in the alloys dominates their wear resistance, while the solid solution strengthening also plays an important role. Moreover, manufacturing process of the alloys can influence their microstructures significantly. For the alloys studied in this research, the HIPed modified Stellite 21 and nitrided Stellite 21 specimens had a more homogenous microstructure with finer carbides, which contributed to the better wear resistance than cast Stellite 21.

4. Improved MOM bearing performance has been achieved by the three proposed alloys. However, as commonly known, improvement in one attribute is usually accomplished at the expense of other desirable properties of materials. Stellite 720 and nitrided Stellite 21 exhibited much better wear resistance than Stellite 21, but they were worse than Stellite 21 in corrosion resistance in Hank's solution. In consideration of both wear and corrosion resistance, modified Stellite 21 with addition of 10 wt%Cr is the best candidate of new material for hip implant application.

7.2 Limitation of this research

As hip implant materials, in addition to wear and corrosion resistance, other material properties, such as tensile strength, fatigue life and fracture toughness and so on, are also important. Due to lack of time and testing facilities, these properties were not considered in this research. Therefore, the recommendation of the alloys for potential hip implant materials was only based on the wear and corrosion tests performed in this research.

7.3 Future work

The following tasks are recommended for future work to further investigate and explore advanced Stellite alloys for hip implant application.

1. Biocompatibility is also an important property for orthopedic implant materials. Biocompatibility testing consists of three tests: cytotoxicity, sensitization, and irritation. Each test screens for the presence of toxic, leachable materials. For the three proposed alloys in this research, biocompatibility testing will be conducted.

2. The proposed new alloys will be eventually applied on hip implants as surface coatings. Various coating specimens such as thermal plasma spray coating using a Mettech Axial III™ System and slurry sintering coating have been obtained. The next task will be characterization of these coatings under various tests including microstructure, wear and corrosion resistance, as well as biocompatibility.
3. The improved MOM bearing of Stellite alloys can be achieved by increasing carbide volume fraction, but can also be gained by introducing intermetallic compounds. Thus Stellite 22 and Stellite 28 may be considered as another group of candidate materials for orthopedic implants. The similar experiments on these alloys will be performed.

References

- [1] F. Higuchi et al., "Metal-on-metal CoCrMo McKee-Farrar total hip arthroplasty: Characteristics from a long-term follow-up study," *Arch. Orthop. Trauma. Surg.*, vol. 116, no. 3, pp. 121-124, 1997.
- [2] C.B. Rieker et al., "Clinical wear performance of metal-on-metal hip arthroplasties," in *Alternative Bearings Surfaces in Total Joint Replacement, ASTM STP*, J.J. Jacobs and T.L. Craig, Eds., ASTM Soc. for Testing and Mater., 1998, pp. 144-155.
- [3] W. Brodner et al., "Elevated serum cobalt with metal-on-metal articulating surfaces," *J. Bone Joint Surg.*, vol. 79, no. 2, pp. 316-321, 1997.
- [4] J.J. Jacobs et al., "Current concepts review - corrosion of metal orthopaedic implants," *J. Bone Joint Surg. Am.*, vol. 80A, no. 2, pp. 268-282, 1998.
- [5] M. Sivakumar et al., "Failures in stainless steel orthopaedic implant devices: A survey," *J. Mater. Sci. Lett.*, vol. 14, no. 5, pp. 351-354, 1995.
- [6] M. Sivakumar et al., "Investigation of failures in stainless steel orthopaedic implant devices: Fatigue failure due to improper fixation of a compression bone plate," *J. Mater. Sci. Lett.*, Vols. 142-145, no. 2, pp. 13, 1994.
- [7] Canadian Institute for Health Information, "Canadian joint replacement registry (CJRR) 2008–2009 annual report," CIHI, Ottawa, 2009.
- [8] H.-P. Sieber et al., "Analysis of 118 second-generation metal-on-metal retrieved hip implants," *J. Bone Joint Surg.*, vol. 81, no. 1, pp. 46-50, 1999.
- [9] London Implant Retrieval Centre, "Report on a Retrieved Metal-on-Metal Hip

Arthroplasty," LIRC Co., Huddersfield.

- [10] P. Roberts et al., "Hip resurfacing arthroplasty of the hip," *Curr. Orthop.*, vol. 19, no. 4, pp. 263-279, 2005.
- [11] P.F. Doorn et al., "Tissue reaction to metal on metal total hip prostheses," *Clin. Orthop. Relat. Res.*, no. 329 Suppl., pp. S187-S205, 1996.
- [12] J. Fisher et al., "Wear of surface engineered metal-on-metal hip prosthese," *J. Mater. Sci. Mater. Med.*, vol. 15, no. 3, pp. 225-235, 2004.
- [13] S. Williams et al., "In vitro analysis of the wear, wear debris and biological activity of surface-engineered coatings for use in metal-on-metal total hip replacements," *Proc. Inst. Mech. Eng. H*, vol. 217, no. 3, pp. 155-163, 2003.
- [14] J.J. Jacobs et al., "Cobalt and chromium concentrations in patients with metal on metal total hip replacements," *Clin. Orthop. Relat. Res.*, no. 329 Suppl., pp. 329 Suppl., 1996.
- [15] E. Frigerio et al., "Metal sensitivity in patients with orthopaedic implants: a prospective study," *Contact Dermatitis*, vol. 64, no. 5, pp. 273-279, 2011.
- [16] H. Koseki et al., "Surface engineered metal-on-metal bearings improve the friction and wear properties of local area contact in total joint arthroplasty," *Surf. Coat. Technol.*, vol. 202, no. 19, pp. 4775-4779, 2008.
- [17] A. Seibert, "Hip pain: causes and treatment," WebMD LLC., 13 August 2012. [Online]. Available: <http://www.webmd.com/pain-management/guide/hip-pain-causes-and-treatment>.
- [18] W. J. Hamilton, *Textbook of human anatomy*, Macmillan, 2010.

- [19] Canadian Institute for Health Information, "Hospitalizations, early revisions and infections following joint replacement surgery," CIHI, Ottawa, 2008.
- [20] R.V. Mierlo, "Hip resurfacing versus total hip replacement," 05 June 2006.
[Online]. Available: <http://resurfacingscan.be/ebhrvthr.htm>.
- [21] Patient educator, "Total hip replacement," Stryker Corp., [Online]. Available: <http://www.kayalortho.com/patient-education/stryker-library/your-hip/total-hip-joint-replacement/>.
- [22] Birmingham, "Birmingham Hip Modular Head (used in hip replacements)," Therapeutic Goods Administration, 30 October 2012. [Online]. Available: <http://www.tga.gov.au/safety/alerts-device-hip-bhmmh-121030.htm>.
- [23] J. Charnley, "Fracture of femoral prostheses in total hip replacement: A clinical study," *Clin. Orthop. Relat. Res.*, vol. 111, pp. 105-120, 1975.
- [24] B.M. Wroblewski et al., "The Charnley hip replacement-43 years of clinical success," *Acta. Chir. Ortho. Traumatol Cech.*, vol. 73, no. 1, pp. 6-9, 2006.
- [25] D. Downson, "New joints for millennium: Wear control in total replacement hip joints," *Proc. Inst. Mech. Eng. H*, vol. 215, no. 4, pp. 335-358, 2001.
- [26] D.W. Manning et al., "In vivo comparative wear study of traditional and highly cross-linked polyethylene in total hip arthroplasty," *J. Arthroplasty*, vol. 20, no. 7, pp. 880-886, 2005.
- [27] E. Oral et al., "Wear resistance and mechanical properties of highly cross-linked, ultrahigh-molecular weight polyethylene doped with vitamin E," *J. Arthroplasty*, vol. 21, no. 4, pp. 580-591, 2006.

- [28] U. Holzwarth and G. Cotogno, "Total hip arthroplasty: State of the art, challenges and prospects," Joint Res. Centre of the Eur. Commission, Ispra, 2012.
- [29] D. Dowson et al., "A hip joint simulator study of the performance of metal-on-metal joints: Part II: design," *J. Arthroplasty*, vol. 19, no. 8 Suppl. 3, pp. 124-130, 2004.
- [30] L. Savarino et al., "Ion release in stable hip arthroplasties using metal-on-metal articulating surfaces: A comparison between short-and-medium-term results," *J. Biomed. Mater. Res. A.*, vol. 66, no. 3, pp. 450-456, 2003.
- [31] D. McMinn and J. Daniel, "History and modern concepts in surface replacement," *Proc. Inst. Mech. Eng. H*, vol. 220, no. 2, pp. 239-251, 2006.
- [32] M.A. Mont et al., "Hip resurfacing arthroplasty," *J. Am. Acad. Orthop. Surg.*, vol. 14, no. 8, pp. 456-463, 2006.
- [33] Smith & Nephew, "Birmingham hip resurfacing system," 2006. [Online]. Available:
http://images.businessweek.com/ss/06/08/medical_products/source/5.htm.
- [34] F.W. Chan et al., "Numerical analysis of time-varying fluid film thickness in metal-metal hip implants in simulator tests," *ASTM Spec. Tech. Publ.*, vol. 1346, pp. 111-128, 1999.
- [35] Z.M. Jin and D. Dowson, "A full numerical analysis of hydro-dynamic lubrication in artificial hip joint replacements constructed from hard materials," *Proc. Inst. Mech. Eng. C*, vol. 213, pp. 355-370, 1999.
- [36] B.J. Hamrock et al., "Introduction," in *Fundamentals of Fluid Film Lubrication*,

2nd ed., New York, Marcel Dekker Inc., 2004, pp. 1-22.

- [37] R. Bosman and D.J. Schipper, "Microscopic mild wear in the boundary lubrication regime," Univ. Twente, Enschede.
- [38] S.L. Smith et al., "The effect of femoral head diameter upon lubrication and wear of metal-on-metal total hip replacements," *Proc. Inst. Mech. Eng. H*, vol. 215, no. 2, pp. 161-170, 2001.
- [39] I.M. Hutchings, *Friction, Lubrication and Wear of Artificial Joints*, London: Professional Engineering Publishing, 2003.
- [40] Z.M. Jin et al., "Biotribology," *Curr. Orthop.*, vol. 20, no. 1, pp. 32-40, 2006.
- [41] J. Nevelos et al., "Metallurgical considerations in the wear of metal-on-metal hip bearings," *Hip Int.*, vol. 14, no. 1, pp. 1-10, 2004.
- [42] Y. Yan et al., "Tribocorrosion in implants-assessing high carbon and low carbon Co-Cr-Mo alloys by in situ electrochemical measurements," *Tribol. Int.*, vol. 39, no. 12, pp. 1509-1517, 2006.
- [43] H.S. Dobbs and M.J. Minski, "Metal ion release after total hip replacement," *Biomaterials*, vol. 1, no. 4, pp. 193-198, 1980.
- [44] J.H. Dumbleton and M.T. Manley, "Metal-on-metal total hip replacement: What does literature say?," *J. Arthroplasty*, vol. 20, no. 2, pp. 174-188, 2005.
- [45] Y. Liao et al., "CoCrMo metal-on-metal hip replacements," *Phys. Chem. Chem. Phys.*, vol. 15, no. 3, pp. 745-756, 2013.
- [46] R.M. Urban et al., "Dissemination of wear particles to the liver, spleen, and abdominal lymph nodes of patients with hip or knee replacement," *J. Bone Joint*

- Surg Am.*, vol. 82, no. 4, pp. 457-476, 2000.
- [47] D.J. Lantong et al., "Adverse reaction to metal debris following hip resurfacing: the influence of component type, orientation and volumetric wear," *J. Bone Joint Surg. Br.*, vol. 93, no. 2, pp. 164-171, 2011.
- [48] H. Hermawan et al., *Biomedical Engineering - From theory to applications: Metals for biomedical applications*, InTech, 2011.
- [49] J. B. Park, *Biomaterials Science and Engineering*, New York: Plenum Press, 1984.
- [50] J.B. Park, *Biomaterials: An introduction*, New York: Plenum Press, 1992.
- [51] Y. Okazaki and E. Gotoh, "Implant applications of highly corrosion-resistant Ti-15Zr-4Nb-4Ta alloy," *Mater. Trans.*, vol. 43, no. 12, pp. 2943-2948, 2002.
- [52] K. Harris and S. Steve, "Investment cast cobalt alloys," Cannon Muskegon Corp., [Online]. Available: http://www.c-mgroup.com/abstracts/investment_cast_cobalt_alloys.htm.
- [53] G. Manivasagam et al., "Biomedical implants: Corrosion and its prevention - A review," *Recent Patents on Corros. Sci.*, vol. 2, pp. 40-54, 2010.
- [54] E.N. Codaro et al., "Corrosion behavior of a cobalt-chromium-molybdenum alloy," *Russ. J. Electrochem.*, vol. 36, no. 10, pp. 1117-1121, 2000.
- [55] Y. Yan et al., "Tribo-corrosion properties of cobalt-based medical implant alloys in simulated biological environments," *Wear*, vol. 263, no. 7-12, pp. 1105-1111, 2007.
- [56] NACE Resource Center, "Metals for implantation," NACE Int., [Online]. Available: <http://events.nace.org/library/corrosion/Implants/Metals.asp>.

- [57] J.R. Davis et al., "Cobalt-Base Alloys," in *Nickel, Cobalt, and Their Alloys*, 2nd ed., Materials Park, ASM International, 2000, pp. 362-370.
- [58] A. Salinas-Rodriguez, "The role of the FCC-HCP phase transformation during the plastic deformation of Co-Cr-Mo-C alloys for biomedical applications," *ASTM Spec. Tech. Publ.*, vol. 1365, pp. 108-121, 1999.
- [59] R. Büscher and A. Fischer, "The pathways of dynamic recrystallization in all-metal hip joints," *Wear*, vol. 259, no. 7-12, pp. 887-897, 2005.
- [60] I. Radu et al., "Tribological behaviour of Stellite 21 modified with Yttrium," *Wear*, vol. 257, no. 11, pp. 1154–1166, 2004.
- [61] WPI, "The WPI international corporate leaders roundtable: The impact of evolving technologies on the future of business: Notable achievements of alumni of Worcester Polytechnic Institute," Worcester Polytechnic Institute, Worcester, 2001.
- [62] J.J. Jacobs et al., "Can metal levels be used to monitor metal-on-metal hip arthroplasties?," *J. Arthroplasty*, vol. 19, no. 8 Suppl. 3, pp. 59-65, 2004.
- [63] D. Dowson et al., "A hip joint simulator study of the performance Part I: The role of materials," *J. Arthroplasty*, vol. 19, no. 8 SUPPL., pp. 118-123, 2004.
- [64] D. Dowson, "Tribological principles in metal-on-metal hip joint design," *Proc. Inst. Mech. Eng. H*, vol. 220, no. 2, pp. 161-171, 2006.
- [65] M.A.L. Hernández-Rodríguez et al., "Wear of cast metal–metal pairs for total replacement hip prostheses," *Wear*, vol. 259, no. 7-12, pp. 958-963, 2005.
- [66] A. Kinbrum and A. Unsworth, "The wear of high-carbon metal-on-metal bearings

- after different heat treatments.," *Proc. Inst. Mech. Eng. H*, vol. 222, no. 6, pp. 887-895, 2008.
- [67] H. Yu et al., "Tribo-mechanical evaluations of cobalt-based (Stellite 4) alloys manufactured via HIPing and casting," in *Proceedings of the World Congress on Engineering*, London, 2007.
- [68] P. Huang et al., "Tribological behaviour of cast and wrought Co–Cr–Mo implant alloys," *Mater. Sci. Technol.*, vol. 15, no. 11, pp. 1324-1330, 1999.
- [69] I. Catelas et al., "Wear particles from metal-on-metal total hip replacements: Effects of implant design and implantation time," *Proc. Inst. Mech. Eng. H*, vol. 220, pp. 195-207, 2006.
- [70] M.E. Wait et al., "Tissue reaction of CoCr wear debris from metal on metal total hip replacements," *Trans. Eur. Orthop. Res. Soc.*, 1995.
- [71] E.W. Soh et al., "Size and shape of metal particles from metal-on-metal total hip replacements," *Trans. Orthop. Res. Soc.*, 1996.
- [72] P.F. Doorn et al., "Metal wear particle characterization from metal on metal total hip replacements: Transmission electron microscopy study of periprosthetic tissues and isolated particles," *J. Biomed. Mater. Res.*, vol. 42, pp. 103-111, 1998.
- [73] Z.M. Jin et al., "Artificial hip joints," in *Encyclopedia of Medical Devices and Instrumentation*, 2nd ed., J.G. Webster, Ed., New York, John Wiley & Sons, 2006.
- [74] M. Silva et al., "Metal-on-metal total hip replacement," *Clin. Orthop. Relat. Res.*, vol. 430, pp. 53-61, 2005.
- [75] M.A. Germain et al., "Comparison of the cytotoxicity of clinically relevant cobalt-

- chromium and alumina ceramic wear particles in vitro," *Biomaterials*, vol. 24, no. 3, pp. 469-479, 2003.
- [76] A. Kocljan et al., "Cobalt-based alloys for orthopaedic applications studied by electrochemical and XPS analysis," *J. Mater. Sci. Mater. Med.*, vol. 15, no. 6, pp. 643-650, 2004.
- [77] J. Chen et al., "Improving the wear properties of Stellite 21 alloy by plasma surface alloying with carbon and nitrogen," *Wear*, vol. 264, no. 3-4, pp. 157-165, 2008.
- [78] J. Fisher et al., "An in vitro study of the reduction in wear of metal-on-metal hip prostheses using surface-engineered femoral heads," *Proc. Inst. Mech. Eng. H.*, vol. 216, no. 4, pp. 219-230, 2002.
- [79] J. Lutz and S. Mändl, "Wear mechanism, wear rate and contact pressure in PIII nitrided CoCr alloys," *Plasma Process and Polymers*, vol. 6, no. Suppl. 1, pp. S65-S69, 2009.
- [80] R. Wei et al., "High-intensity plasma ion nitriding of orthopedic materials: Part I. Tribological study," *Surf. Coat. Technol.*, vol. 186, no. 1-2, pp. 305-313, 2004.
- [81] B.R. Lanning et al., "High intensity plasma ion nitriding of orthopedic materials Part II. Microstructural analysis," *Surf. Coat. Technol.*, vol. 186, no. 1-2, pp. 314-319, 2004.
- [82] J.F. Archard, "Contact and rubbing of flat surfaces," *J. Appl. Phys.*, vol. 24, no. 8, pp. 981-988, 1953.
- [83] U. Kamachimudali et al., "Corrosion of bio implants," *Sadhana*, vol. 28, no. 3-4,

pp. 601–637, 2003.

- [84] J.R. Davis, *Corrosion: Understanding the basics*, ASM International, 2000.
- [85] R.E. Andrews et al., "Effects of cobalt and chromium ions at clinically equivalent concentrations after metal-on-metal hip replacement on human osteoblasts and osteoclasts: Implications for skeletal health," *Bone*, vol. 49, no. 4, pp. 717-723, 2011.
- [86] C. Fleury et al., "Effect of cobalt and chromium ions on human MG-63 osteoblasts in vitro: Morphology, cytotoxicity, and oxidative stress," *Biomaterials*, vol. 27, no. 18, pp. 3351 – 3360, 2006.
- [87] Gamry, "Basics of electrochemical impedance spectroscopy," Gamry Instruments Inc., Warminster, 2010.
- [88] J.R. Macdonald, "Impedance spectroscopy," *Ann. Biomed. Eng.*, vol. 20, no. 3, pp. 289-305, 1992.
- [89] V.F. Lvovich, "Examples of ideal equivalent circuit models," in *Impedance Spectroscopy: Applications to Electrochemical and Dielectric Phenomena*, 1st ed., Hoboken, John Wiley & Sons, Inc., 2012, pp. 49-57.
- [90] R.W. Revie and H.H. Uhlig, "Polarization and corrosion rates," in *Corrosion and Corrosion Control*, 4th ed., Hoboken, John Wiley & Sons Inc., 2008, pp. 53-82.
- [91] A. Mohammad, "Studies of the use of electrochemical impedance spectroscopy to characterize and assess the performance of lacquers used to protect aluminum sheet and can ends," M.A.Sc Thesis, Dept. of Mech. and Aero. Eng., Carleton University, Ottawa, 2013.

- [92] A. Stefánsson et al., "New methods for the direct determination of dissolved inorganic, organic and total carbon in natural waters by Reagent-Free Ion Chromatography and inductively coupled plasma atomic emission spectrometry," *Anal. Chim. Acta.*, vol. 582, no. 1, pp. 69-74, 2007.
- [93] ASTM G99 - 05 (2010), "Standard test method for wear testing with a Pin-on-Disk apparatus," Amer. Soc. Test. Mater., West Conshohocken, 2000.
- [94] ASTM G5 - 13, "Standard reference test method for making potentiostatic and potentiodynamic anodic polarization measurements," Amer. Soc. Test. and Mater., West Conshohocken, 2011.
- [95] L. Tan et al., "Preparation and characterization of Ca-P coating on AZ31 magnesium alloy," *Trans. Nonferrous Met. Soc. China*, vol. 20, no. 2, pp. 648-654, 2010.
- [96] J.N. Murray, "Electrochemical test methods for evaluating organic coatings on metals: An update. Part I. Introduction and generalities regarding electrochemical testing of organic coatings.," *Prog. Org. Coat.*, vol. 30, no. 4, pp. 225-233, 1997.
- [97] F. Mansfeld, "Use of electrochemical impedance spectroscopy for the study of corrosion protection by polymer coatings," *J. Appl. Electrochem.*, vol. 25, no. 3, pp. 187-202, 1995.
- [98] J.A. Ortega-Saenz et al., "Tribological and corrosion testing of surface engineered surgical grade CoCrMo alloy," *Wear*, vol. 271, no. 9-10, pp. 2125–2131, 2011.
- [99] L.M. Calle and L.G. MacDowell, "Electrochemical evaluation of stainless steels in acidified sodium chloride solutions," NASA, FL, 2004.

- [100] B. Beverskog and I. Puigdomenech, "Revised pourbaix diagrams for chromium at 25-300°C," *Corros. Sci.*, vol. 39, no. 1, pp. 43-57, 1997.
- [101] ASTM G102 - 89 (1999), "Standard practice for calculation of corrosion rates and related information from electrochemical measurements," Amer. Soc. Test. Mater., West Conshohocken, 1999.
- [102] Deloro Stellite, "Stellite 21 alloy," Deloro Stellite Inc., Swindon, 2007.
- [103] Deloro Stellite, "Stellite 12 Alloy," Deloro Stellite Inc., Swindon, 2007.
- [104] C.H. Hsu and F. Mansfeld, "Technical Note: Concerning the conversion of the constant phase element parameter Y_0 into a capacitance," *Corrosion*, vol. 57, no. 09, pp. 747-748, 2001.
- [105] M.G.S. Ferreira et al., "Semiconducting properties of oxide and passive films formed on AISI 304 stainless steel and alloy 600," *J. Braz. Chem. Soc.*, vol. 13, no. 4, pp. 433-440, 2002.
- [106] "Inductively coupled plasma atomic emission spectroscopy," 27 May 2013.
[Online]. Available:
http://en.wikipedia.org/wiki/Inductively_coupled_plasma_atomic_emission_spectroscopy.
- [107] Admin, "Inductively coupled pasma (ICP)," Glassware Chem., 4 June 2012.
[Online]. Available: <http://glasswarechemical.com/tag/icp-oes-%E0%B8%84%E0%B8%B7%E0%B8%AD/>.
- [108] B. Beard, "Analytical methods for non-traditional isotopes," *Rev. Mineral. Geochem.*, vol. 55, pp. 113-152, 2004.

- [109] R.A. Poggie, "A review of the effect of design, contact stress, and materials on the wear of metal-on-metal hip prostheses," *ASTM Spec. Tech. Publ.*, vol. 1346, pp. 47-54, 1999.
- [110] G.N. Norman and E. Alan, *Chemistry of the Elements*, Oxford: Pergamon Press, 1984.
- [111] R. Ahmed et al., "Influence of re-HIPing on the structure–property relationships of cobalt-based alloys," *Tribol. Int.*, vol. 57, pp. 8-21, 2013.
- [112] R. Warren, *Ceramic–matrix composites*, New York: Chapman & Hall, 1992.
- [113] G. Bertrand et al., "A study of the corrosion behaviour and protective quality of sputtered chromium nitride coatings," *Surf. Coat. Technol.*, Vols. 199-209, no. 2-3, pp. 126, 2000.
- [114] T. Christiansen and M.A.J. Somers, "Controlled dissolution of colossal quantities of nitrogen in stainless steel," *Metall. Mater. Trans. A*, vol. 37, no. 3, pp. 675-682, 2006.
- [115] D. Raghu and J.B. Wu, "Recent development in wear and corrosion-resistant," *Mater. Perform.*, vol. 36, no. 11, pp. 27-36, 1997.